VIENNA UNIVERSITY OF TECHNOLOGY
DEPARTMENT OF GEODESY AND GEOINFORMATION
RESEARCH GROUPS PHOTOGRAMMETRY & REMOTE SENSING

DIPLOMARBEIT

Calibration of space-borne Scatterometers: Towards a consistent climate data record for Soil Moisture Retrieval

Ausgeführt zum Zwecke der Erlangung des akademischen Grades
eines Diplom-Ingenieur unter der Leitung von

Univ.Prof. Dipl.-Ing. Dr.techn. Wolfgang Wagner
Department für Geodäsie und Geoinformation
Forschungsgruppen Photogrammetrie und Fernerkundung

eingereicht an der
Technischen Universität Wien
Fakultät für Mathematik und Geoinformation
von

Christoph Reimer
Matrikelnummer 0525149
Simon-Denk-Gasse 2/6
A-1090 Wien

Wien, am 10. Juni 2014 ....

Abstract

Higher level scatterometer products, such as surface soil moisture and wind vector fields became an important input dataset for climate change research. For this reason an accurate radiometric calibration of space-borne scatterometers is needed by the scientific community to establish a long-term consistent climate data record. Accordingly a novel radiometric calibration methodology is developed with the objective to achieve a consistent calibration of the European scatterometer mission onboard of the European Remote-Sensing Satellite (ERS) and the Meteorological Operational Platform (MetOp). The introduced calibration method is a stepwise relative calibration approach by making use of applicable extended area land-targets. A set of appropriate extended area calibration targets is determined by a threshold based decision scheme using three parameters to characterise backscatter attributes of individual land-targets. Consistent calibrated backscatter coefficients throughout a specific scatterometer mission are achieved by conducting sensor intra-calibration. Radiometric calibration deficiencies are explored in individual antenna beams of ERS-2 AMI-WS and MetOp-A ASCAT revealing deviations to a defined calibration reference in the order of 0.2 dB for AMI-WS and 0.1 dB for ASCAT respectively. Similarities in the instrument technical design of AMI-WS and ASCAT encourage a merging of these European scatterometer missions. As a consequence, a second calibration methodology is introduced on top of sensor intra-calibration, with the objective to identify possible differences in the radiometric calibration levels of the two scatterometer missions, referred to as sensor inter-calibration. Differences in the calibration levels of AMI-WS and ASCAT are found to reveal biases ranging from 0.39 dB to -0.08 dB. The capability of the developed stepwise calibration methodology to correct for such calibration related deficiencies is demonstrated by the use of independent verification targets. Taking advantage of the developed stepwise calibration methodology will result in a long-term consistent calibrated European scatterometer data archive comprising more than 30 years of global data.

Acknowledgements

The present research was undertaken at the Research Group Remote Sensing within the Department of Geodesy and Geoinformation at Vienna University of Technology (TU-Wien). I am extremely grateful for the opportunity and trustfulness to be part of a highly professional and motivated research group over the last years.

I would like to thank ...

... my supervisor Prof. Wolfgang Wagner for regular discussions and inspirations to accomplish the present study. From the first discussion to the finalisation of this work it has been a long journey, but Prof. Wagner never exerted pressure on myself and displayed patience, which was vital for the achievement of the present research.

... all my colleagues within the Research Groups Remote Sensing and Photogrammetry for providing such a great working atmosphere and environment to perform this Master Thesis.

... Richard Kidd for reinforcing my self-confidence into this work and having motivating words during the long and stony process of writing this Master Thesis.

... my colleagues of the WARP developer team, Sebastian Hahn, Thomas Melzer, Chistoph Paulik and Stefan Hasenauer, for fruitful discussions about surface soil moisture retrieval from spaceborne scatterometers and the development of a great framework for processing the investigated data archives.

... my family for their continuing appreciation and support of my educational career.

... my partner Cornelia for her patience and support all the time, from the beginning to the end of this Master Thesis.

Contents

List of Figures

List of Tables

List of Symbols

A_{rs}, A_r	effective area of surface target or receiver antenna.
$G(\theta,\phi), G_t, G_{ts}, G_r$	antenna gain pattern, generic, of the transmitter antenna, surface target and receiver antenna.
P_t, P_{rs}, P_{ts}, P_r	EM power transmitted, intercepting the surface target, scattered from the target and entering the receiver antenna.
R_t, R_r	distance to the surface target (t) and from the target to the receiver antenna (r).
S_t, S_r	power density in surface target and receiver antenna direction.
ν	temporal variability parameter of surface target.
$\overline{\sigma^0}$	estimate of the backscatter coefficient of a surface target.
σ, σ^0	radar cross section and normalised radar cross section.
f_a	fraction of absorbed electromagnetic radiation.

Chapter 1

Introduction

Earth Observation (EO) from space has become a beneficial information provider for our society over the last decades. Rapid technological growth since the 1960s has advanced the ability of satellites to monitor geophysical processes on a global scale and improve our understanding of the system Earth. Enhancements of space-borne remote sensing instruments and innovations in computer technology ensure fast and comprehensive interpretation of recorded EO data. Nowadays, satellite records can be processed within hours after sensing and telecommunication networks allow global dissemination of the derived information. Therefore, EO becomes a technology driver and a considerable service provider for a large spectrum of applications with socio-economic benefits. The spectrum of applications ranges from weather forecasting to disaster management, from crop monitoring to risk-maps for epidemics and many more. The Group on Earth Observation (GEO) initiated a 10-year implementation plan for the *creation of a comprehensive, coordinated, and sustained Earth observations framework* [*GEO*, 2013] called the Global Earth Observation System of Systems (GEOSS). GEOSS will be a distributed system linking together already existing and planned EO systems of members of GEO. Information will be provided across the nine societal benefit areas with the aim of enhancing human health, safety and welfare, alleviating human suffering including poverty, protecting the global environment and achieving sustainable development. These societal benefit areas are disaster, health, energy, climate, water, weather, ecosystems, agriculture and biodiversity. Climate change is today's most compelling issue affecting all societal benefit areas and moreover all life-forms on Earth. The climate component of GEO is implemented by the Global Climate Observing System (GCOS), a system that has the aim of providing long-term comprehensive observations to monitor the Earth climate system [*GCOS*, 2010]. Fifty Essential Climate Variables (ECVs) were identified for atmospheric, ocean and terrestrial domains in 2010, with the focus to understand the climate system in terms of detecting and attributing climate changes. The requirement of long-term comprehensive observations is a challenging task, because of the need to merge various instrument records to a single consistent ECV. Instrument records approved for ECVs production differ in spatial scales, temporal sampling, observation period and recording technique (in-situ or remote sensing). The detection of climate change from space is a tremendous task, given that space-based instruments have to be able to measure small changes in long-term global records [*Ohring et al.*, 2005]. Current operational satellite instruments are designed to support short-term weather and environmental predictions. Sensors and onboard electronic components degrade in orbit over time and long-term satellite observation need to be merged from several satellite missions. This will cause artefacts in space-borne instrument long-term observations and degrade the overall quality of the satellite observation and accuracy of derived ECVs. Previously, insufficient attention was paid to pre- and post launch instrument characterisation and calibration which would help in overcoming these challenges of observing climate changes from space. Highly accurate measurements from space are required to address the questions of climate change:

- What is the current rate of climate change?
- What will the climate be in the future?

Future climate state on Earth is predicted by complex climate models. Various models propose different climate conditions in the future, so which model do we trust? The reliability of climate models can be validated by comparing model forecast against observations, representing the current state of the climate. Satellite observations are exclusively able to provide measurements with the required global perspective, highlighting the significance of space-borne remote sensing data for climate change research. It is the responsibility of the satellite data providers, essentially the Space Agencies, to enable access to long-term consistent satellite measurements for climate change monitoring by means of adequate instrument calibration strategies and historical EO data preservation [*Chander et al.*, 2013].

1.1 Motivation and Structure of Work

Surface soil moisture (SSM) was recognised as an Essential Climate Variable (ECV) in 2010 and accordingly become an important dataset for climate change research. Traditionally, worldwide networks, operated by universities, met services, etc. , record SSM measurements at in-situ stations in various depth. However, point scale in-situ measurements of SSM are not suited to provided the global picture of SSM variations desired for comprehensive climate change research. *Wagner et al.* [1999a] demonstrated the feasibility of SSM retrieval by the use of global data provided by C-band scatterometers flown onboard the European Remote-Sensing Satellites (ERS). The developed SSM retrieval algorithm, referred to as TU Wien model and implemented in the WAter Retrieval Package (WARP), is based on a change detection approach, utilising a set of model parameters determined by multi-annual scatterometer data analysis. Algorithmic improvements and adaptations concentrating on a more robust model parameter estimation and the migration of WARP to handle scatterometer data originating from MetOp were conducted over the last years by *Bartalis et al.* [2007] and *Naeimi et al.* [2009]. Scatterometers are categorised as real aperture RADAR systems.

They continuously sample the Earth's surface, facilitating all-day observations from space. Scatterometers are active microwave instruments transmitting controlled electromagnetic (EM) pulses towards the Earth's surface and record the energy scattered back. Backscattered energy is detected by an antenna and subsequently converted to an electrical signal. The physical quantity of interest, the normalised radar cross section (NRCS), is derived by a conversion of the electrical signal by taking advantage of scatterometer system related parameters. The determination of scatterometer system related parameters is referred to as radiometric calibration, quantifying the relationship between the raw instrument recordings and the physical quantity of interest, the normalised radar cross section σ^0. As a consequence, radiometric calibration of a scatterometer system is crucial to ensure accurate measurements of the normalised radar cross section σ^0 of the Earth's surface. During the lifetime of a scatterometer, diverse mechanical and electrical components onboard will degrade over time, affecting the radiometric calibration and, accordingly, the accuracy of the physical quantity of interest. With respect to surface soil moisture retrieval from scatterometers, unaccounted calibration related artefacts, reflected in the normalised radar cross section, will affect the precision of the model parameters and furthermore induce accuracy losses in the SSM prediction. Hence, instrument related artefacts need to be considered in the creation of a surface soil moisture ECV for climate change research. Consequently, one objective of this work is to support already established radiometric calibration strategies of European space-borne scatterometers to ensure consistent well-calibrated observations of the NRCS of individual mission. Additionally, climate change research requires long-term global observations which may be accomplished by merging observations of different scatterometer missions over time. Similarities in the instrument technical design of scatterometers onboard of ERS and MetOp, encourage the fusion of these missions towards a long-term European scatterometer data archive. Ultimately, the second objective of this study is to develop a methodology for the detection and correction of possible biases in the recorded normalised radar cross section σ^0 of the Earth's surface between these European scatterometer missions. The correction of potential biases in the normalised radar cross section between scatterometer mission is crucial for the creation of a long-term consistent European scatterometer data archive, comprising more than 30 years of global observation, for a comprehensive SSM retrieval to support climate change research.

The present work is structured into five chapters outlining the major aspects investigated during the preparation phase of this study. **Chapter 2** give a basic overview of current state of the art space-borne microwave instruments and their different fields of applications. The chapter is complemented by an explanation of various calibration procedures, performed during the lifetime of a scatterometer before lift-off and during operations in space. The measurement principle of space-borne scatterometers is discussed in **Chapter 3**, stating the derivation of the monostatic RADAR equation, restrictions on the spatial resolution of RADAR systems in general and how scatterometers achieve radiometric accurate measurements of the normalised radar cross section. Furthermore, an overview of ERS-1/2 and MetOp-A mission parameters is provided with a description of the technical parameters of the onboard scatterometers and the on-ground processing of the data. Already established radiometric calibration methods of ERS-1/2 and MetOp-A scatterometers are outlined at the end of this chapter. The proposed calibration methodology, developed within this study, is presented in **Chapter 4**. Suitable natural calibration targets, essential for the success of the proposed relative calibration approach, are investigated, based on defined requirements reflected in a set of parameters describing scattering characteristics of the Earth's surface. The calibration methodology is divided into two calibration steps which are discussed in detail, completing the chapter. **Chapter 5** is dedicated to the practical application of the presented calibration methodology, considering backscatter observations originating from scatterometers onboard ERS-2 and MetOp-A. Results are verified with an independent subset of calibration targets to confirm the feasibility of the proposed calibration approach. The present work is concluded with a discussion about pros and cons of proposed calibration methodology given in **Chapter 6**. Additionally, scatterometer data calibrated with the presented methodology and processed with the latest version of the WAter Retrieval Package (WARP), are compared to SSM retrievals which have been deduced from the same dataset, but by neglecting the proposed calibration steps. Finally, potential new applications of the presented calibration methodology are discussed with respect to the production of long-term consistent surface soil moisture products.

Chapter 2

Microwave Remote Sensing and Calibration of Scatterometers

2.1 Overview of the Chapter

Microwave remote sensing is a rather novel technique in Earth Observation (EO), dating back to September 1968 with the launch of Cosmos 243 satellite [*Kramer*, 2002]. This chapter give a short and very general overview about microwave remote sensing and it's various kinds of instruments for data acquisition from space. Aspects of microwave remote sensing are discussed, highlighting differences to other remote sensing techniques and the distinction of passive and active microwave sensors. Furthermore, an overview of several active space-borne microwave instruments is given with respect to specific instrument characteristics and areas of applications. The chapter is completed by an introduction to calibration of space-borne scatterometers, outlining the needs of well calibrated sensors and the fundamental concepts of radiometric calibration.

2.2 Introduction

Earth Observation, or more specifically remote sensing of the Earth, is defined as the use of EM radiation to acquire information about the ocean, land and atmosphere without being in physical contact with the object, surface or phenomenon under investigation [*Martin*, 2004]. Because of atmospheric interference, EM radiation suitable for Earth remote sensing is limited to three wavelength bands called the visible, infrared and microwave. Remote sensing in the visible spectrum of EM radiation depends on reflected sunlight and is restricted to daytime and cloud free periods. Though observations of thermal radiation of the Earth's surface in the infrared are independent of sunlight, they are still restricted to cloud free periods. However, in the microwave domain of the EM spectrum (wavelengths from 1 mm to 1 m) observations neither depend on sunlight nor are restricted to cloud free periods. Long wavelength microwaves penetrate deeper into vegetation, snow and soil and reveal information about dielectric and geometric properties of the target surface or volume. The distinct dielectric properties of water are of major importance for the success of microwave remote sensing in areas such as hydrology, forestry, agriculture and glaciology.

In general, microwave remote sensing represents a valuable source of information, because of inferring additional physical parameters of a target which are concealed in the visible and infrared spectrum. This sounds rather trivial but information retrieved by microwaves will complement visible and infrared sensing methods to delineate all target properties we wish to sense remotely. In contrast to lenses or mirrors used for visible and infrared remote sensing, antennas are used for microwave observations to detect the incoming EM radiation. Antennas of several metres in size are required to achieve spatial resolutions in the order of kilometres due to the long wavelength nature of microwaves. Generally speaking we may distinguish two types of microwave remote sensing instruments: passive and active.

2.3 Space-borne Microwave Instruments

Passive microwave instruments, radiometers, measure naturally emitted microwave energy from the Earth's surface. The concept behind passive microwave remote sensing is similar to that of thermal remote sensing. Objects with a physical temperature that differ from absolute zero, emit EM radiation in a wide range of wavelengths, having a continuous spectrum with one maxima related to the physical temperature of the object. In terms of objects on the Earth's surface the maxima of the emitted EM energy is found in the infrared domain, but also microwaves are emitted at a relatively low energy level. Thus, to record a signal of emitted microwave energy from space, the sensors field of view must be large to detect enough energy. Passive microwave instruments are therefore characterised by low spatial resolutions of tens of kilometres. Passive microwave systems measure the so-called brightness temperature, which is related to physical and geometric properties of a target, depending on the context of measurement. Changes in brightness temperature over the oceans are related to changes in the physical temperature of the ocean surface and the dielectric constant due to changes in the ocean salinity. For land and sea ice, variations in the brightness temperature are mainly driven by the physical temperature of the land surface, differences in emissivity related to surface roughness and variations in the dielectric constant because of changes in water content or salinity.

Active microwave instruments, Radio Detection and Ranging (RADAR) systems, carry their own source of EM energy to illuminate the Earth's surface. Active systems transmit controlled pulses of EM energy towards the surface and record the energy scattered back from a target. The transmission of a signal to illuminate a target is what makes RADAR systems an active form of remote sensing. The term RADAR stands for Radio Detection and Ranging and as the name suggests, incorporate an additional measurement variable; the range to a target. Therefore active microwave instruments comprise two different types of information. Distance information to a target is retrieved by utilising time delay measurements of the transmitted EM pulse. And secondly, the instrument detects properties of the pulse echo such as intensity or polarisation, useful to characterise target properties. Active microwave systems can be grouped into three types of RADARs: altimeter, synthetic aperture radar and scatterometer.

Altimeters are designed to exploit the ranging capability of a RADAR to infer distance information between the Earth's surface and the satellite. The antenna system of an altimeter directs a pulse of microwave energy towards nadir direction and measure the time delay of the returned echo. Combining time delay measurements with the exact position of the instrument in space, at the time of measurement, enables the Earth's surface topography to be mapped. Altimeter observations are a significant source of information about planetary scale processes of the oceans and the cryosphere. Long-term averages of ocean surface topography, derived by altimeters, contribute to the determination of the geoid, which is a fundamental reference surface in geodetic applications. Monitoring of the topography of the Earth's ice sheets of Greenland and Antarctica, inform us about net mass changes of the ice due to variations in accumulation and ablation. Ice sheets are a major freshwater reservoir, which in terms of intensive melting, will increase the global sea level and additionally will affect ocean circulations resulting in Earth climate changes.

Antenna equipment of **synthetic aperture radars** and **scatterometers** are mounted to point sideways downward, with respect to the satellite track, so that the radar beam illuminate a larger area on ground in comparison to altimeters. These side-looking RADARs transmit a sequence of microwave pulses and record the energy scattered back from the surface as a function of time delay. This allows the discrimination of the slant-range to a target with the shortest range distance near the edge of the RADAR footprint. Hence, RADAR echoes returned progressively later are further away from the instrument. Recoding the RADAR response as function of time delay, enable these RADAR systems to subdivide the RADAR footprint into smaller resolution cells (range resolution) across the satellite track. Along the satellite track, the spatial resolution (azimuthal resolution) of side-looking RADARs is governed by the physical size of the antenna. To achieve spatial resolution in the order of optical sensors (about 10 metre) would require an antenna of several kilometres, which is clearly not a very practical proposition for space-borne microwave instruments.

Synthetic Aperture Radars (SARs) utilise strategies to overcome the limitation of azimuthal resolution governed by the physical size of the antenna. The technical necessity for SAR operations is to transmit coherent microwave pulses, meaning that each transmitted pulse has the same initial amplitude and phase. A sequence of pulse echoes recorded from consecutive positions along the flight pass can be processed in a way to synthesise a very large antenna. The key parameter for this processing strategy is the recorded phase of the pulse echo to ensure a coherently combination of records as if all originate from a collection of many antennas working in unison to form a single antenna [*Woodhouse*, 2006]. Such instruments tend to have increased power consumption, high data rates and are the largest and heaviest sensors in space. SAR instruments serve as valuable input for a broad range of applications in environmental monitoring and topographic mapping.

Scatterometers, on the other hand, are specifically designed to make highly accurate measurements of the intensity of the returned microwave pulse. Corrections for atmospheric interference and instrument noise have to be applied to gain highly accurate intensity measurements, sacrificing range and azimuth resolution compared to SAR. The original aim of scatterometers was to observe wind speed and direction over the oceans by simultaneous observations from different viewing (azimuthal) directions. But soon the potential of scatterometer observations over land was recognised, resulting in promising applications related to monitoring of cryosphere, vegetation and soil properties. Highly frequent global observations independent of the predominating weather conditions and the rather simple data processing on-ground are the main advantages of scatterometers over other active microwave instruments. Derived scatterometer products, so-called Level 2 or Level 3 products [*Bennett and James*, 2013], such as surface soil moisture (SSM) [*Wagner et al.*, 1999a] or wind vector fields (WVF) [*Stoffelen*, 1998], have become an important input dataset for operational weather forecasts and climate change research. Hence, scatterometers have to be well calibrated during their mission lifetime and across different missions to meet the challenges of capturing short-term and long-term changes from space.

2.4 Calibration of space-borne Scatterometer

Generally speaking, calibration is the quantitative characterisation of the performance of an instrument [*Woodhouse*, 2006]. To understand the performance of a scatterometer in space, one needs to review the measurement principle of it. In simplified terms, a scatterometer transmits a controlled pulse towards the Earth's surface and record the energy scattered back. The backscattered energy is detected by the scatterometer antenna and is converted to an output voltage. Ultimately we are interested in the physical properties of a target illuminated by a scatterometer and not in the raw electrical signal. The relationship between the recorded voltage and the physical property of interest has to be determined. Accordingly, the determination of this relationship and its noise-related uncertainty is referred to as **radiometric calibration** of a scatterometer. During the lifetime of a spaceborne instrument two calibration procedures are traced.

In the development stage of a satellite sensor, **pre-launch calibration** is performed in order to characterise the performance of particular subsystems or even individual components of the instrument to conform to the engineering specifications. The most critical component of any microwave system is the antenna, linking the inside and the outside of a sensor. Pre-launch calibration of the antenna to determine the antenna gain pattern is an ambitious task, due to the fact that the antenna is operating in far-field conditions in space, which is challenging to replicate prior to the launch.

After the launch of an instrument onboard a satellite, **post-launch calibration or in-flight calibration** needs to be carried out on a regular basis. The need for post-launch calibration of space-borne sensors is relevant for a number of reasons. External forces such as the extreme acceleration and vibrations by launching the satellite can influence the final performance of the instrument in space. Pre-launch activities on ground are performed under the gravitational acceleration of the Earth but once in space the instrument operates in a microgravity environment. Additionally, thermal conditions in space are different to those on Earth and strongly vary throughout each orbit depending on Sun illumination. Furthermore, mechanical or electrical parts will degrade over time and consequently the overall system performance will alter during operations. Thus a careful monitoring of the instrument performance is required to guarantee accurate measurements over the period of the mission with no opportunity of physically checking or servicing the instrument in space. In the case of scatterometers, post-launch calibration activities concentrate on the radiometric stability and accuracy of the system following two separate calibration methods.

Radiometric stability of a scatterometer is achieved by continuous monitoring of variations in the transmitter and receiver chain of the instrument directly onboard. This method is referred to as **internal calibration** using a replicate of a transmitted pulse as reference signal fed into the transmitter and receiver chain to estimate the overall system gain [*Attema*, 1991]. Variations in the system gain, captured through internal calibration, are compensated to ensure radiometric stability of the scatterometer. As already mentioned, the antenna is the most critical component of any microwave system and therefore the major source of calibration errors. The process of internal calibration bypass the scatterometer antennas and for this reason is not appropriate to monitor calibration errors emerged by the antennas. Thus, to monitor the antenna performance of an instrument, it is crucial to perform **external calibration**. Targets with a well-known signal response are used to determine the relationship of transmitted and received signal affected by the antenna. Two strategies of external calibration of space-borne scatterometers are commonly used. Using active transponders, acting as artificial point targets with a well-established radar cross section, allows the deduction of calibration information about the antenna pattern across the main lobe [*Anderson et al.*, 2012]. Since calibration information using transponders is sampled at distinct positions in the antenna pattern, a second approach for antenna pattern fine tuning was proposed based on extended area land-targets [*Lecomte and Wagner*, 1998]. Targets of this type are characterised by a stable radar cross section signature over an extensive area.

Chapter 3

Principles of space-borne Scatterometers

3.1 Overview of the Chapter

An overview of different microwave remote sensing instruments was given in the previous chapter. The focus in this chapter is on the measurement principle of scatterometers and the production of the physical quantity of interest, the normalised radar cross section (NRCS). With respect to this, the RADAR equation is presented, describing the fundamental relationship between RADAR system parameters, the transmitted and recorded signal and the unknown target properties expressed by the NRCS. Besides this theoretical point of view of the measurement principle, attention will be paid to the spatial resolution of scatterometers and limitations restricting the resolution of real aperture RADAR systems. Furthermore, an important technical parameter of scatterometers is discussed, referred to as pulse repetition frequency (PRF), which is crucial to achieve the unique radiometric accuracy of such RADAR instruments. To complement these aspects of the measurement principle of scatterometers, a brief summery of the main mission events, technical parameters and the ground processing concept of the Active Microwave Instrument (AMI)-Wind Scatterometer (WS) onboard the European Remote-Sensing Satellite (ERS) and the Advanced Scatterometer (ASCAT) onboard the Meteorological Operational Platform (MetOp) is provided. Finally, already established external calibration approaches, specifying sensor related parameters and monitoring the instrument performance of AMI-WS and ASCAT are outlined.

3.2 Introduction

The objective of a scatterometer is to quantitatively characterise backscatter properties of the Earth's surface on a global scale. The focus is on the radiometric accuracy of the observations and a large-scale spatial coverage, rather than on the spatial resolution of the sensor system. To

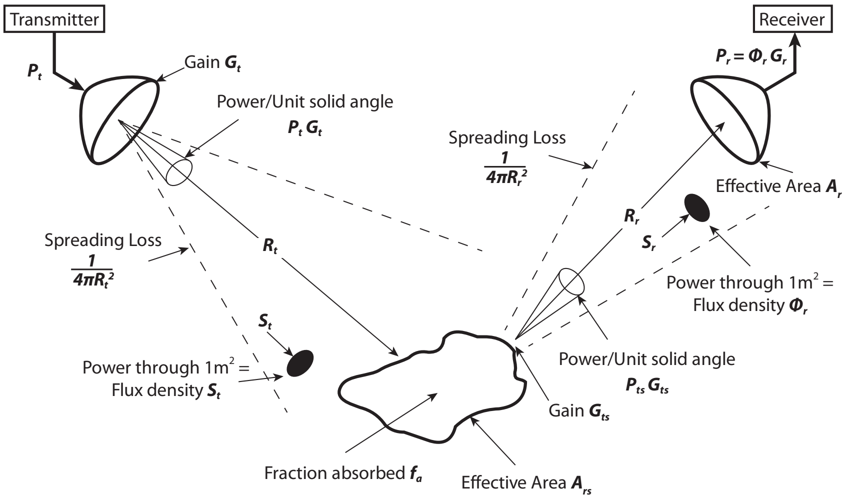

Figure 3.1: Geometry and quantities involved in the radar equation after *Ulaby et al.* [1982]

provide accurate intensity measurements from a certain surface region, a large number of independent samples are observed and averaged. Scatterometers do not provide high-resolution "images" of the Earth surface, in contrast to SAR systems, accordingly they are referred to as non-imaging RADARs or **real-aperture RADARs**. More explicitly, antennas mounted on scatterometer systems are usually directed obliquely from the instrument, pointing towards some location far from nadir. This side-looking geometry is broadly used in microwave remote sensing to achieve the desired spatial coverage of the instrument. Furthermore we may distinguish between pencil-beam and fan-beam scatterometers, since both systems are flown on various missions. The major distinction of those two systems is the physical shape of the antenna used and the principle of gathering the σ^0 backscatter coefficient of the surface. Using a side-looking parabolic antenna dish will result in a narrow spot-like surface footprint, called **pencil-beam**, impinging the surface at a constant incidence angle [*Spencer et al.*, 2000]. Due to the narrow surface footprint, pencil-beam systems are conically scanning, by an mechanically revolving antenna about the nadir axis to provide σ^0 measurements at multiple azimuth directions and constant incidence angle. On the other hand, **fan-beam** systems are designed to employ a rectangular antenna, providing a long but narrow surface footprint at a single azimuth direction. The incidence angles of the radar beam will increase from the inner to the outer edge of the radar swath. Depending on the application, the antenna beam may point to any arbitrary azimuth direction or a combination of different azimuth angles by mounting multiple antennas. The antenna configuration mounted on a fan-beam scatterometer is typically fixed with respect to the satellite and directed to any arbitrary direction sideways to the flight path, resulting in a wide swath coverage controlled by the movement of the platform.

3.3 The Radar Equation

The fundamental relationship between the characteristics of a RADAR system, the properties of a target and the received signal are explained by the RADAR equation. Figure 3.1 illustrates the basic geometry of an active microwave system along with the parameters involved in the radar equation. Hereinafter, the outlined derivation of the monostatic RADAR equation and the normalised radar cross section closely follows *Ulaby et al.* [1982]. The distance from the transmitter antenna to the target is denoted by $R_t = |\mathbf{R_t}|$ and from the surface target to the receiver antenna by $R_r = |\mathbf{R_r}|$. The power leaving the transmitter, P_t, is controlled by the antenna gain pattern $G(\theta,\phi)$. Hence the effective power emitted by the transmitter antenna is $P_t G_t$, where G_t is the value of the antenna gain $G(\theta,\phi)$ in surface target direction. The power per unit area, so called power density S_t, at the surface will result in

$$S_t = P_t G_t \frac{1}{4\pi R_t^2} , \tag{3.1}$$

where the fractional factor accounts for the decrease in power density associated with spreading of the power over a sphere of radius R_t surrounding the transmitter antenna. Finally the total power intercepted by the target is derived as the product of the power density S_t and the effective area of the target A_{rs}. It should be mentioned, that the effective area of a target is a function of it's orientation relative to the incoming radiation and depends on the effectiveness of the target scatterer as a receiving antenna.

$$P_{rs} = S_t A_{rs} \tag{3.2}$$

Natural targets on the Earth's surface are neither a perfect conductor nor a perfect isolator, thus a part of the incident power is absorbed and a fractional part is re-radiated in various directions. The fraction absorbed by the surface target is f_a, consequently the part re-radiated is $1 - f_a$, resulting in the total re-radiated power

$$P_{ts} = P_{rs}(1 - f_a) . \tag{3.3}$$

The re-radiated power P_{ts} is affected by directional sensitivity of the surface scatterer, so a gain G_{ts} in the direction of the receiver antenna is introduced. Thus, the power density S_r in the direction to the receiver system is defined as:

$$S_r = P_{ts} G_{ts} \frac{1}{4\pi R_r^2} , \tag{3.4}$$

taking into account the spreading loss towards the receiver antenna. To obtain the power entering the receiver antenna P_r, the power density S_r must be multiplied by the effective area A_r of the aperture, which is related to antenna gain G_r.

$$P_r = S_r A_r \quad with \quad A_r = \frac{\lambda^2 G_r}{4\pi} \tag{3.5}$$

By substitution of equations 3.1 to 3.4 into equation 3.5, the most general form of the so-called **bistatic RADAR equation** is found, relating the received power to the transmitted power, the scattering properties of the target and the system geometry.

$$P_r = (P_t G_t)\left(\frac{1}{4\pi R_t^2}\right)\left[A_{rs}(1-f_a)G_{ts}\right]\left(\frac{1}{4\pi R_r^2}\right)\left(\frac{\lambda^2 G_r}{4\pi}\right) \tag{3.6}$$

In the case of active microwave remote sensing systems, transmitting and receiving locations are the same, resulting in the **monostatic RADAR equation**. In the monostatic configuration a single antenna is used for the transmission and detection of the microwave signal, so that the parameters distance ($R_t = R_r = R$), antenna gain ($G_t = G_r = G$) and the effective antenna ($A_t = A_r = A$) can be generalised.

$$P_r = \frac{P_t G^2 \lambda^2}{(4\pi)^3 R^4}\left[A_{rs}(1-f_a)G_{ts}\right] \tag{3.7}$$

Quantities related to the surface target are grouped in the square brackets and are usually combined into a single parameter called the **radar cross section (RCS)** denoted by σ. The effective area A_{rs}, the absorption characteristic f_a and the radiation gain G_{ts} of a surface target is in general very challenging to determine. The amount of power scattered back and accordingly the magnitude of σ, are a complex combination of multiple parameters of an object such as shape, dielectric properties, orientation, roughness, etc. and is commonly expressed in the unit of area (m^2).

$$\sigma = A_{rs}(1-f_a)G_{ts} \tag{3.8}$$

In general, the radar cross section represents a measure of the directional reflectivity of a target as response to an incident electromagnetic wave. Accordingly, it can also be seen as the ratio between the power backscattered from a target and the power incident on a target:

$$\sigma = \frac{P_{backscattered}}{P_{incident}}\,. \tag{3.9}$$

In microwave remote sensing, sensors observe an extended area of targets rather than an individual object. The energy scattered back to the sensor refer to the proportion of energy scattered by distributed targets of an extended area, corresponding to the instrument footprint. The scattering model, used to determine the radar cross section σ (see Eq. 3.7), of a distributed area is based on the assumption that the area observed consists of many random distributed point scatterers, with no single scatterer dominating. The concept of randomly distributed targets enable the introduction of the so-called **normalised radar cross section (NRCS)**:

$$\sigma^0 = \frac{\mathrm{d}\sigma}{\mathrm{d}A}\,, \tag{3.10}$$

defined as the differential scattering cross section $\mathrm{d}\sigma$ per differential unit area $\mathrm{d}A$. In the context of microwave remote sensing, this quantity is widely used and may be referred to as backscatter coefficient or sigma-nought. The normalised backscatter coefficient is no longer a property of the measurement geometry of a sensor, enabling the comparison of measurements from different instruments. The monostatic RADAR equation of a distributed target can be derived from equation 3.7 by applying the NRCS with the assumption that dA is a function of R.

$$P_r = \frac{P_t G^2 \lambda^2}{(4\pi)^3} \int_{area\ A} \frac{\sigma^0}{R^4}\, \mathrm{d}A\,. \tag{3.11}$$

This representation of the RADAR equation is commonly used in microwave remote sensing to quantify distributed targets within the sensor footprint. The basic measurement principle of an active microwave instrument is to transmit a microwave pulse of known power P_t and record the backscattered power P_r. Therefore, a general equation (see Eq. 3.12) can be given to estimate σ^0 by means of the recorded power P_r:

$$\sigma^0 = \frac{P_r}{P_t} \frac{(4\pi)^3\, R^4}{AG^2\lambda^2}\,. \tag{3.12}$$

The unit of the normalised radar cross section, σ^0, is $m^2 m^{-2}$ and therefore a unit-less measure. However, in microwave remote sensing it is convenient to express σ^0 in logarithmic units using the pseudo-unit decibel [dB]. Values of σ^0 vary over a wide dynamic range in the linear scale, but in logarithmic scale the range is reduced to easily display the values. But even more important is the fact that the confidence interval of the measured backscatter coefficient σ^0 is independent of the magnitude in logarithmic scale, which is not the case by using the linear scale [*Ulaby et al.*, 1986].

$$\sigma^0\,[dB] = 10\,\log_{10}\sigma^0\,\left[\frac{m^2}{m^2}\right] \tag{3.13}$$

3.4 Spatial Resolution

Before continuing with the discussion about the spatial resolution of a scatterometer, it is first important to pay attention to the surface footprint of a fan-beam system. Any antenna is characterised by its power or radiation pattern, defining the energy emission of an antenna in a non-uniform fashion. The directionality of an antenna is identified by the antenna gain function $G(\theta,\phi)$, which relates the antenna input power P_t to the power density in a specific direction $S_t(\theta,\phi)$ (see Eq. 3.2). Fan-beam scatterometers utilise a rectangular shaped antenna to concentrate the emitted power to a distinct direction. This direction is referred to as **boresight direction**, with the maximum power emitted, appearing as a single mainlobe in the radiation pattern. Nevertheless, antennas will also transmit and receive energy at angles away from boresight direction, indicated by sidelobes in the pattern. Of particular interest are the so called half-power points in boresight direction, at which the power radiated is reduced by a factor of $\frac{1}{2}$ from the peak value of the mainlobe. The angle between the half-power points is denoted as **half-power beamwidth** β or 3-dB field of view, which is inversely related to the size of the antenna [*Ulaby et al.*, 1981]. Hence, the projection of the half-power beamwidth β on the Earth's surface represents the surface footprint of the microwave antenna. In terms of a fan-beam configuration, this applies to each axis of the rectangular antenna, so that the half-power beamwidth in along-track direction β_h and across-track direction β_v is inversely related to the length l and width w of the antenna given by:

$$\beta_h = \frac{\lambda}{l} \quad \textit{and} \quad \beta_v = \frac{\lambda}{w} \,. \tag{3.14}$$

Precisely because the spatial resolution of a sensor refers to the size of the smallest possible feature that can be distinguished, a narrow beamwidth is preferred. As stated by equation 3.14, increasing the antenna size will accomplish a narrower beamwidth, which is a strict constraint for space-borne microwave systems. In the particular case of side-looking RADARs, information can also be extracted from within the radar beamwidth by making use of the ranging capability of the system. The received normalised radar cross section (σ^0) within the surface footprint in across-track direction is recorded as a function of time delay. This means that, energy recorded shortly after the transmission of the pulse will correspond to energy scattered back at beginning of the footprint and subsequent received energy originate from across the footprint. Figure 3.2 illustrates the interaction of a single pulse with the Earth's surface and the recorded signal received by the antenna. The length d_g of the surface projection of the transmitted pulse of a side-looking RADAR can be approximately given by:

$$d_g = \frac{\tau c}{\sin\theta} \,, \tag{3.15}$$

where τ is the pulse duration, c the speed of light and θ the incidence angle of the pulse with respect to the surface. In **range binning**, the recorded signal of the backscattered energy in across-track direction will be binned according to the time delay between transmission and reception of the pulse. It should be noted that, range binning only provides meaningful results if the width of the surface projection d_g of the pulse is smaller than the beamwidth in across-track direction β_v. The technique of range binning divides the recorded energy into equally spaced time bins, which are equivalent to range bins on the Earth's surface. As a result, the width of the range bins on ground define the actual **across-track resolution** or **range resolution** r_θ of a side-looking RADAR. Ultimately, the range resolution r_θ depends on the pulse duration τ, given by the following relationship.

$$r_\theta = \frac{d_g}{2} = \frac{\tau c}{2\sin\theta} \tag{3.16}$$

According to this relationship (see Eq. 3.16), as long as the distance between two targets is greater than the half of the projected pulse length, two targets will generate separate and identifiable returns. This becomes obvious due to the fact that, the pulse echo of the second target will travel a two-way distance of $2r_\theta$ more than the echo of the first target. Thus, the optimum across-track

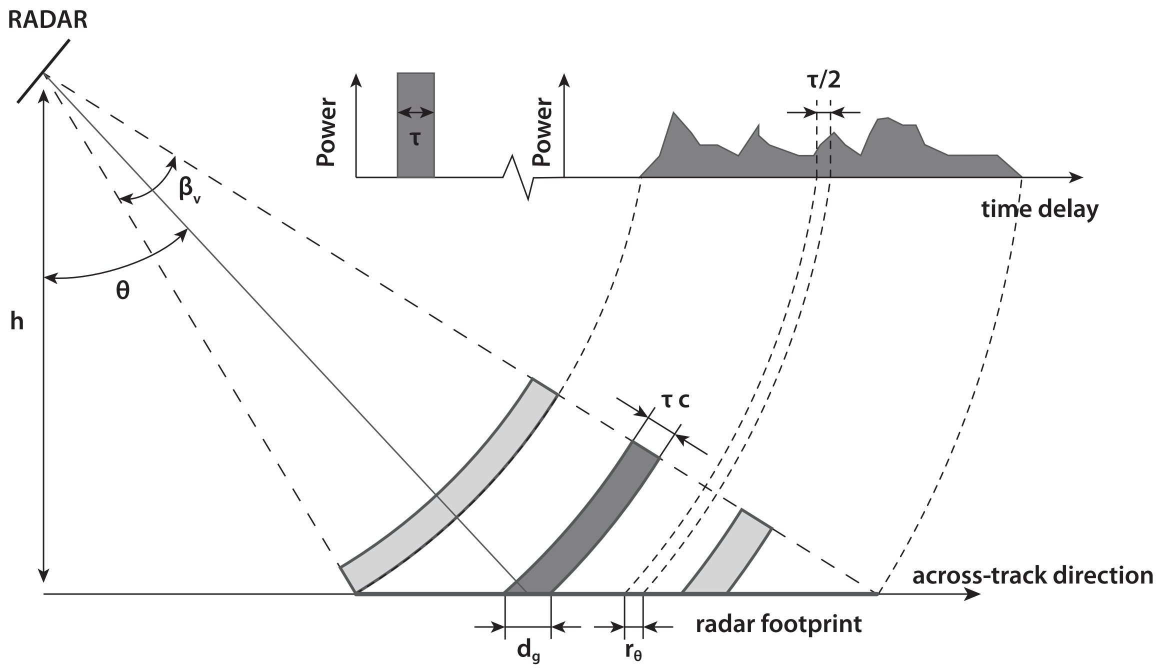

Figure 3.2: Determination of the spatial resolution r_θ in across-track direction for a side-looking radar. See text for further description.

resolution cannot be less than that specified in equation 3.16, even if the time bins are chosen to be very small. It also implies that the across-track resolution r_θ improves as the duration of the pulse decreases. However, the generation of very short pulses, to improve the range resolution, is in practice restricted by at least two factors, the frequency bandwidth and limitations related to the signal-to-noise ratio. A pulse has a frequency bandwidth inversely proportional to the pulse duration τ, hence as the pulse duration shortens, the required frequency bandwidth increases. Specifically within the 1-14 GHz radar frequencies, quite narrow frequency bandwidths are allocated by the responsible bodies, because of the large number of users within these frequency bands. Therefore, usable pulse durations are limited to avoid leakage into adjacent frequency bands. Secondly, short pulses require a high peak pulse power to guarantee a satisfactorily high signal-to-noise ratio level. In terms of space-borne instruments, where the power supply is limited, the creation of high peak pulse power is impracticable. As a consequence, many space-borne radar systems utilise a **pulse compression** method known as **linear frequency modulation** or chirp radar to overcome this restrictions. Such compression methods permit the creation of long pulses which combine the high energy level of long pulses with the high spatial resolution of short pulses. Within each pulse, the frequency is modulated linearly with time and the resulting chirp pulse will have the same integrated power and frequency bandwidth as the desired short pulse [*Ulaby et al.*, 1982]. After reception of the chirp pulse, the signal runs through a filter that reconstructs the short pulse. The chirp pulse has the same frequency bandwidth as the short pulse, but is longer, of higher power level and can be reconstituted into the desired single frequency short pulse.

The across-track resolution r_θ for scatterometers is optimised by utilising the ranging capability of the instruments. On the other hand, the **along-track resolution** r_ϕ of a scatterometer is governed by the physical size of the antenna in this direction. Accordingly, the along-track resolution r_ϕ or azimuth resolution is approximately given by:

$$r_\phi = \beta_h R = \frac{\lambda}{l}\frac{h}{\cos\theta} \tag{3.17}$$

3.5 Pulse Repetition Frequency (PRF)

As already mentioned, a scatterometer is designed to provided highly accurate backscatter measurements by averaging a large number of independent observed samples. The regular interval of observations is identified as τ_p and accordingly the **pulse repetition frequency (PRF)** is defined as:

$$PRF = \frac{1}{\tau_p}\ . \tag{3.18}$$

It is desirable to make as many observations as possible and accordingly increase the pulse repetition frequency, because multiple observations will increase the signal-to-noise ratio by averaging the returns. Certainly, the maximum PRF achievable with a side-looking radar is constrained by the across-track direction beamwidth. A schematic description of the determination of the maximum PRF is represented in figure 3.3. Two successive transmitted pulses are separated by τ_p which is equivalent to a slant-range distance of $d_p = \tau_p c$. In general, the recorded returns of a single pulse originate first from the near edge of the swath and later on from the far edge. If two successive pulses are transmitted with a too high PRF, the second pulse scattered back from the near edge of the swath is recorded before the echo of the first pulse from the far edge is returned resulting in an overlap of echoes. Overlapping echoes generate ambiguities in the returned signal, making the data worthless. To avoid ambiguities in the returned signal, the echo from the far edge of the first pulse has to be returned before the echo from the near edge of the second pulse returns, expressed with the following inequality:

$$d_p = \tau_p c\ >\ 2\left(R_2 - R_1\right)\ . \tag{3.19}$$

In terms of the PRF the equation becomes:

$$PRF < \frac{c}{2\left(R_2 - R_1\right)}\ , \tag{3.20}$$

with R_1 denoted as the slant-range distance to the near edge of the swath, R_2 the distance to the far edge of the swath and c the speed of light.

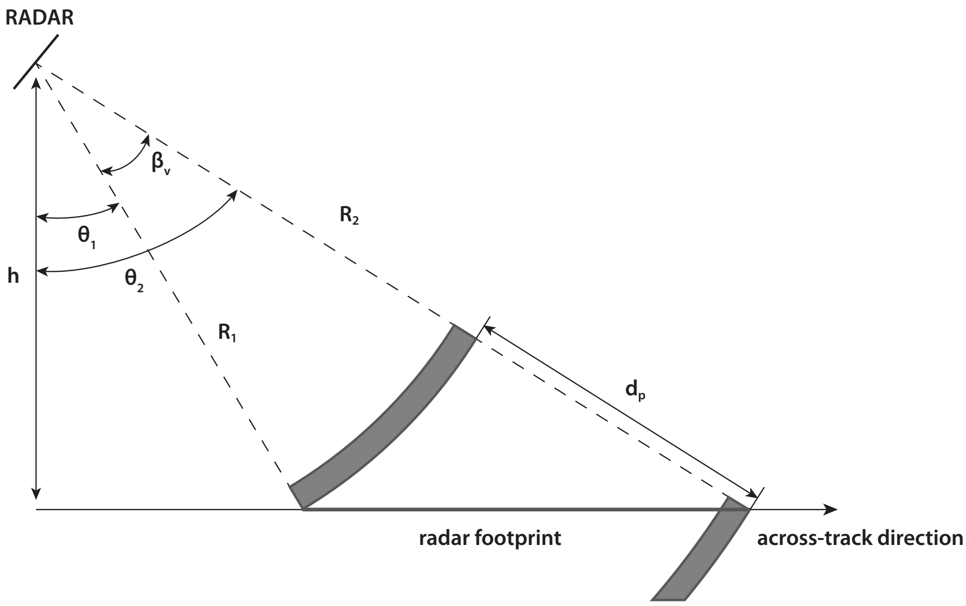

Figure 3.3: Determination of the maximum pulse repetition frequency (PRF) for a side-looking radar.

3.6 AMI-WS onboard the European Remote-Sensing Satellites

On 17 July 1991, ESA launched the first European Remote-Sensing Satellite (ERS) from the Kourou launch site in French Guiana [*Vass et al.*, 1992]. ERS-1 was the major forerunner of the present European satellites for environmental monitoring, with development and predecessor studies dating back to the early seventies [*ESA*, 2013]. It was the first European effort to acquire expertise in microwave remote sensing and to complement the already established optical and infrared observation systems. The **ERS-1 payload** carried an array of instruments for environmental monitoring of land, water, ice and atmosphere. The centrepiece of the ERS-1 payload was the Active Microwave Instrument (AMI), combining the functionality of a SAR and a Wind Scatterometer (WS). Other instruments onboard were a Radar Altimeter, an Along-Track Scanning Radiometer, a Precise Range and Range-Rate equipment and a Laser Retro-Reflector. The system was designed for a nominal lifetime of 3 years, but it was not until March 2000, that the ERS-1 mission ended after 9 years of excellent service due to a failure in the onboard attitude control system.

		unit	ERS-1	ERS-2	MetOp-A
Repeat cycle		[orbits]	43 501 2411	501	412
		[days]	3 35 168	35	29
Orbits/day		-	14.333 14.314 14.351	14.314	14.207
Ground velocity		[km/s]		7	
LMT at ascending node		-	22:15	22:30	21:30
Spacecraft mass		[kg]	2384	2516	4085
Payload mass		[kg]	1100		920
Launch date		-	17 July 1991	21 April 1995	19 October 2006
Mission end date		-	10 March 2000	4 July 2011	-

Table 3.1: ERS-1/2 and MetOp-A mission parameter overview.

Already on 21 April 1995 the follow-on mission **ERS-2** was launched, equipped with an almost identical payload as ERS-1, but with an additional sensor onboard for atmospheric ozone research. When they were launched, the two ERS satellites were the most sophisticated EO satellites ever developed and launched in Europe. In July 2011, after 16 years in space, ERS-2 was decommissioned and removed from its operational orbit, comprising, together with ERS-1, a Wind Scatterometer data archive of 20 years of Earth backscatter measurements. Both satellites were launched into an elliptical sun-synchronous orbit at approximately 785 km altitude and 98.5° inclination. Consequently, the nominal orbit period was approximately 100 minutes, with an ascending node (crossing of the Equator northwards) time of 22:15 local mean time (LMT) for ERS-1 and of 22:30 LMT for ERS-2 respectively. A standard orbit repeat cycle of 35 days was appointed for both satellites, supplemented with two other repeat cycles of 3 and 168 days specifically dedicated to ERS-1. An overview of mission relevant parameters is given in table 3.1.

3.6.1 Functional Description

As already mentioned, the **Active Microwave Instrument (AMI)** was the centrepiece of the ERS payload. It was designed as a multimode RADAR, operating at a frequency of 5.3 GHz (C-Band), by combining the functionality of a high resolution SAR and a low resolution **Wind Scatterometer** [*Attema*, 1991]. AMI SAR operations were performed in two distinct modes: image and wave. In wind mode, AMI was configured as a Wind Scatterometer to provide backscatter measurements of the Earth's surface. The image and wind mode were mutually exclusive due to the high power consumption and data rate required for high resolution SAR image acquisition. Nevertheless, AMI could operate in a wind/wave mode, in which wind and wave mode were operated sequentially, enabling simultaneous characterisation of the wind and wave fields over the oceans. Measurements in wind mode were acquired with three sideways looking, vertically polarised fan-beam antennas, one looking perpendicular to the right with respect to the satellite track (**Mid-beam**), one looking forward at 45° angle (**Fore-beam**) and one looking backward at 135° angle (**Aft-Beam**) illuminating a 500 km wide swath (see Fig. 3.4). The transmitter unit of the scatterometer generated a rectangular radio frequence pulse with a duration of 130 μs for the Fore- and Aft-beam and of 70 μs for the Mid-beam antenna. The three antennas were operated in sequences of 32 radio frequency pulses each, starting with the Fore-beam antenna. The pulse repetition frequency (PRF) was chosen to be 98 Hz for the side antennas and 115 Hz for the mid antenna, resulting in a total repeat cycle length of 940.84 ms referred to as **FMA sequence**. Four FMA sequences last 3.763 s, which correspond to approximately 25 km along the ground track of the satellite. During each beam sequence of 32 pulses, 4 internal calibration pulses and 28 noise signals were measured [*Lecomte and Wagner*, 1998]. The internal calibration pulse was a replica of the transmitted pulse fed into the receiver chain. The aim was to monitor the power of the transmitted pulse and the receiver gain to guarantee instrument stability during the mission, hence the term internal calibration. Noise measurements were necessary to account for thermal radiation superimposing the received echo signal to improve the signal-to-noise ratio. An analogue to digital converter (ADC) was used to sample the echo signal, the internal calibration pulses and the noise measurements at 30 kHz. A sampling of the received echo signal at 30 kHz correspond to a across track resolution of approximately 32.4 km at 18° incidence angle and 14 km at 45.5° incidence angle for the Mid-beam.

3.6.2 Ground Processing

Onboard tape recorders were used to store the sampled echo signals, the internal calibration pulses and the noise measurements after various onboard processing steps. These data packages were down-linked to ground stations for further on-ground processing, supplied by external data (orbit and attitude information) and characteristics of the instrument, in order to achieve the required system performance. In a first attempt, various fundamental signal processing steps were performed to improve the signal-to-noise ratio and correct for transmitter and receiver chain fluctuations (internal calibration). Subsequently, the power echo samples were converted to the normalised radar cross section, σ^0, by predetermined normalisation factors. The normalisation factors were defined as the power at the input equal to a uniform reference backscatter coefficient of unity on the Earth's surface. These normalisation factors are a function of changing geometry along the orbit for a given antenna (see Eq. 3.12) provided as Look-Up-Tables. In a further processing step, a spatial filter was applied to the σ^0 samples to increase the radiometric resolution and achieve the desired point target response along a grid of nodes, representing the entire swath. Calculation of the position of each node in the swath was based on the Mid-beam antenna. The central node position of the swath was determined at the intersection of the Mid-beam boresight direction with the Earth's surface. From this central node, more nodes are computed at every 25 km arc distance towards the near and far edge of the swath, along a perpendicular oriented line with respect to the satellite ground track. This is repeated after 4 FMA sequences, corresponding to an along track node interval of 25 km. Once the node positions within the swath were determined, the σ^0 samples located within a certain area around a node are averaged in along and across-track direction using a so-called Hamming function (see Eq. 4.1) for each antenna beam. The aim of this function is to apply weights to various σ^0 samples, according to their distance to the regarded node. Ultimately, each node in the swath holds a σ^0 value of each antenna beam referred to as σ^0-triplet. This processing step is of major importance, due to the fact that it impacts the characteristic of the σ^0 values and particularly the final spatial resolution of the product. A detailed discussion about the ground on-processing steps of ERS AMI-WS data packages can be found in *Lecomte and Wagner* [1998] and *Neyt et al.* [2002].

3.7 ASCAT onboard the Meteorological Operational Platform

In 2003, the National Oceanic and Atmospheric Administration (NOAA) and the European Organisation for the Exploitation of Meteorological Satellites (EUMETSAT) signed an agreement to provide an operational polar-orbiting service referred to as Initial Joint Polar System (IJPS). The objective of the IJPS is to provide and improve operational meteorological and environmental forecasting and global climate monitoring services by contributing to and supporting of the following programs:

- the Word Meteorological Organisation (WMO) Global Observing System,
- the Global Climate Observing System (GCOS),
- the United Nations Environmental Programme (UNEP),
- the Intergovernmental Oceanographic Commission (IOC),
- and other related programs

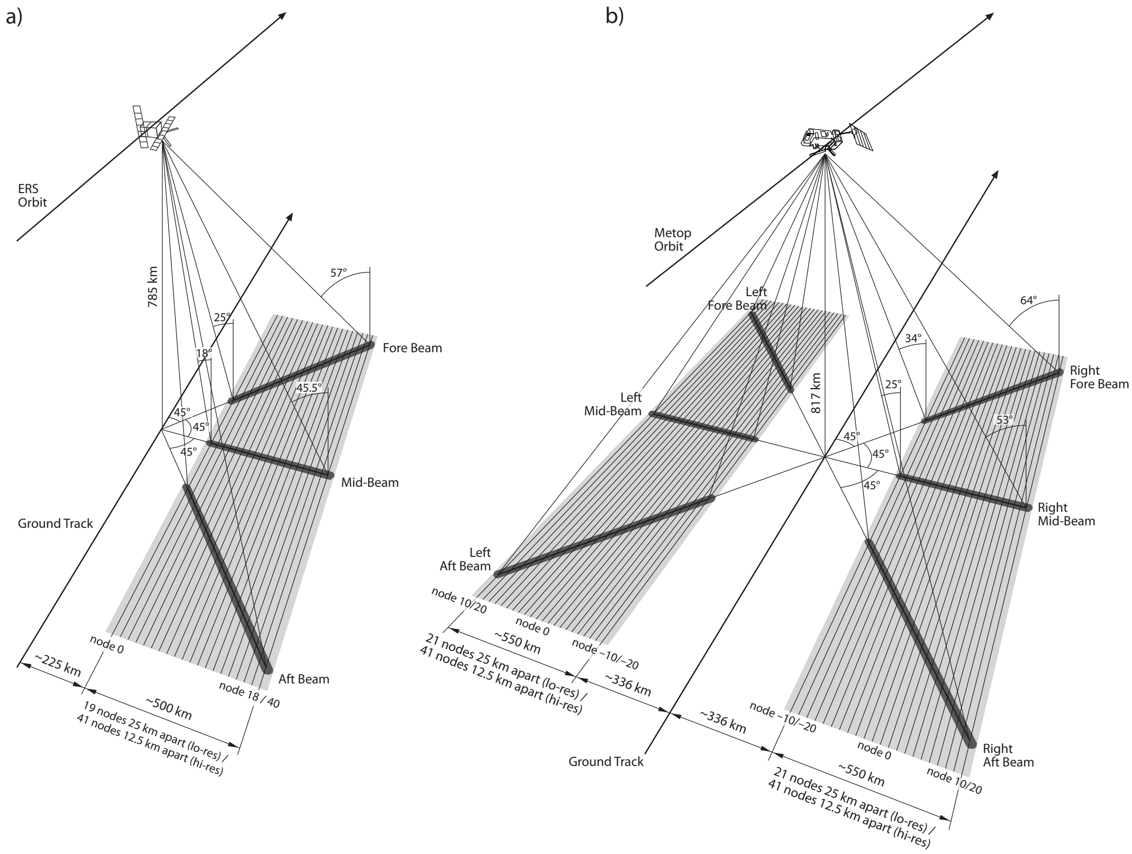

Figure 3.4: Instrument configuration of a) ERS AMI-WS and b) MetOp ASCAT after *Bartalis* [2009a].

The European contribution to IJPS is called EUMETSAT Polar System (EPS), consisting of a ground component and a space component. A series of three satellites, the Meteorological Operational Platform (MetOp), are part of the space component of EPS, which were jointly developed by EUMETSAT and European Space Agency (ESA) [*Klaes et al.*, 2007]. The cooperation of NOAA and EUMETSAT foresees the exchange of common payload elements. As a result, MetOp carries a set of instruments (AVHRR/3, AMSU-A, HIRS/4, MHS) provided by the United States to achieve continuity to previous operational measurements and a new generation of European instruments, developed from the heritage of proven research missions on the ERS satellites.

The MetOp satellites fly in a sun-synchronous mid-morning orbit (crossing of the Equator southwards at 09:30 LMT) at a mean altitude of 820 km and an inclination of about 98.7°, whereas the American satellites cover the afternoon orbit (21:30 LMT). MetOp-A and MetOp-B were already successfully launched on 19 October 2006 and on 17 September 2012 respectively. These two satellites currently operate in parallel in the same orbital plane with a time shift of about 50 minutes (half a orbit). The nominal lifetime of each MetOp satellite is 5 years, but it is foreseen to operate MetOp-A as long as available capacities bring benefits to the user. The third satellite, MetOp-C, is due to be launched in 2018 to ensure continuity in the long-term monitoring of geophysical factors, important for climate change research and assimilation into numerical weather prediction models at least until 2020.

3.7.1 Functional Description

The Advanced Scatterometer (ASCAT) is one of the new generation of European instruments onboard MetOp. The design of ASCAT is based on the robust and well-understood concept of AMI-WS onboard the ERS satellites [*Figa-Saldaña et al.*, 2002]. With respect to the experience obtained during the operations of AMI-WS and the intensive use of the data, the technical design of ASCAT include various improvements compared to its predecessor which are listed as follows:

- Continuous data acquisition and product generation without sharing operation time in orbit with other instruments.
- Increased spatial coverage by the advantage of a double swath configuration.
- Higher incidence angle range to improve the performance of the wind-retrieval algorithm.
- Generation and dissemination of a research product at a higher spatial resolution (25 km).
- Instrument design improvements resulting in higher instrument stability and reliability.
- Improved onboard processing to allow for a lower data rate.

Like the AMI Wind Scatterometer, ASCAT is a fan-beam scatterometer operating in C-band at 5.255 GHz using vertically polarised antennas. While AMI-WS was sharing the operation time in orbit with the onboard SAR, ASCAT operations onboard MetOp are exclusive. Furthermore, the amount of antennas was doubled, resulting in a left and right swath illuminated by three side-looking antennas each. The ASCAT sensor has two antennas looking perpendicular with respect to the satellite track (**Mid-beam**), two looking forward at 45° angle (**Fore-beam**) and two looking backward at 135° angle (**Aft-beam**) illuminating a 550 km wide swath (see Fig. 3.4). ASCAT incidence angles range from 25° to 53° in the mid-beam antennas and from 34° to 64° in the Fore- and Aft-beam antennas. It should be noted that, the central frequency of the transmitted pulses of ASCAT is slightly shifted of about 45 MHz with respect to AMI-WS.

Furthermore, ASCAT utilise linear frequency modulation technique, referred to as **chirp** (see chapter 3.4), for pulse transmission to produce long (10 msec) and low peak power (120W) pulses. The received ground echoes are de-chirped by mixing with a delayed image of the transmitted pulse and the resulting echo power spectrum is sampled and analysed to provide the require range resolution. Knowing the chirp rate and the Doppler-frequency, each frequency in the power spectrum can be mapped into slant range information [*Gelsthorpe et al.*, 2000; *Rostan et al.*, 1999]. Additionally, ancillary information about internal calibration and noise measurements are record within each pulse repetition interval (see Tab. 3.2) to monitor the instrument stability and guarantee high quality measurements. An onboard data pre-processing of the echo and noise measurements achieve a considerable data rate reduction of the raw data by a factor of 25. The pre-processed data, together with the internal calibration information, is downlinked for further on-ground processing to produce higher level products.

3.7.2 Ground Processing

It is worthwhile to mention that ASCAT is operated in two modes, namely measurement mode and calibration mode. In measurement mode, which is the standard operation mode, ASCAT generates two types of downlinked data packets, echo and noise packets. In the on-ground processing, measurement noise subtraction is carried out and the data is corrected for variations of the transmitter power and receiver chain gain by using the internal calibration information. The resulting power measurements are converted to normalised radar cross section (σ^0) values using normalisation functions accounting for instrument configuration related parameters and the current satellite orbit. Subsequently, these raw σ^0 backscatter measurements are localised on the Earth's surface, for each antenna and a single orbit, by utilising the Goddard Earth Model 10 (GEM10) and a model to predict the satellite orbit, resulting in the so-called ASCAT Level-1B full resolution product. On the base of this product, further two Level 1 products are generated by spatial resampling to an equidistant orbit grid with appropriate spatial and radiometric resolutions. Like for AMI-WS, the spatial resampling is done by the use of a two-dimensional weighting function, centred at the position where the interpolated σ^0 values are to be produced. The weighting function is realised as the product of two one-dimensional Hamming functions (see Eq. 4.1), one oriented across-track direction and the other along-track. The final operational Level-1B product is fully radiometric calibrated with a spatial resolution of 50 km provided on a equidistant orbit grid with a spacing of 25 km to comply the Nyquist sampling theorem. Each grid node of the product is holding a triplet of σ^0 values constituted from the three antenna beams of one swath. An additional Level-1B research product is also made available with a spatial resolution of 25 km and a grid spacing of 12.5 km [*EUMETSAT*, 2013].

	unit	AMI-WS	ASCAT
Frequency	[GHz]	5.3	5.255
Wavelength	[cm]	5.66	5.7
Chirp rate	[kHz/ms]	-	50
Polarisation	-	VV	VV
Peak Power Pulse	[W]	4800	120
Pulse Duration	[μs]	70 (mid) 130 (fore/aft)	10000
PRF	[Hz]	115 (mid) 98 (fore/aft)	5
Incidence Angle	[deg]	18-47 (mid) 25-59 (fore/aft)	25-53.5 (mid) 33.7-64.5 (fore/aft)
Antenna Angle w.r.t ground track	[deg]	45 (fore) 0 (mid) -45 (aft right)	45 (right fore) 0 (mid right) -45 (aft right) 135 (fore left) 180 (mid left) -135 (aft left)
Swath width	[km]	500	550
Swath offest from ground track	[km]	200	336
Radiometric Stability	[dB]	0.46	0.46
Radiometric Accuracy	[dB]	-	0.57
Radiometric Resolution	[%]	6.5 - 7.0	3.0

Table 3.2: Overview of AMI-WS and ASCAT technical parameters

3.8 External Calibration of AMI-WS and ASCAT

The objective of **radiometric calibration** of a space-borne scatterometer is to determine the relationship between the raw instrument recordings and the physical quantity of interest the normalised radar cross section (σ^0). Different calibration strategies are trailed during the lifetime of a space-borne scatterometer as already introduced in chapter 2.4, highlighting the importance of post-launch calibration activities to achieve the mission requirements.

$$\sigma^0 = \frac{P_r}{P_t}\frac{(4\pi)^3 R^4}{AG^2\lambda^2} \,. \tag{3.21}$$

Any error associated with a parameter in the monostatic RADAR equation, provided for convenience in equation 3.21, will produce an error in the deduced normalised radar cross section σ^0. Errors associated to the transmitted power P_t and the received power P_r are carefully monitored onboard of a scatterometer in terms of frequent internal calibration pulses. This internal calibration enable the control of system gains and attenuations of the transmitter or the receiver chain in the on-ground processing. The effective power transmitted and recorded by a monostatic RADAR configuration is governed by the antenna gain pattern $G(\theta,\phi)$. As internal calibration bypass the antennas, external calibration is crucial to determine and monitor the antenna gain pattern as a function of incidence and azimuth angle. In terms of AMI-WS and ASCAT, **active transponders** are used to gather information about the directional characteristics of the antenna gain pattern referred to as absolute calibration. Active transponders provide a stable and accurately known point target cross section. During an overpass, the transponder tracks the satellite and receives calibration signals transmitted by the scatterometer. After receiving the calibration signal, the transponder will wait a fixed time interval and send back a signal of precisely known cross section determined by the transponder [*Anderson et al.*, 2012; *Manise et al.*, 2004; *Rostan*, 2000; *Wilson et al.*, 2010]. Absolute calibration of AMI-WS was performed using two transponders located in Spain, while in terms of ASCAT calibration three transponders, located in Turkey, are used. The transponder positions are chosen in a way to optimise the sampling of the antenna gain pattern $G(\theta,\phi)$ of each antenna with respect to the repeat cycle of the particular instrument.

To perform **absolute calibration**, the instrument has to be switched to calibration mode, which is similar to the nominal measurement mode but with a different antenna duty cycle. Calculation of the required antenna gain pattern $G(\theta,\phi)$ of each antenna requires three processing steps, including the generation of normalisation factors to convert the raw instrument records to calibrated σ^0 values. First, calibration data from a single transponder overpass (see Fig. 3.5-a) of the satellite is processed to give **antenna gain values** in the nominal antenna coordinate system, characterised by the azimuth and elevation angle with respect to the boresight direction of the antenna. Each overpass represents a cut through the antenna gain pattern at a particular eleva-

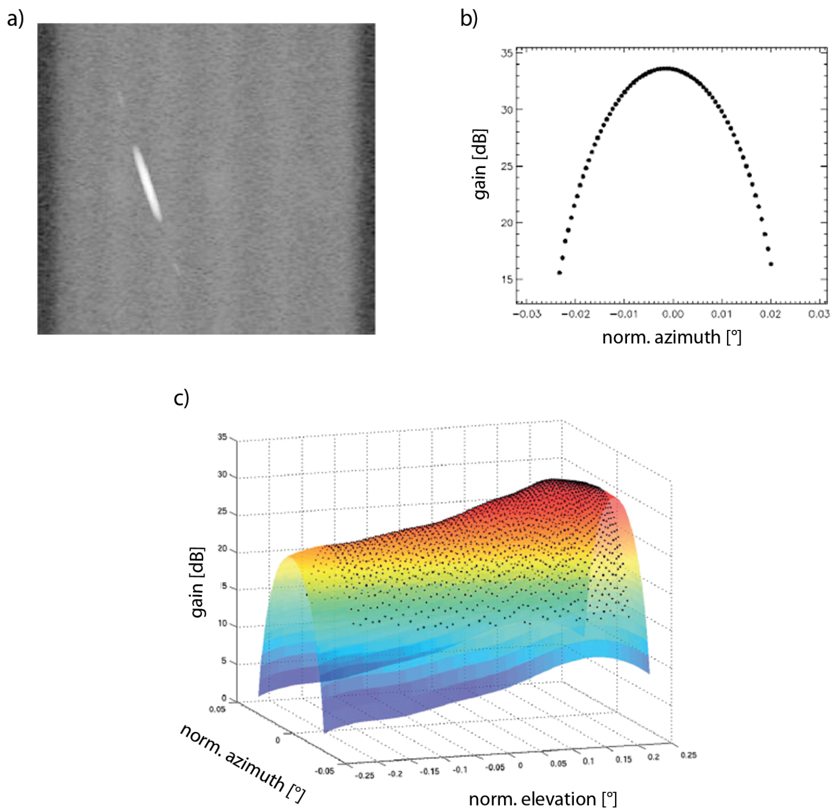

Figure 3.5: Estimation of the antenna gain pattern $G(\theta,\phi)$ using active transponders from *Anderson et al.* [2012].
a) image of a transponder signal recorded by MetOp-A ASCAT
b) antenna gain as function of azimuth angle, representing a cut through $G(\theta,\phi)$
c) gathered transponder data with the fitted antenna gain model

tion angle and various azimuth angles as shown in figure 3.5-b. Gathering a number of transponder overpasses will result in a well sampled antenna gain pattern in azimuth and elevation angle. After gathering a sufficient amount of transponder cuts, in a second step an **antenna gain model** is fitted to the data values (see Fig. 3.5-c). Furthermore, antenna pointing errors are modelled based on power spectrum analysis of the gathered overpasses. The location of the maximum energy in the power spectrum depends on the slant range distance between the transponder and the instrument as well as on the Doppler frequency shift of the signal. Hence, the location of the maximum energy in the power spectrum can be used to estimate the transponder positions out of the power spectrum. Any deviations of the known transponder positions from the estimated positions are referred to as antenna pointing errors. Consequently, calibration using active transponder enables the antenna gain patterns to be monitored, along with the boresight pointing and the precise orientation of the antennas. Finally the derived antenna gain patten models are used to obtain **normalisation factors** to convert the raw power measurements into calibrated σ^0 values. The calculation of these normalisation factors is based on the assumption of Earth's backscatter to be unity ($\sigma^0 = 1$). With this assumption and the derived antenna gain patterns an estimate of the measured signal is determined. Differences between the predicted and the actual signal measured by the scatterometer are taken to be a result of the Earth's backscatter not being unity. Moreover, the actual signal divided by the predicted signal gives an estimate of the normalised radar cross section of the Earth's surface. Accordingly, the predicted signal is the required normalisation factor used to calculate σ^0-values from the raw power measurements of the instrument [*Anderson et al.*, 2012; *Lecomte*, 1998]. Normalisation factors are calculated for various standard orbits, to account for variations in satellite attitude and geometry, and are provided as look-up-table to the on-ground processor.

A limitation of absolute calibration is that calibration corrections are provided at distinct positions in the antenna pattern and not continuously. These distinct positions are given by the measured transponder cuts of the scatterometer for each antenna. Specifically in the ERS scatterometer era, a supplementary calibration approach was chosen referred to as **relative calibration**. The aim of relative calibration is to infer a continuous antenna pattern across the swath by the use of natural extended area land-targets such as the Amazon Rainforest [*Anderson et al.*, 2012; *Crapolicchio et al.*, 2012; *Lecomte and Wagner*, 1998]. At C-band densely vegetated regions, are assumed to act like a pure volume scatterer, scattering the incoming signal equally in all directions. As a consequence, the measured backscatter response will depend on the area A^0 effectively seen by the instrument and is linked to the incidence angle by the so-called gamma nought model expressed by:

$$\gamma^0_{linear} = \frac{P}{A^0} = \frac{P}{A\cos\theta} = \frac{\sigma^0_{linear}}{\cos\theta} \,. \tag{3.22}$$

The subscript $linear$ should indicate that the gamma nought model γ^0 (see Eq. 3.22) is valid for backscatter measurements in the linear domain and not in the commonly used logarithmic domain (see Eq. 3.13). Under the assumption of isotropic backscatter behaviour of Amazon Rainforest and consequently the validity of the gamma nought model, the derived γ^0 backscatter coefficients can be compared regardless of the viewing geometry, incidence and azimuth angle, of the measurements. Furthermore, it was found that the isotropic γ^0 backscatter response of the Amazon Rainforest is approximately constant with respect to time and spatial location [*Hawkins et al.*, 2000]. Analysis of the γ^0 backscatter coefficients, concentrating on the residual incidence angle dependency, allow a continuous monitoring of antenna gain pattern variations during the mission lifetime, since γ^0 coefficients should result in a flat pattern across the swath. Any deviations to the assumed flat behaviour are considered as calibration inaccuracies which have to be corrected for (see Fig. 3.6a). The overall instrument performance can be monitored by computing the peak position of the γ^0 histogram of weekly or monthly aggregated data individually for each antenna beam (see Fig. 3.6b).

a)

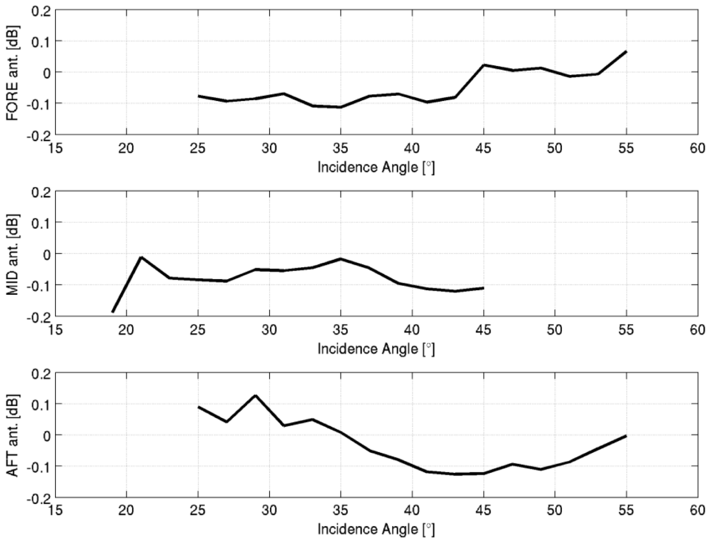

b)

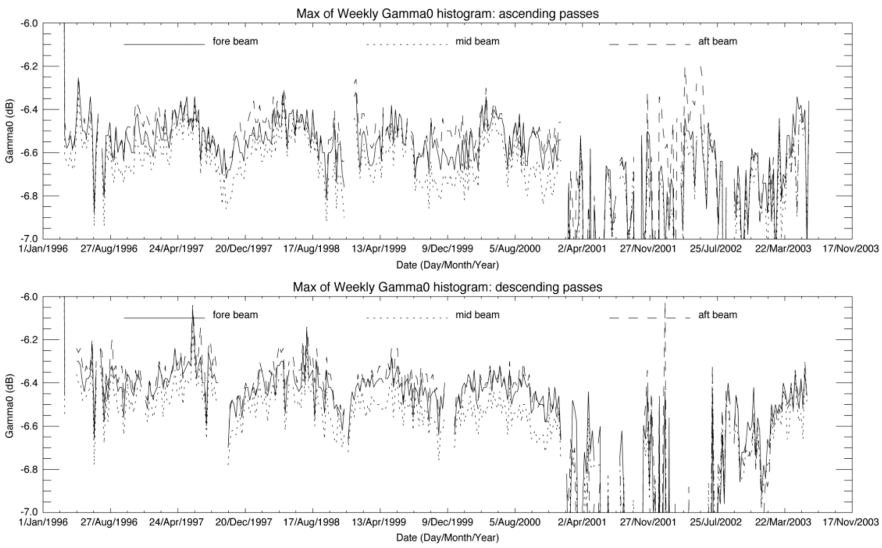

Figure 3.6: ERS-2 AMI-WS relative calibration results over Amazon Rainforest from *Crapolicchio et al.* [2012].
a) antenna gain pattern drifts between 1996 and 2011 for ascending overpasses
b) temporal evolution of the γ^0 histogram peak

Chapter 4

Calibration Methodology

4.1 Overview of the Chapter

Already established external calibration methods of AMI-WS and ASCAT are outlined in the last section of the previous chapter. The objective of this chapter is to introduce a stepwise relative calibration methodology by taking advantage of natural extended area land-targets. Data archives examined within this work and preceding data preparations are stated, before concentrating on the selection of extended area land-targets appropriate for relative calibration. Requirements on extended area land-targets applicable for radiometric calibration of space-borne scatterometers are discussed in detail, resulting in three parameters specifying the backscatter characteristics of land-targets. In addition, a threshold based selection scheme is presented, identifying a number of extended area land-targets suitable for C-band scatterometer calibration. Finally, the proposed calibration methodology is introduced, highlighting the major objectives of the different calibration steps. The elaborated calibration methodology can be distinguished into sensor intra-calibration and sensor inter-calibration.

4.2 Introduction

The aim of this study is to support and advance post-launch calibration methods already established by ESA and EUMETSAT, concentrating on space-borne scatterometers onboard of ERS-2 and MetOp-A. Both agencies are endeavouring to provide accurate measurements of the NRCS, sigma nought (σ^0), by means of routinely performed calibration campaigns. In terms of ASCAT, calibration campaigns by the use of active transponders are scheduled on a regular interval every 12 to 18 months [*Wilson et al.*, 2010]. Such campaigns are of fundamental importance to characterise the overall system performance and to estimate all relevant calibration quantities to derive calibrated σ^0 measurements. However, these campaigns depict only a snapshot of the performance of the instrument at a specific period of the mission. Instrument variations between consecutive campaigns, if unaccounted for in the on-ground processing, will result in calibration deficiencies degrading the accuracy of backscatter observations. The accuracy of retrieved Level 2 scatterometer products, such as surface soil moisture or wind vector fields, will suffer from these calibration related deficiencies, leading to artificially introduced increases or decreases in the quantity of interest. Such sensor related drifts have to be identified and corrected for with regard to the creation of long-term consistent datasets for climate change research. In the worst case, artificial increases or decreases in a climate record could be falsely interpreted as an anomalous event due to climate change, although the climate is stable and only the sensor characteristics changed.

Within this work, a calibration methodology is presented, aiming to continuously infer calibration parameters of ERS-2 and MetOp-A scatterometers, to capture and correct for instrument related variations reflected in the σ^0 backscatter coefficient. The proposed calibration strategy closely follows the principle of relative calibration in terms of using natural extended area land-targets, indicated by a temporal stable and homogeneous σ^0 response over an extensive area. Moreover, the calibration strategy is a stepwise calibration methodology, with the objective to ensure consistent calibrated σ^0 observations of a specific mission and secondly consistency across different scatterometer missions. Consistency of σ^0 backscatter coefficients of a specific mission is achieved by means of sensor intra-calibration. Scatterometer intra-calibration intends to account for calibration anomalies of individual antenna beams and between different antennas, unconsidered in the normalisation factors used in the on-ground processor. Similarities in the instrument technical design of AMI-WS and ASCAT encourage a merging of these European scatterometer missions towards a long-term consistent backscatter dataset comprising more than 30 years of global data. As a consequence, a second calibration procedure is introduced, referred to as sensor inter-calibration, with the objective to identify possible calibration related differences between two scatterometer missions. Sensor inter-calibration carefully analyses potential biases between two missions and correct σ^0 backscatter coefficients of one scatterometer mission with respect to a established calibration reference mission.

4.3 Data and Data Preparation

Scatterometer data investigated in this work originate from ERS-2 AMI-WS and from MetOp-A ASCAT. Both datasets provide σ^0-triplets, comprised of Fore, Mid and Aft-beam coefficients, at a spatial resolution of approximately 25 km localised in an orbit grid, which is defined with respect to the satellite orbit by the on-ground processor. Unforeseen events during the ERS-2 mission and the need for high quality products lead ESA to develop the Advanced Scatterometer Processing System (ASPS) project [*Crapolicchio et al.*, 2005; *De Chiara et al.*, 2007]. Initially a failure of the Attitude and Orbit Control System (AOCS) of ERS-2, on January 2001, caused ESA to review the former implemented on-ground processor called Stand-alone—Low bit Rate Data Pro-

Instrument	Data Format	Spatial Resolution	Spatial Coverage	Temporal Coverage
AMI-WS	ASPS	25 km	Global	20/05/1997 - 17/02/2003
ASCAT	EPS	25 km	Global	01/01/2007 - 31/11/2012

Table 4.1: Overview of ERS-2 and MetOp-A scatterometer data investigated in this study.

cessing Facility (S-LRDPF). At this time, the ERS-2 satellite was piloted in the so-called Zero Gyro Mode (ZGM) with slightly degraded attitude in particular for the yaw angle. Consequently, the derived σ^0 backscatter coefficients were not calibrated due to the satellite mispointing. To guarantee the continuity of the ERS-2 mission, a new on-ground processor, called ERS Scatterometer Attitude Corrected Algorithm (ESACA), was implemented in August 2003 with a yaw angle estimation module to process data acquired in ZGM. A malfunction of the onboard tape recorders in July 2003 further restricted the availability of the data. Acquired data in this period is restricted to the visibility of the satellite to ground stations for a direct downlink of the measurements. The initial global coverage of the ERS-2 scatterometer was reduced to regional coverage, determined by the available ground stations. For those reasons, an upgraded version of the ESACA processor was implemented into the ASPS, to handle data acquired in the ZGM and to provide best quality data during the regional coverage scenario of ERS-2. It should be noted that the S-LRDPF was based on a large number of pre-computed off-line parameters, such as the normalisation factors to derive σ^0 values, while the ESACA computes these parameters on the fly since the satellite is piloted in ZGM. Hence, a reprocessing of the entire ERS-1/2 missions was envisaged by ESA to provide a homogeneous long-term dataset of σ^0 backscatter coefficients to the scientific community processed with a state of the art on-ground processor facility. Level 1 AMI-WS data used in this study are reprocessed ERS-2 data computed with the ASPS facility, comprising σ^0 backscatter observations from May 1997 to February 2003. The data is disseminated in the corresponding ASPS data format in nominal (50 km) and high (25 km) spatial resolution, but only the high resolution scientific product is considered in this study.

EUMETSAT operationally disseminates Level 1 MetOp ASCAT products in various formats and by different telecommunication networks to the users. Within this study, Level 1 data, distributed via the EUMETSAT Data Centre, with a spatial resolution of 25 km, ranging from the beginning of the MetOp-A mission, January 2007, until November 2012 are included. The available product format is called native EPS-format, in which each file is containing a complete ASCAT orbit of σ^0-triplets of the left and right swath antenna beams of the instrument on an orbit grid. These orbit files are generated with the ASCAT on-ground processor in near real time after sensing. The on-ground processor software has been updated since start of the MetOp-A ASCAT mission with respect to some minor algorithmic improvements and the implementation of up-to-date calibration parameters. One of the major updates during operations was the transition to the in-flight estimation of σ^0 normalisation factors in September 2009. While previous normalisation factors are based on a reference orbit provided as static look-up-table to the on-ground processor, the actual processor version is capable to compute these factors on the fly by utilising the actual MetOp orbit. This on-ground processor transition is comparable to the transition from S-LRDPF to ESACA for AMI-WS data processing.

Level 1 products of both scatterometer missions are supplied in a satellite orbit defined grid with a grid spacing of 12.5 km. However, the present study requires temporal analysis of the datasets on a fixed Earth grid. For this purpose, the Level 1 σ^0-triplets are resampled to a Discrete Global Grid (DGG) developed by Vienna University of Technology (TU-Wien) for surface soil moisture (SSM) retrieval [*Kidd*, 2005]. The developed fixed Earth grid is based on the Goddard Earth Model 6 (GEM6) to accurately model the physical shape of the Earth surface. The grid consists of 3264391 grid points identified by a unique Grid Point Index (GPI) and an equal spacing of 12.5 km between neighbouring grid points in longitude and latitude. Data resampling from orbit to the fixed Earth grid is performed by searching the nearest orbit grid points for each GPI within a predefined 18 km radius. Finally, values of the backscatter coefficient, incidence angle and azimuth angle on the fixed Earth grid are obtained as weighted average of the nearest orbit grid points. The weighting coefficients $w(x)$ are derived by the Hamming window function express by:

$$w(x) = 0.54 + 0.46\,\cos\left(2\pi\frac{\delta x}{r}\right). \tag{4.1}$$

In the Hamming window function, δx denotes the distance between the orbit grid point and the actual GPI and r is the radius of the nearest neighbour search window. With this resampling method a time series of σ^0-triplets is generated for each grid point (GPI) over land on the fixed Earth grid, separately for each European scatterometer mission. Hereafter, any data analysis or computations related to σ^0 backscatter coefficients are referred to the derived σ^0 time series localised on the DGG.

4.4 Selection of extended area Land-Targets for Calibration

Post-launch calibration campaigns using active transponders is one traditionally followed external calibration approach. Transponders are active electronic devices constructed of antennas with auxiliary electronic equipment, acting as artificially point targets with a controlled, well known and temporal stable NRCS. A second key approach for post-launch calibration, often referred to as relative calibration, is based on the use of extended area land-targets with unique backscatter characteristics. Investigations about extended area land-targets suitable for external calibration of scatterometers were carried out since the early stages of space scatterometry. Data of the first space-borne scatterometer S-193 onboard NASA's Skylab mission showed, that Amazon Rainforest exhibit a stable and homogeneous radar response over an extended area. Later studies,

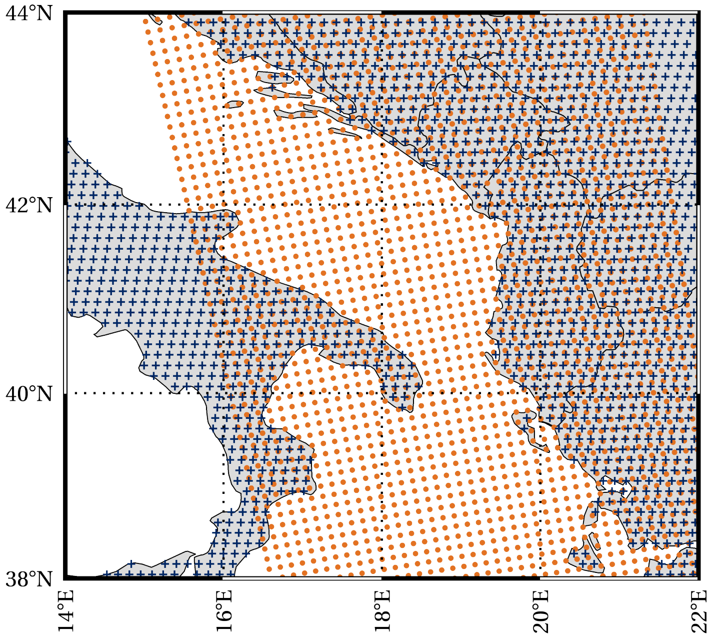

Figure 4.1: Orbit grid points [orange dots] and Discrete Global Grid points (GPIs) [blue crosses] over Adriatic Sea, Italy, Croatia, Albania, Montenegro, Bosnia-Herzegovina.

based on different types of RADAR instruments, confirmed these unique radar response properties and recommended Amazon Rainforest as natural extended area land-target for calibration [*Birrer et al.*, 1982; *Frison and Mougin*, 1996; *Hawkins et al.*, 2000]. *Kennett and Li* [1989a] intensively examined backscatter data, recorded by the Seasat-A Satellite Scatterometer (SASS), by global statistical analysis and proposed the following requirements related to natural calibration targets over land [*Kennett and Li*, 1989b]:

- σ^0 should be known at radar frequency, polarisation and incidence angle of interest.
- The dependency of σ^0 on azimuth angle should be small and well understood.
- The calibration target should have a large spatial extent.
- Spatial variations of σ^0 within the target should be small and well understood.
- σ^0 dependency on the time of the year should be known.
- σ^0 dependency on the time of the day should be known.
- The target conditions should remain constant during the missions.

In a strict sense, the proposed requirements claimed for natural calibration targets reflect the backscatter characteristics of active transponders utilised for absolute calibration. Hence, natural targets featured with these specific backscatter characteristics are treated as a calibration reference supposed to be applicable for relative calibration of scatterometers. In the present study, backscatter observations of AMI-WS and ASCAT are analysed to select extended area land-targets for radiometric calibration under consideration of the proposed requirements stated by

Kennett and Li [1989b]. Analysis of backscatter measurements concentrate on azimuthal anisotropic backscatter effects, the mean observed radar backscatter response and the temporal variability of σ^0 measurements. The objective of this analysis is to derive a set of parameters for the selection of extended area land-targets suitable for external calibration of the European C-band scatterometers AMI-WS and ASCAT. A so-called azimuthal anisotropy parameter δ is introduced, characterising natural land-targets backscatter response in terms of different azimuth angle acquisitions. Active transponders emit a constant backscatter response in arbitrary azimuth directions, but it is known that numerous land-targets do not exhibit a uniform backscatter response with respect to the azimuth angle [*Bartalis et al.*, 2006]. Thus, an azimuthal isotropic backscatter behaviour is crucial to infer possible biases between measurements recorded by different antennas of a fan-beam scatterometer. Even more important is the requirement of a small and well known backscatter dependency over time to assure the predictability of the backscatter coefficient σ^0 at any time of the year. In general, the normalised radar cross section (NRCS) of natural land-targets is controlled by the predominate land cover and geophysical processes affecting the scattering properties, resulting in a time dependent backscatter coefficient. Quantitative analysis of land cover dynamics and geophysical processes affecting the normalised radar cross section will be undertaken with respect to the observed long-term mean backscatter $\overline{\sigma^0}$ and the corresponding temporal variability parameter ν. With reference to applicable natural calibration targets, a long-term stable backscatter signature is demanded, supposed to be unaffected by target related dynamics, maintaining the predicted mean backscatter coefficient $\overline{\sigma^0}$ over time. Furthermore, it is postulated that the predicted mean backscatter response $\overline{\sigma^0}$ of an applicable calibration target is exclusively constrained by the absolute accuracy of the instrument to represent the true NRCS of a target. As a consequence, external calibration by means of natural land-targets is referred to as relative calibration. Moreover, to gather an appropriate amount of data, the calibration target should extend over a large spatial area with homogeneous backscatter characteristics, hence the term extended area land-targets for calibration. In the following sections, the computation of the outlined parameters is discussed with respect to the selection of applicable calibration targets.

4.4.1 Azimuthal Anisotropy over Land

Over the ocean, measurements of the backscatter coefficient σ^0 observed at multiple azimuth angles are used to infer surface wind speed and direction commonly known as wind vector fields (WVF). The principle of wind direction estimation is based on differences in the backscatter coefficient observed at different azimuth angles, which are caused by sea surface topography induced by surface winds [*Hersbach et al.*, 2007]. Over the land surface, various topographic mechanisms can modulate the recorded backscatter values, resulting in azimuthally anisotropic backscatter [*Bartalis et al.*, 2006]. Particularly in the case of fan-beam scatterometers, it is challenging to discriminate between azimuthally anisotropic backscatter effects and potential inter-beam biases, because measurements at different azimuth angles are acquired by different antennas. Hence, the proposed requirement of a small and well understood dependency of the normalised radar cross section (NRCS) on the azimuth angle is critical for sensor intra-calibration. With regard to the fan-beam configuration of AMI-WS and ASCAT, each location on the Earth's surface is illuminated by each antenna beam at ascending and descending orbit overpass. Thus, a location L on the Earth's surface is observed at discrete azimuth angles determined by the number of fix-mounted antennas (n_{azi}), resulting in a total of six azimuth angles for AMI-WS and twelve angles for ASCAT, respectively. Obviously, a complete description of the backscatter versus azimuthal angle relationship can not be examined by fan-beam sensors in contrast to rotating pencil-beam scatterometers. Nevertheless, the unique arrangement of the Fore- and Aft-beam antennas (see Fig. 3.4) mounted on the European scatterometers ensure the exploration of azimuthal effects modulating backscatter measurements [*Early and Long*, 1997; *Long and Drinkwater*, 2000]. Because of the particular antenna configuration of the Fore- and Aft-beam, observations are acquired at identical incidence angles, enabling the analysis of azimuthal effects displayed in the difference between observations in the two beams given by:

$$\delta_{O,S}(L, t_i) = \sigma^0_{F,O,S}(L, t_i) - \sigma^0_{A,O,S}(L, t_i) \ . \tag{4.2}$$

In equation 4.2, the indices denote that Fore/Aft-beam differences can be calculated separately for each σ^0-triplet i recorded during a specific orbit overpass O by antenna beams within the swath S. An example of Fore/Aft-beam differences over time $\delta_{O,S}(L, t_i)$, of a specific orbit direction and swath at a desert GPI featured by azimuthal anisotropy is illustrated in figure 4.2-a. Fore- and Aft-beam measurements are assumed to be random variables, thus the difference $\delta_{O,S}(L, t_i)$ is expected to be a Gaussian random variable too, which can be represented by the corresponding mean value and standard deviation. The mean value $\delta_{O,S}(L)$ of the calculated differences $\delta_{O,S}(L, t_i)$ is considered to be a measure of azimuthal anisotropy, along with the expectation of a zero mean for land surfaces isotropic in azimuth. Ultimately the magnitude of the azimuthal modulation is of major interest to quantitatively analyse the effect, given by the absolute value of the calculated mean expressed by:

$$\delta_{O,S}(L) = \left| \frac{1}{n} \sum_{i=1}^{n} \delta_{O,S}(L, t_i) \right| \ . \tag{4.3}$$

Applying equation 4.3 to all grid points on the fixed Earth grid, results in estimates of the azimuthal anisotropy observed at a specific orbit direction and swath. Histograms given in figure 4.3 summarises the results of this global analysis for AMI-WS and ASCAT individually. Overall, azimuthal anisotropy estimated for each orbit O and swath S is relatively small, with values ranging from 0. - 0.1 dB evaluated for about 50% of the land surface area. A significant dependency of the azimuthal modulation with respect to different orbit overpasses can not be distinguished. But in terms of the ASCAT dual swath configuration, modulations observed by left swath antennas re-

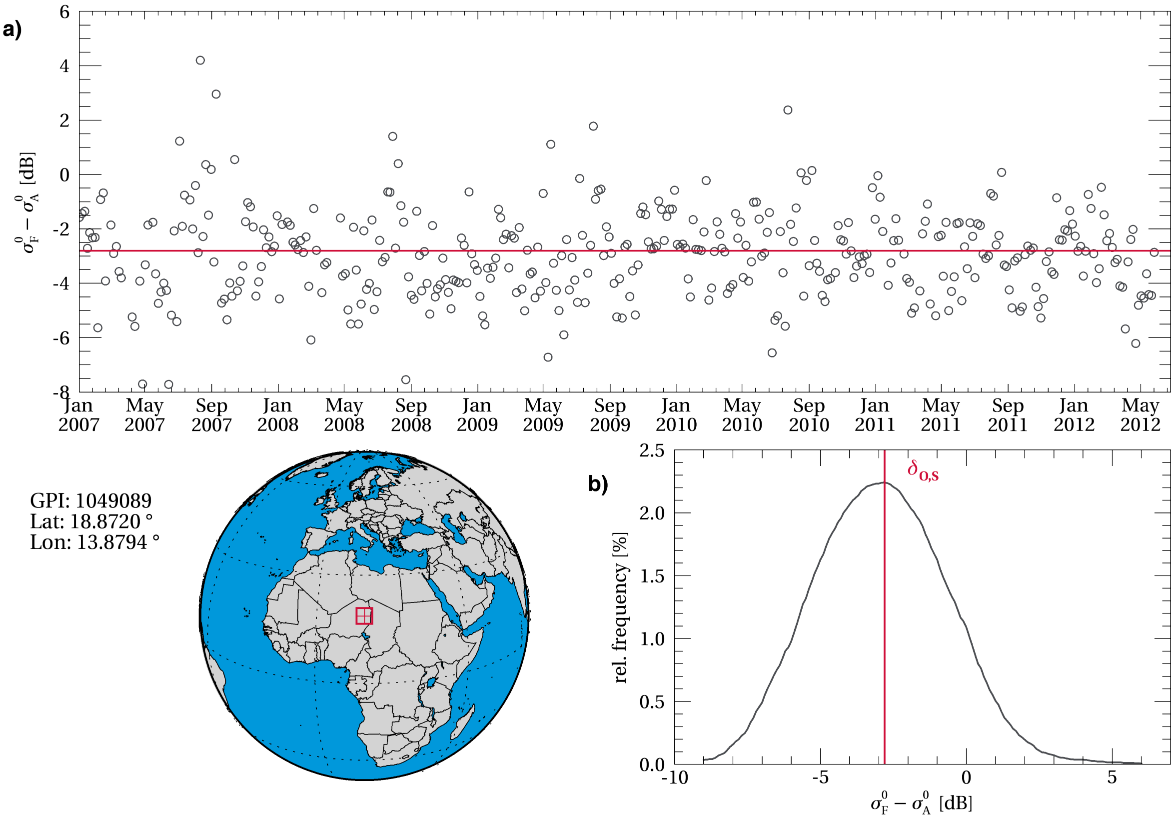

Figure 4.2: Fore- and Aft-beam differences of MetOp-A ASCAT descending orbit, right swath $\sigma^0_F - \sigma^0_A$ at a desert location.
a) $\sigma^0_F - \sigma^0_A$ difference as a function over time
b) relative frequency distribution function of the $\sigma^0_F - \sigma^0_A$ differences

veal slightly higher azimuthal effects than estimations from the right swath. A comparison of the magnitudes of the azimuthal anisotropy between AMI-WS and ASCAT indicates higher azimuthal modulations observed for AMI-WS in a global perspective. Although both relative frequency distributions (see Fig. 4.3) reveal magnitudes of less than 1 decibel of azimuthal anisotropy, a few land surface regions are found with magnitudes of several decibels. With respect to the selection of extended area land-targets for radiometric calibration, an azimuthal anisotropy parameter is required, characterising the overall backscatter dependency with azimuthal angle. Taking this into consideration, the azimuthal anisotropy parameter δ is introduced as the maximum value (see Eq. 4.4) of the individual estimates of $\delta_{O,S}$ for each scatterometer mission. The parameter δ will constitute the major azimuthal anisotropy expected for a target over land, appropriate to identify targets with small azimuthally modulated backscatter measurements.

$$\delta(L) = \max\left(\delta_{O,S}(L)\right) \tag{4.4}$$

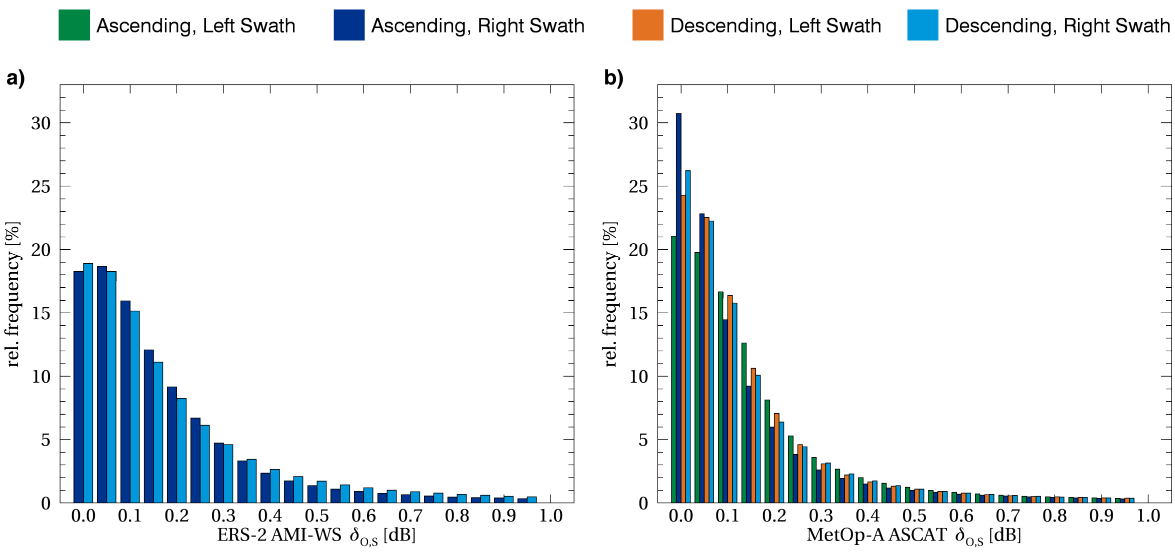

Figure 4.3: Relative frequency distribution of global azimuthal anisotropy estimates for each orbit overpass and swath. a) ERS-2 AMI-WS b) MetOp-A ASCAT

The azimuthal anisotropy parameter δ assessed for ERS-2 AMI-WS and MetOp-A ASCAT is shown in figure 4.4. Missing values of the parameter δ are found for AMI-WS due to performed SAR campaigns (Alaska, Yukon-Territory and Europa) and onboard data storage problems (Central Asia), resulting in restricted scatterometer data coverage for parameter estimation. A visual comparison of the two maps given in figure 4.4 highlight, that azimuthal backscatter modulations persist over time, indicated by equal spatial patterns apparent in both global maps, considering that both sensor cover different temporal periods. The observed spatial patterns differ only in magnitude, as already discussed, with smaller azimuthal anisotropy values δ discovered for ASCAT appearing in brighter colours in figure 4.4-b. For calibration purposes, we are interested in regions with rather small azimuthally modulated backscatter values to facilitate the identity of measurements originating from different antenna beams. Smallest values of the azimuthal anisotropy parameter δ are detected for regions with moderate and dense vegetation cover, mainly induced by volume scattering of the impinging EM wave [*Ulaby et al.*, 1982; *Woodhouse*, 2006]. On the other hand, mountainous regions, cities and some non-mountainous regions with sparse vegetation cover, such as the American prairies, are characterised by δ values up to 1 dB. Areas with extremely high magnitudes of the azimuthal anisotropy parameter δ, greater than 1 dB, are detected particularly in desert regions and on the ice sheet of Greenland. In summary, the azimuthal anisotropy parameter δ is introduced, with the aim to identify land surface regions featured by an isotropic backscatter response in azimuth direction. Investigations of the parameter results in the conclusion that 50% of the land surface exhibit almost isotropic backscatter behaviour ($\leq$ 0.1 dB), with smallest values found for moderate and dense vegetation covered surface regions.

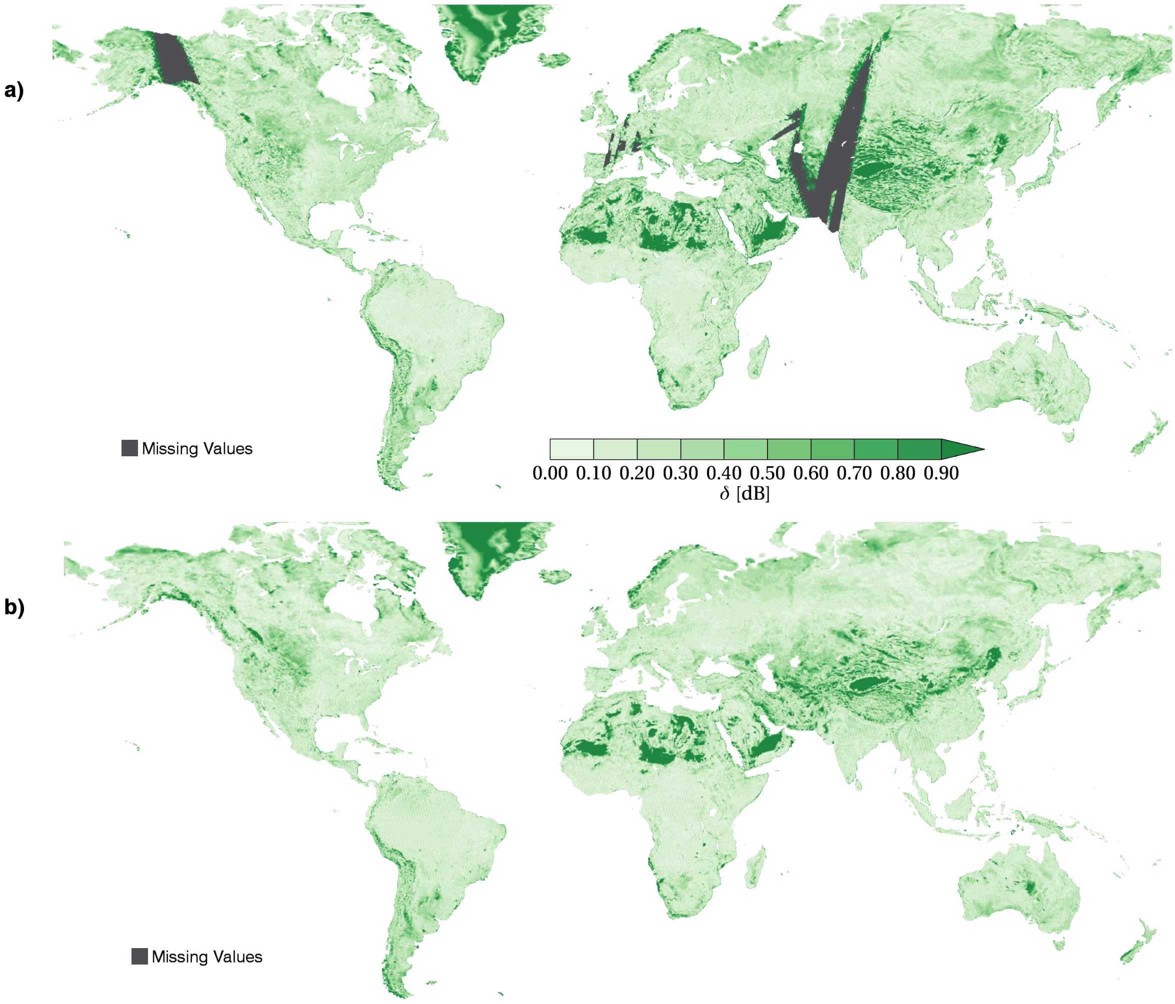

Figure 4.4: Global maps of the azimuthal anisotropy parameter δ, estimated for a) ERS-2 AMI-WS and b) MetOp-A ASCAT

4.4.2 Mean Backscatter and Temporal Variability over Land

Backscatter coefficients of the Earth's land surface are basically controlled by the predominant land cover and geophysical processes. As a consequence, scattering characteristics of land-targets will change over time. However, several studies highlighted that some regions on the Earth's surface exhibit a distinct backscatter response, stable over time at various microwave wavelengths under investigation [*Birrer et al.*, 1982; *Frison and Mougin*, 1996; *Hawkins et al.*, 2000; *Kennett and Li*, 1989a; *Kumar et al.*, 2011]. Natural land-targets with a temporal stable normalised radar cross section (NRCS) are the key requirement for the feasibility of relative calibration of space-borne scatterometers. Targets with a temporal stable backscatter coefficient σ^0 are assumed to be unaffected by time-depended geophysical processes controlling the scattering properties of the target. As stated by *Kennett and Li* [1989b], land-targets suitable for calibration should have a small and well understood backscatter dependency with respect to the time of year or day. Furthermore, target backscatter characteristics are required to remain constant during a mission and if possible also remain constant across several missions. Investigations of the temporal properties of natural land-targets need to account for the measurement configuration of a scatterometer to record backscatter coefficients. In the case of fan-beam scatterometers, the backscatter coefficient σ^0 is mainly a function of the incidence angle θ, with decreasing values of the coefficient with increasing incidence angles. Such measurement configuration effects have to be taken into account, since observations acquired at different times are recorded at varying incidence angles.

Within this study, a linear model (see Eq. 4.5) is chosen to normalise the backscatter coefficient σ^0 with regard to the incidence angle θ to a reference angle of 40 degrees. The model parameters B_0 and B_1 are estimated by an ordinary least-square estimation, depending upon the location L at the Earth's surface and the azimuth configuration ϕ_j, separately for AMI-WS and ASCAT. The azimuth configuration ϕ_j represents the discrimination of each antenna beam per orbit overpass and per swath, to account for possible discrepancies in the target backscatter characteristics. Thus, the incidence angle normalisation model (see Eq. 4.5) displays the mean backscatter versus incidence angle response over time of each antenna beam individually for each azimuth configuration ϕ_j.

$$\sigma^0\left(L,\theta,\phi_j\right) = B_0\left(L,40°,\phi_j\right) + B_1\left(L,40°,\phi_j\right) * \left(\theta - 40°\right) \tag{4.5}$$

The model parameter $B_0\left(L,40°,\phi_j\right)$ denotes the mean backscatter coefficient at 40° incidence angle and the parameter $B_1\left(L,40°,\phi_j\right)$ characterise the mean change ratio of the backscatter coefficient $\sigma^0\left(L,\theta,\phi_j\right)$ with incidence angle, referred to as slope, for a given azimuth acquisition. Incidence angle normalised backscatter values $\sigma^0\left(L,t_i,40°,\phi_j\right)$ are computed by correcting the recorded NRCS values $\sigma^0\left(L,t_i,\theta,\phi_j\right)$ with the derived slope parameter $B_1\left(L,40°,\phi_j\right)$ given by:

$$\sigma^0\left(L,t_i,40°,\phi_j\right) = \sigma^0\left(L,t_i,\theta,\phi_j\right) - B_1\left(L,40°,\phi_j\right) * \left(\theta - 40°\right) . \tag{4.6}$$

Investigations about the temporal variability of the backscatter response concentrate on the long-term variability of land-targets. Long-term variability refers to the variability of measurements related to a mean backscatter value observed across several years. This long-term mean backscatter response $\overline{\sigma^0}\,(L,40°)$ is estimated as the average of the model parameter $B_0\left(L,40°,\phi_j\right)$ over the number of azimuth configurations n_{azi}.

$$\overline{\sigma^0}\left(L,40°\right) = \frac{1}{n_{azi}} \sum_{j=1}^{n_{azi}} B_0\left(L,40°,\phi_j\right) \tag{4.7}$$

It should be noted that the long-term mean backscatter $\overline{\sigma^0}\,(L,40°)$ is only appropriate for land-targets isotropic in azimuth to represent a measurement configuration independent estimate of the true radar cross section of the target (see chapter 4.4.1). In figure 4.5 results of this analysis are illustrated for AMI-WS (see Fig. 4.5-a) and ASCAT (see Fig. 4.5-b). As can be seen, spatial pat-

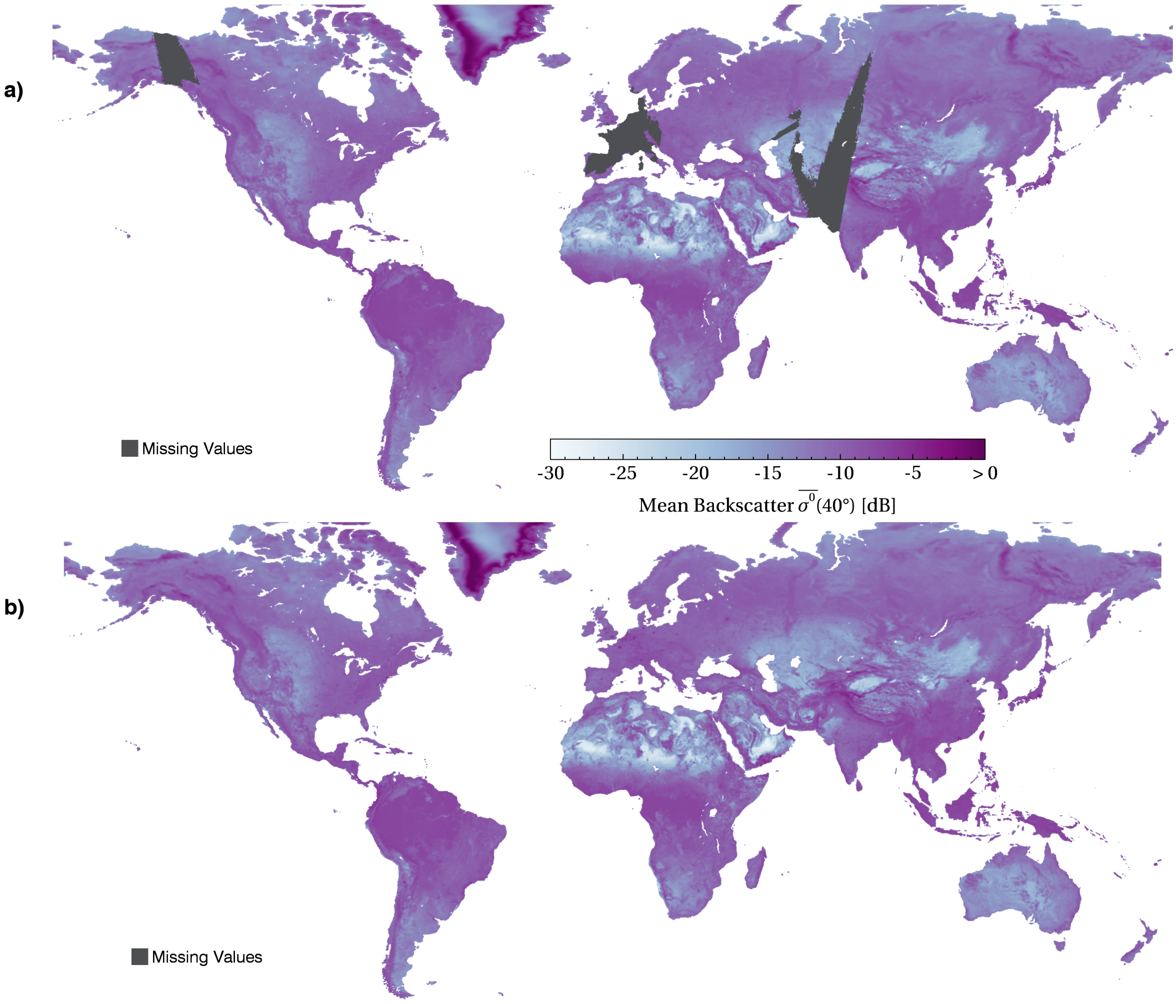

Figure 4.5: Global maps of the estimated long-term mean backscatter coefficient over land $\overline{\sigma^0}(40°)$, estimated for a) ERS-2 AMI-WS and b) MetOp-A ASCAT

terns of the mean backscatter of both scatterometers persist over time, taking into consideration that both datasets cover different time periods. In terms of AMI-WS, missing values are found for some regions on the Earth's surface due to reduced or missing data coverage to perform a robust calculation of the mean backscatter. High mean backscatter values $\overline{\sigma^0}(L, 40°)$, in the range of -10. - 0. dB, are found for vegetated regions, some mountainous areas and over the outer belt of the Greenland ice sheet. In contrast, low values of $\overline{\sigma^0}(L, 40°)$ can be distinguished for sparse vegetated regions, deserts and the center of the Greenland ice sheet. A measure of temporal variability of the backscatter measurements is calculated as the pooled standard deviation of the incidence angle normalised observations $\sigma^0(L, t_i, 40°, \phi_j)$ to account for possible inter-beam biases. Therefore, observations given at location L are assumed to have the same variance but different mean values, because of azimuthal backscatter modulations.

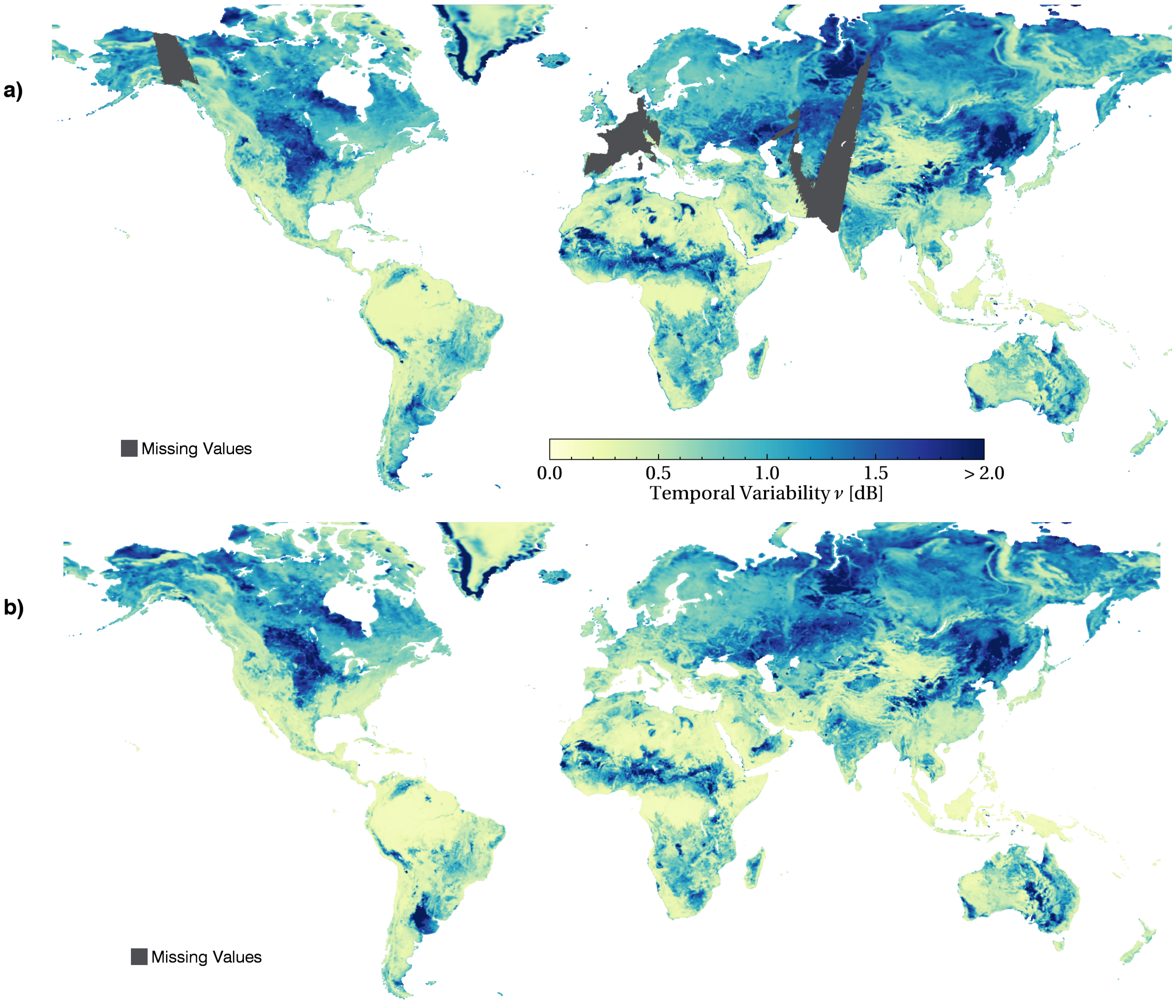

Figure 4.6: Global maps of the temporal variability parameter ν, estimated for a) ERS-2 AMI-WS and b) MetOp-A ASCAT

However, the variance $\nu^2(L, 40°, \phi_j)$ (see Eq. 4.8) of the backscatter observations at a specific azimuth configuration ϕ_j can be estimated with respect to the corresponding mean backscatter at this azimuth acquisition given by the model parameter $B_0(L, 40°, \phi_j)$.

$$\nu^2(L, 40°, \phi_j) = \frac{1}{n} \sum_{i=1}^{n} \left(\sigma_i^0(L, t_i, 40°, \phi_j) - B_0(L, 40°, \phi_j)\right)^2 \tag{4.8}$$

Each individual azimuth acquisition configuration ϕ_j is supposed to be a sample of the backscatter coefficient distribution with an expectancy value equal to the long-term mean backscatter. The estimated standard deviation of this backscatter distribution is considered to be a measure of the temporal backscatter variability, resulting in the temporal variability parameter $\nu(L, 40°)$.

The parameter ν is calculated as the pooled standard deviation specifying the variability of measurements over time expressed by:

$$\nu\left(L,40°\right)=\sqrt{\frac{\sum_{j=1}^{n_{azi}} n_j * \nu^2\left(L,40°,\phi_j\right)}{\sum_{j=1}^{n_{azi}} n_j}} \tag{4.9}$$

Results of the temporal variability analysis are illustrated in figure 4.6 for both European scatterometers. Temporally stable regions with a standard deviation between 0. - 0.3 dB, soft yellow colors in the figures, are identified for land-targets with dense vegetation cover such as the tropical rainforests, and most of the polar and non-polar deserts like the Greenland Arctic desert and the Sahara desert in northern Africa. Moderate to sparse vegetated regions such as croplands and grasslands exhibit highly temporal variable backscatter values and are depicted in blueish colors with an estimated temporal variability $\nu\left(L,40°\right)$ greater than 1 dB.

4.4.3 Selection of Calibration Targets

The selection of extended area land-targets for relative calibration of AMI-WS and ASCAT is based on the backscatter characteristics examined in the previous chapters. The parameters of azimuthal anisotropy δ, long-term mean backscatter $\overline{\sigma^0}\left(L,40°\right)$ and temporal variability $\nu\left(L,40°\right)$ are combined by a simple threshold approach with the objective to derive spatial masks, typifying land-targets for relative calibration of space-borne scatterometers. Figure 4.7 depicts the methodology for the selection of suitable calibration targets, starting at the parameter estimation level (yellow boxes) down to the final calibration target masks. At first, locations identified by an azimuthal anisotropy δ and a temporal variability $\nu\left(L,40°\right)$ parameter less than the defined thresholds are extracted. The defined thresholds (see Tab. 4.2) are chosen to be minimal compared to the global average. As a result, locations identified by backscatter observations almost isotropic in azimuth and stable over time are extracted for further processing.

Parameter	Threshold	
	AMI	ASCAT
Azimuthal Anisotropy	0.3 dB	0.2 dB
Temporal Variability	0.4 dB	
Backscatter Homogeneity	0.25 dB	

Table 4.2: Parameter thresholds used for the selection of calibration targets.

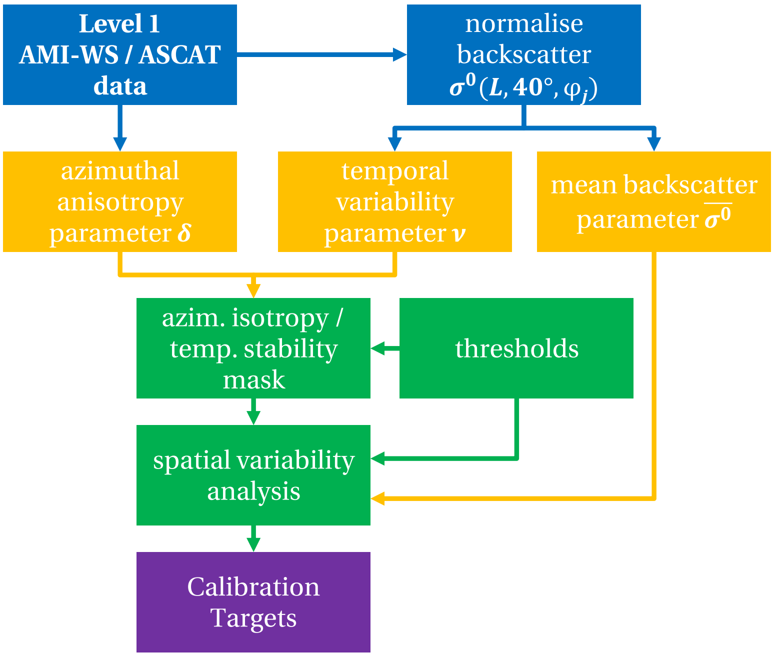

Figure 4.7: Flowchart illustrating the threshold based selection of extended area land-targets for calibration.

To account for the requirement of spatial homogeneous backscatter observations over an extensive area, the spatial variability of backscatter measurements is analysed by evaluating the long-term mean backscatter $\overline{\sigma^0}(L, 40°)$. Therefore, nearby locations extracted from the azimuth isotropy and temporal stability mask are joined to regions representing initial calibration targets. The spatial variability of the mean backscatter $\overline{\sigma^0}(L, 40°)$ within each initial calibration target is analysed by a clustering method referred to as mean-shift clustering. Mean-shift clustering is based on the non-parametric kernel density estimation to assess the probability density function of a n-dimensional feature space [*Cheng*, 1995; *Comaniciu and Meer*, 2002; *Fukunaga and Hostetler*, 1975]. Within this study the feature space is 1-dimensional, composed of the spatially distributed mean backscatter $\overline{\sigma^0}(L, 40°)$ values of a region. The objective is to find the local maxima of the underlying probability density function known as mode, representing the most likely mean backscatter coefficient of a calibration target region. Finally, backscatter spatial homogeneity within a calibration target is achieved by extracting locations L exhibiting a mean backscatter $\overline{\sigma^0}(L, 40°)$ value deviating from the found mode value by the defined homogeneity threshold (see Tab. 4.2). By utilising this selection procedure for AMI-WS and ASCAT, a number of applicable natural targets for relative calibration are found (see Fig. 4.8).

With respect to AMI-WS (see Fig. 4.8-a) seven calibration targets are identified with this selection procedure. All selected calibration targets are covered with dense evergreen vegetation of the tropical rainforests (Amazon, Congo, Southeast Asia). The selection procedure applied to ASCAT

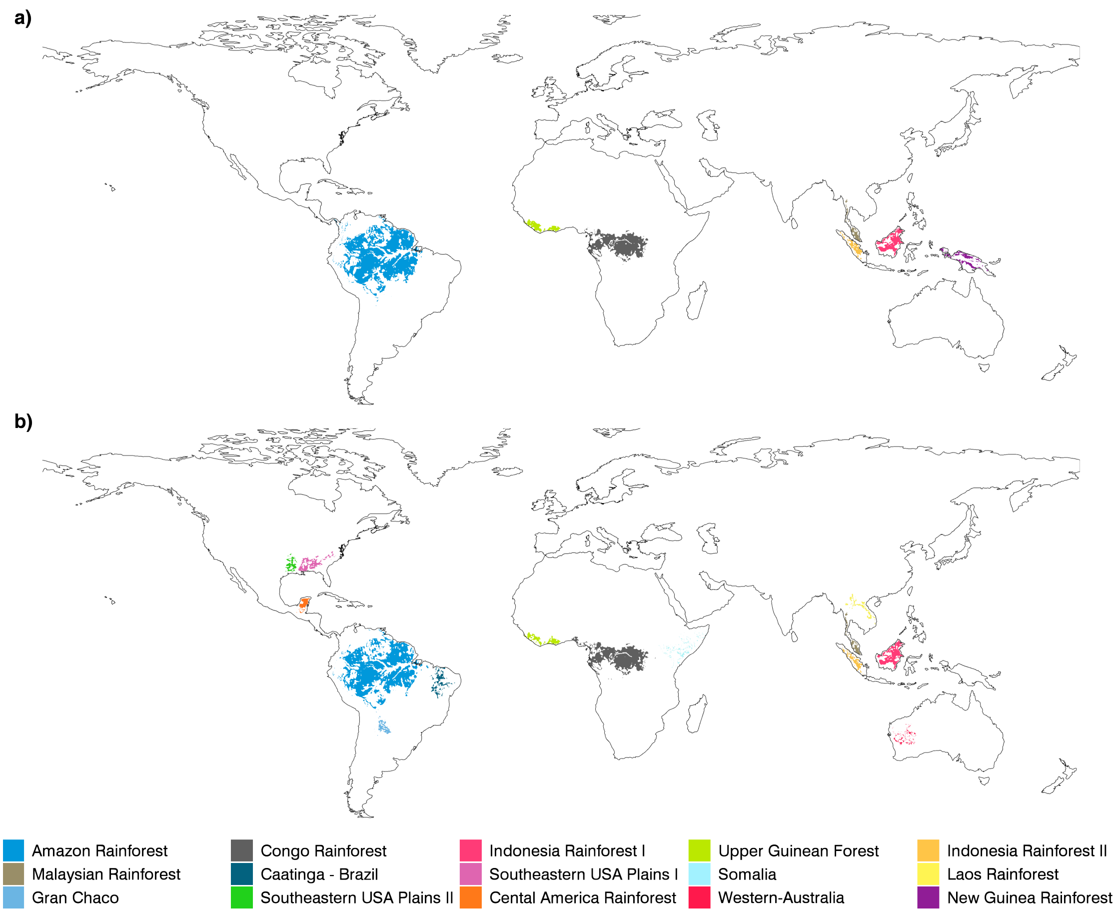

Figure 4.8: Global map of extended area land-targets suitable for calibration a) ERS-2 AMI-WS and b) MetOp-A ASCAT

results in fourteen calibration targets. In addition to targets covered by tropical rainforests, further targets are found in sparsely vegetated regions in Western-Australia and eastern Africa (Somalia) and in temperate forest regions like the South-eastern Plains in North America, Gran Chaco in Northern Argentina and Caatinga in Brazil.

4.5 Sensor Intra-Calibration

During the mission lifetime of a scatterometer in space, numerous disturbances may influence the overall sensor performance and accordingly affect the accuracy of the derived normalised radar cross section σ^0 if disregarded. Space and satellite agencies, such as ESA and EUMETSAT, are routinely monitoring the scatterometer performance in order to correct for such sensor related performance variations. The developed sensor intra-calibration method aims to support already established calibration efforts with the objective to monitor and correct for residual scatterometer performance anomalies. Sensor intra-calibration is performed by utilising natural calibration targets on the Earth's surface, presumed to exhibit a perfectly temporally-stable, spatially-homogeneous and azimuthally isotropic backscatter response over an extended area. With regard to these backscatter properties, a backscatter measurement model (see Eq. 4.11) is introduced for sensor intra-calibration. The proposed measurement model was adopted from *Long and Skouson* [1996] with respect to the measurement geometry of AMI-WS and ASCAT. Backscatter coefficients $\sigma^0\left(L_T, t_i, \theta, \phi_j\right)$ observed for calibration targets L_T are composed of the true normalised radar cross section $\widetilde{\sigma^0}\left(L_T, \theta\right)$ of the calibration target, the intra-calibration coefficient $\widetilde{C_{IAS}}\left(L_T, t_i, \theta, \phi_j\right)$ and sensor noise ϵ.

$$\sigma^0\left(L_T, t_i, \theta, \phi_j\right) = \widetilde{\sigma^0}\left(L_T, \theta\right) + \widetilde{C_{IAS}}\left(L_T, t_i, \theta, \phi_j\right) + \epsilon \tag{4.10}$$

Because of the postulated backscatter characteristics of the calibration targets, the true normalised radar cross section $\widetilde{\sigma^0}\left(L_T, \theta\right)$ of a specific calibration target L_T is exclusively a function of the incidence angle θ. The calibration coefficient $\widetilde{C_{IAS}}\left(L_T, t_i, \theta, \phi_j\right)$ incorporates any arbitrary performance anomaly related to the instrument, accounting for variations in individual antenna characteristics, sensor component degradations or any other anomalies exerting influences on the calibration level of a scatterometer. Hence, in the case of a perfectly calibrated instrument the calibration coefficient becomes equal to null $\left(\widetilde{C_{IAS}}\left(L_T, t_i, \theta, \phi_j\right) = 0\right)$, resulting in observations $\sigma^0\left(L_T, t_i, \theta, \phi_j\right)$ deviating from the true NRCS, $\widetilde{\sigma^0}\left(L_T, \theta\right)$, by the instrument noise ϵ. Furthermore, sensor noise ϵ will be treated as white Gaussian noise with zero mean in the proposed measurement model. Moreover, the true normalised radar cross section $\widetilde{\sigma^0}\left(L_T, \theta\right)$ of a calibration target is unknown, but assuming a perfectly calibrated scatterometer for the time being, an estimate of the unknown normalised radar cross section can be found for each calibration target given that:

$$\overline{\sigma^0}\left(L_T, \theta\right) = \frac{1}{n} \sum_{i=1}^{n} \left(\widetilde{\sigma^0}\left(L_T, \theta\right) + \epsilon\right) = \frac{1}{n * n_{azi}} \sum_{i=1}^{n} \sum_{j=1}^{n_{azi}} \sigma^0\left(L_T, t_i, \theta, \phi_j\right) . \tag{4.11}$$

The estimated backscatter coefficient $\overline{\sigma^0}\left(L_T, \theta\right)$ of a calibration target is presumed to differ from the unknown true normalised radar cross section merely by the absolute accuracy of the instrument. As a consequence, the determined backscatter coefficient $\overline{\sigma^0}\left(L_T, \theta\right)$ will represent a long-term stable calibration reference. By substituting the true backscatter coefficient $\widetilde{\sigma^0}\left(L_T, \theta\right)$ by the estimate $\overline{\sigma^0}(L_T,\theta)$, equation 4.11 can be solved for the calibration coefficient $\widetilde{C_{IAS}}\left(L_T, t_i, \theta, \phi_j\right)$ for each observation $\sigma^0\left(L_T, t_i, \theta, \phi_j\right)$ belonging to a calibration target.

$$\widetilde{C_{IAS}}\left(L_T, t_i, \theta, \phi_j\right) + \epsilon = \sigma^0\left(L_T, t_i, \theta, \phi_j\right) - \overline{\sigma^0}(L_T, \theta) \tag{4.12}$$

As can be seen from equation 4.12, the difference between the observations $\sigma^0\left(L_T, t_i, \theta, \phi_j\right)$ and the estimated calibration reference $\overline{\sigma^0}(L_T,\theta)$ will result in realisations of the calibration coefficient affected by instrument noise ϵ for each individual calibration target L_T. Furthermore, the intra-calibration coefficient, depicting calibration anomalies, is exclusively an attribute of a scatterometer and consequently independent of the calibration target L_T used for determination. Within this study a set of calibration targets will be used for the determination of the intra-calibration coefficient $\widetilde{C_{IAS}}(t,\theta,\phi)$, supposed to result in a more robust prediction of instrument performance anomalies. On account of this, a number of calibration targets n_{TAR} is selected to estimate temporal scatterometer performance anomalies as stated in the following equation 4.13.

$$\overline{C_{IAS}}\left(t_i, \theta, \phi_j\right) = \frac{1}{n_{TAR}} \sum_{T=1}^{n_{TAR}} \left(\widetilde{C_{IAS}}\left(L_T, t_i, \theta, \phi_j\right) + \epsilon\right) \tag{4.13}$$

As a result, the target independent intra-calibration coefficient $\overline{C_{IAS}}\left(t_i, \theta, \phi_j\right)$ can be inferred as the mean value over the number of calibration targets n_{TAR} at time t_i. With respect to intra-calibration of fan-beam scatterometers, calibration coefficients $\overline{C_{IAS}}$ will be deduced separately for each antenna azimuth configuration, denoted by ϕ_j, relative to the define calibration reference $\overline{\sigma^0}$ over time t_i. Finally, the predicted calibration coefficient $\overline{C_{IAS}}\left(t_i, \theta, \phi_j\right)$ is subtracted from the raw backscatter values $\sigma^0\left(L, t_i, \theta, \phi_j\right)$ to correct for residual calibration anomalies. Thus, each observation recorded at a specific location on the Earth's surface L, at time t_i, incidence angle θ and azimuth configuration ϕ_j is corrected with the corresponding estimate of the target independent intra-calibration coefficient $\overline{C_{IAS}}\left(t_i, \theta, \phi_j\right)$ to obtain consistently intra-calibrated scatterometer observations $\sigma^0_{intra}\left(L, t_i, \theta, \phi_j\right)$.

$$\sigma^0_{intra}\left(L, t_i, \theta, \phi_j\right) = \sigma^0\left(L, t_i, \theta, \phi_j\right) - \overline{C_{IAS}}\left(t_i, \theta, \phi_j\right) \tag{4.14}$$

4.6 Sensor Inter-Calibration

Similarities in the instrument technical design of AMI-WS and ASCAT encourage the fusion of these European scatterometer missions towards a long-term consistent backscatter dataset comprising more than 30 years of global data. Possible biases in the observed backscatter coefficient σ^0 of different scatterometer missions have to be taken into account because of potential small differences in the calibration level of each mission. Due to the importance of long-term consistent scatterometer observation, several sensor inter-calibration methods, considering AMI-WS and ASCAT data, were published [*Bartalis*, 2009b; *Elyouncha and Neyt*, 2012, 2013]. *Bartalis* [2009b] examined ERS-2 and MetOp-A scatterometer observation biases by inter-comparison of collocated records over a two year period, from 2007 to 2008, for the common incidence angle range. *Elyouncha and Neyt* [2013], on the other hand, investigated inter-calibration results based on different calibration methods, by examining backscatter measurements recorded during a period of approximately 1 year. In general, sensor inter-calibration methods can be distinguished into model and collocation based inter-calibration. However, in this study a model based sensor inter-calibration method is presented by taking advantage of extended area land-targets. Furthermore, the developed inter-calibration methodology is a stepwise calibration strategy by means of utilising already mission intra-calibrated scatterometer data to infer potential biases between two missions. Therefore, sensor inter-calibration is conducted consecutively to the previously introduced sensor intra-calibration approach. On account of this, temporal calibration anomalies of a specific mission can be neglected, $\widetilde{C_{IAS}}\left(t_i,\theta,\phi_j\right) = 0$, resulting in the assumption of a temporal constant sensor inter-calibration coefficient $\widetilde{C_{IES}}\left(\theta,\phi_j\right)$. Sensor inter-calibration aims to calibrate one sensor, hereafter referred to as slave-sensor, denoted by the index Sla, with respect to a master-scatterometer, denoted by the index Mas. With reference to the introduced measurement model (see Eq. 4.11), the backscatter coefficient $\sigma^0\left(L_T,t_i,\theta,\phi_j\right)$ of a natural calibration target recorded by the master-scatterometer and by the slave-instrument is defined as:

$$\sigma^0\left(L_T,t_i,\theta,\phi_j\right) = \sigma^0_{Mas}\left(L_T,t_i,\theta,\phi_j\right) = \sigma^0_{Sla}\left(L_T,t_i,\theta,\phi_j\right) + \widetilde{C_{IES}}\left(L_T,\theta,\phi_j\right) \,. \tag{4.15}$$

The equation states that observations of the slave-scatterometer $\sigma^0_{Sla}\left(L_T,t_i,\theta,\phi_j\right)$, for a specific calibration target L_T, differ exclusively from backscatter records of the master-scatterometer by the so-called inter-calibration coefficient $\widetilde{C_{IES}}\left(L_T,\theta,\phi_j\right)$. Furthermore, backscatter observations of the master-scatterometer can be substituted by the calibration reference $\overline{\sigma^0_{Mas}}\left(L_T,\theta\right)$ determined for sensor intra-calibration, representing the actual calibration level of the master-sensor. As a result, an explicit model of the inter-calibration problem of two scatterometers can be given by solving equation 4.15 for the desired inter-calibration coefficient.

$$\widetilde{C_{IES}}\left(L_T,\theta,\phi_j\right) + \epsilon = \overline{\sigma^0_{Mas}}\left(L_T,\theta\right) - \sigma^0_{Sla}\left(L_T,t_i,\theta,\phi_j\right) \tag{4.16}$$

Estimates of the inter-sensor calibration coefficient $\widetilde{C_{IES}}\left(L_T,\theta,\phi_j\right)$, accompanied by instrument noise ϵ, can be determined by subtracting backscatter observations of the slave-scatterometer from the defined calibration level $\overline{\sigma^0_{Mas}}(L_T,\theta)$ of the master-sensor. Moreover, the predicted sensor inter-calibration coefficient is exclusively a sensor related property and therefore independent of the investigated calibration target. Equivalently to the discussed intra-calibration methodology, it is supposed that exploiting a number of calibration targets n_{TAR} for the determination of the inter-calibration coefficient $\widetilde{C_{IES}}\left(\theta,\phi_j\right)$ will result in a more robust prediction. Thus, estimates of a set of calibration targets are used to infer a possible inter-calibration bias $\overline{C_{IES}}\left(\theta,\phi_j\right)$ between the master- and the slave-scatterometer defined as:

$$\overline{C_{IES}}\left(\theta,\phi_j\right) = \frac{1}{n_{TAR}}\sum_{T=1}^{n_{TAR}}\widetilde{C_{IES}}\left(L_T,\theta,\phi_j\right)+\epsilon \tag{4.17}$$

The temporal constant inter-calibration coefficient $\overline{C_{IES}}\left(\theta,\phi_j\right)$ is inferred as the mean value of realisations over the number of utilised calibration targets n_{TAR}. Sensor inter-calibrated backscatter observations $\sigma^0_{inter}\left(L,t_i,\theta,\phi_j\right)$ can be derived by correcting observations of the defined slave-scatterometer with the derived inter-calibration coefficient as stated by equation 4.18. As a result, the defined calibration references $\overline{\sigma^0_{Mas}}(L_T,\theta)$ and $\overline{\sigma^0_{Sla}}(L_T,\theta)$ are supposed to be aligned, paving the way towards a consistent long-term scatterometer data archive.

$$\sigma^0_{inter}\left(L,t_i,\theta,\phi_j\right) = \sigma^0_{Mas}\left(L,t_i,\theta,\phi_j\right) = \sigma^0_{Sla}\left(L,t_i,\theta,\phi_j\right) - \overline{C_{IES}}\left(\theta,\phi_j\right)\ . \tag{4.18}$$

Chapter 5

Calibration of AMI-WS and ASCAT

5.1 Overview of the Chapter

A relative calibration methodology for C-band fan-beam scatterometers was introduced in the precedent chapter 4. In the following sections of this chapter, the developed calibration methodology is employed to the European scatterometers AMI-WS and ASCAT, with the objective to obtain a long-term consistent scatterometer data archive for climate change research. As already discussed, the calibration procedure relies on the use of extended area land-targets with well defined backscatter characteristics. Applicable calibration targets were determined based on a threshold decision scheme applied to each grid point GPI (see chapter 4.4) of the Earth fixed grid, but a comprehensive characterisation of the backscatter attributes of each extended area land-target is desirable. Hence, various backscatter characteristics are investigated to prove the capability of the selected extended area land-targets for calibration purposes. Moreover, a subset of calibration targets is extracted with regard to defined quality criteria, quantifying the applicability of a target for the proposed calibration methodology. Based on the selected calibration target subset, sensor intra-calibration of AMI-WS and ASCAT is performed, in order to achieve consistent calibration throughout each individual European scatterometer mission. In this respect, the ascertainment of a backscatter model, representing the backscatter calibration reference of a target, and the assessment of intra-sensor calibration coefficients is discussed in detail. Furthermore, the estimated intra-calibration coefficients are applied to the corresponding scatterometer sensor and the resulting data archive is verified with regard to the desired mission consistency. The chapter is completed by a discussion about sensor inter-calibration of AMI-WS and ASCAT, in terms of highlighting observed differences between these scatterometer missions and the determination of sensor inter-calibration coefficients. The derived inter-calibration coefficients are applied to correct for the observed differences between AMI-WS and ASCAT, followed by a verification of the resulting long-term scatterometer dataset.

5.2 Introduction

After the launch of AMI-WS or ASCAT, the commissioning phase of the satellite instrument is initiated. During the instrument commissioning phase, in-flight calibration campaigns were carried out to establish the initial calibration level of the European scatterometers AMI-WS and ASCAT by the use of active transponders [*Fromberg et al.*, 2010; *Lecomte and Wagner*, 1998]. Once in operation, the sensor performance is monitored by means of routinely performed calibration campaigns to account for potential instrument related drifts. Subsequently, the scatterometer ground processor is updated to the latest calibration level to meet the required instrument accuracy for the provided backscatter observations. The updated calibration level is kept constant between two consecutive calibration campaigns, disregarding potential instrument drifts in between, controlling the overall instrument accuracy. Therefore, scatterometer data may be considered to be composed of different calibration levels and unaccounted short-term drifts, as long as no complete re-processing of the entire data archive was carried out with reference to a unique calibration level.

Especially for the creation of higher level scatterometer products, like surface soil moisture (SSM) [*Wagner et al.*, 1999a] or wind vector fields (WVF) [*Stoffelen*, 1998], scatterometer data made up of different calibration levels and potential short-term drifts are critical. So-called Level 2 scatterometer products rely on pre-estimated model parameters, which, in terms of SSM retrieval, are determined by multi-annual analysis of the normalised radar cross section σ^0. As a consequence, various calibration levels and drifts within scatterometer data will degrade the model parameter estimation accuracy and accordingly decrease the prediction accuracy of the quantity of interest. As can be imagined, the correction of calibration related variations within a scatterometer dataset is of major importance. The proposed sensor intra-calibration methodology, see chapter 4.5, was developed to correct for calibration related instrument variations throughout a scatterometer mission in a relative fashion, resulting in consistent calibrated backscatter measurements. Sensor intra-calibration aims to detect and correct for backscatter drifts distinguished in specific antenna beams of a scatterometer, relative to a defined calibration reference to ensure instrument stability.

A long-term consistent scatterometer data record is envisaged in view of climate change research and in terms of the creation of a surface soil moisture ECV derived from European scatterometers. Hence, backscatter observations of different missions need to be fused to a multi-mission data archive, by accounting for possible discrepancies between various scatterometer missions. The proposed sensor inter-calibration methodology, see chapter 4.6, is applicable to identify and correct for differences between two scatterometer missions, attaining the desired long-term data record. It is worthwhile to state that the proposed calibration methodology is a stepwise calibration process. As a result, the presented sensor inter-calibration method is exclusively applicable to already intra-calibrated scatterometer sensors, due to the assumption of a temporal invariant backscatter relationship between two instruments.

Both calibration methods rely on the use of extended area land-targets with unique scattering characteristics. With respect to the presented calibration methodology, each extended area calibration target is supposed to act as a particular calibration reference, although it is comprised of various independent smaller scale targets. Hence, heterogeneities in the backscattering features exhibited by the independent targets will cause inaccuracies in the calibration parameter predication. Accordingly, special attention have to be paid to spatial and temporal variations within each calibration target to guarantee the reliability of the presented calibration methodology.

5.3 Backscatter Characteristics of Calibration Targets

The selection of extended area land-targets applicable for the calibration of C-band scatterometers was discussed in chapter 4.4, resulting in seven suitable calibration targets for AMI-WS and fourteen targets for ASCAT respectively. Calibration targets were selected based on a simple threshold decision scheme (see Fig. 4.7) employed for each Grid Point Index (GPI) on the Discrete Global Grid (DGG). As a result, calibration targets consists of a number of individual GPIs, which in terms of scatterometer calibration are considered equally. Therefore, a comprehensive characterisation of the backscatter properties of each individual extended area calibration target was not possible during the selection process. As a consequence, the defined target requirements for calibration (see chapter 4.4) of each individual calibration target needs to be proven to confirm the applicability of the targets for calibration purposes. Analysis are carried out concentrating on the backscatter versus azimuth angle relationship, the backscatter dependency with incidence angle and spatio-temporal variations of the observed backscatter coefficient within a calibration target. Taking into account the results of this analysis, the selected calibration targets will be classified in accordance to their quality of fulfilling the defined target requirements for calibration.

5.3.1 Azimuthal Anisotropy of Calibration Targets

The backscatter versus azimuth angle relationship was investigated in chapter 4.4.1 by introducing the azimuthal anisotropy parameter $\delta(L)$, to identify targets on the Earth's surface featured by a small dependency of the backscatter σ^0 with azimuth angle ϕ. Extended area land-targets characterised by a small backscatter dependency in azimuth direction are essential to discriminate potential inter-beam biases in the introduced sensor intra-calibration methodology. Hence, the requirement of small backscatter modulations with respect to the azimuth angle need to be

	$\delta(L_T)$ [dB]	
	AMI-WS	ASCAT
Amazon Rainforest	0.11	0.10
Congo Rainforest	0.13	0.12
Indonesia Rainforest I	0.12	0.09
Upper Guinean Forest	0.13	0.10
Indonesia Rainforest II	0.13	0.10
Malaysian Rainforest	0.13	0.09
Caatinga - Brazil	-	0.12
Southeastern USA Plains I	-	0.17
Somalia	-	0.16
Laos Rainforest	-	0.10
Gran Chaco	-	0.18
Southeastern USA Plains II	-	0.15
Cental America Rainforest	-	0.11
Western-Australia	-	0.15
New Guinea Rainforest	0.11	-

Table 5.1: Estimated azimuthal anisotropy parameter $\delta(L_T)$ of targets selected for AMI-WS and ASCAT calibration.

proven for each selected calibration target individually. Accordingly, the azimuthal anisotropy parameter introduced in chapter 4.4.1 was adopted to quantify azimuthal modulation effects by substituting the location argument L to represent an entire calibration target L_T, resulting in $\delta(L_T)$. Table 5.1 summarises the findings of this azimuthal anisotropy analysis, indicating that almost each calibration target exhibits only half of the magnitude of the pre-defined azimuthal anisotropy threshold (see table 4.2). In terms of AMI-WS, the smallest value of the parameter $\delta(L_T)$ is found for Amazon Rainforest and New Guinea Rainforest, with an observed azimuthal anisotropy of 0.11 dB. Values of the azimuthal anisotropy parameter $\delta(L_T)$ calculated for ASCAT are in general smaller than those computed for AMI-WS, with respect to coincident calibration targets. Especially the Malaysian Rainforest and the Indonesian Rainforest I are featured by low azimuthally anisotropic backscatter modulations with a magnitude of 0.09 dB. So far, backscatter azimuthal anisotropy was considered to be a time invariant target property, however this assumption have to be verified carefully. Examination of the temporal evolution of the azimuthal anisotropy parameter closely follows the derivation of δ, equations 4.2 to 4.4, which easily can be extended by the function argument t_i representing the time of determination, resulting in the following given equation.

$$\delta\left(L_T, t_i\right) = \max\left(\delta_{O,S}\left(L_T, t_i\right)\right) \tag{5.1}$$

The temporal evolution of the azimuthal anisotropy $\delta(L_T, t_i)$ will be explored by utilising equation 5.1 for each calibration target. Figure 5.1 illustrates the results of this temporal analysis of the azimuthal anisotropy $\delta(L_T, t_i)$, based on monthly estimates individually for AMI-WS and ASCAT. Temporal variations of the parameter $\delta(L_T, t_i)$ found for AMI-WS (see Fig. 5.1-a) show a rapid increase of the assessed anisotropy after May 2001 consistently for all calibration targets. This anomaly correspond to the failure of the Attitude and Orbit Control System (AOCS) on January 2001, causing ESA to pilot ERS-2 in the so called Zero Gyro Mode (ZGM). In addition, this temporal anomaly after May 2001 could explain the observed differences in the time invariant estimates of the azimuthal parameter $\delta(L_T)$ of AMI-WS calibration targets, see table 5.1, with respect to ASCAT. On the other hand, a seasonal cycle of the parameter $\delta(L_T, t_i)$ can be distinguished for most of the targets selected for ASCAT calibration. Amplitudes of the seasonality and additionally the signal-phase varies from target to target, concluding that the observed seasonality of the parameter $\delta(L_T, t_i)$ is not related to sensor malfunctions but rather a property of each individual calibration target. An explanation of the less distinctive seasonality in the parameter estimates of AMI-WS can be found in the Level 1 calibration approach of the sensor. In the ERS scatterometer era, a relative calibration approach was routinely performed based on the γ^0-model. As already outlined in chapter 3.8, the assumption of this calibration method is a temporal and spatial stable isotropic backscatter behaviour of Amazon Rainforest. Under this assumption the deduced γ^0 backscatter coefficients (see Eq. 3.22) are calibrated to a mean γ^0 backscatter response of the Rainforest. As a consequence of this calibration approach, any temporal azimuthal backscatter deviations exhibited by Amazon Rainforest are considered to be sensor related and therefore corrected for [*Lecomte and Wagner*, 1998]. Although the seasonal behaviour of the azimuthal anisotropy parameter $\delta(L_T, t_i)$ is diverse for coincident calibration targets of AMI-WS and ASCAT, it is worthwhile to note that the average magnitude of the parameter $\delta(L_T, t_i)$ is stable across both scatterometer missions. In summary, the observed azimuthal anisotropy $\delta(L_T, t_i)$ of AMI-WS and ASCAT for coincident calibration targets is ranging from 0.06 dB to less than 0.1 dB, neglecting the detected seasonality and parameter estimates of AMI-WS after May 2001. For that reason, selected calibration targets of AMI-WS and ASCAT are perceived as isotropic targets with regard to the calibration methodology of C-band scatterometers presented within this work.

5.3.2 Backscatter Incidence Angle Dependency

The normalised radar cross section σ^0 of an arbitrary target on the Earth's surface is strongly dependent on the incidence angle θ at which the observation was recorded. In general, the dependency of the backscatter coefficient σ^0, with respect to the incidence angle θ, is controlled by various variables. Earth's surface parameters such as land cover, moisture content and surface roughness as well as technical parameters of a RADAR system such as the operating frequency and polarisation are regulating this dependency. As already outlined in chapter 4.4.3, backscatter

Figure 5.1: Temporal evolution of the azimuthal anisotropy parameter $\delta(L_T, t_i)$ determined for the selected calibration targets. Column a) results found for ERS-2 AMI-WS and column b) results found for MetOp-A ASCAT

measurements have to be normalised to a reference incidence angle in order to analyse temporal and spatial variations of the σ^0-coefficient. In the selection scheme of extended area land-targets for calibration, a 1-order polynomial (see Eq. 4.5) was chosen for simplicity to normalise each backscatter observation to a reference incidence angle of 40 degrees. Furthermore, an accurate description of the backscatter behaviour with respect to the incidence angle is vital for the success of the proposed calibration methodology, outlined in chapter 4.5 and 4.6, because the determined calibration reference of individual calibration targets is postulated to be a function of incidence angle exclusively. In this section, the backscatter incidence angle dependency of the selected targets will be analysed in detail, with the objective to identify a simple parametrised and accurate backscatter model, valid for the complete range of calibration targets of AMI-WS and ASCAT. It is assumed that the dependency of the backscatter coefficient σ^0 with respect to the incidence angle θ can be modelled as a continuous function with decreasing σ^0 coefficients by increasing incidence angles θ. Backscatter incidence angle models considered in this work are simple empirical models, n-order polynomial functions centred at 40 degrees incidence angle (see Eq. 5.2), which have a straightforward parametrisation. In addition, the already known γ^0-model (see Eq. 3.22) is examined in terms of representing the backscatter versus incidence angle dependency of the selected calibration targets accurately for both C-band scatterometers.

$$\sigma^0(\theta) = B_0\left(40°\right) + \sum_{p=1}^{n_{poly}} B_p * \left(\theta - 40°\right)^p \tag{5.2}$$

Two data density plots are illustrated in figure 5.2 to gain a first understanding of the general behaviour of the backscatter coefficient σ^0 as function of the incidence angle θ. Data recorded by AMI-WS in July 1998 over Amazon Rainforest were selected to compute the density plot and observations recorded in July 2008 were considered for ASCAT respectively. A distinction between various beams, Fore-/ Mid-/ Aft-Beam, and different satellite overpasses, ascending/descending overpass, was neglected for data selection, due to the already proven azimuthal isotropic backscatter characteristics of the calibration targets (see chapter 5.3.1). Additionally, a series of backscatter models are plotted in figure 5.2, modelled by polynomials up to the order of five and the γ^0-model, evaluated by the use of the underlying data. A visual comparison of these models suggests that polynomials of order two to five reveal almost identical behaviour and fit the underlying data accurately. The 1-order polynomial model displays the approximated trend of the coefficient σ^0, but can not rigorously model the overall backscatter behaviour (under-fitting). A good analogy was found for observations of AMI-WS over Amazon Rainforest (see Fig. 5.2-a) and the γ^0-model, but in terms of ASCAT (see Fig. 5.2-b) the model failed to predict the backscatter behaviour, especially for incidence angles greater than 50 degrees and less than 30 degrees. The main reason of the γ^0-model prediction failure with respect to ASCAT data is that the γ^0-model was devised particularly for AMI-WS relative calibration over Amazon Rainforest, regarding the rainforest as pure volume scatterer for the entire range of incidence angles of the sensor [*Crapolicchio*, 2004; *Lecomte and Wagner*, 1998]. However, in this work natural extended area land-targets of different land cover types are used to infer calibration quantities. In order to select a particular "best-fit" backscatter incidence angle model, appropriate for all calibration targets of AMI-WS and ASCAT, a more quantitative evaluation approach is needed. This approach is based on model selection methods taking into account the Akaike's information criterion (AIC), model cross-validation and regression analysis [*Burnham and Anderson*, 2002; *Hastie et al.*, 2003]. These methods provide independent and also slightly different quantitative information about the quality of a model to fit a certain dataset. Candidate models evaluated with this selection methods are polynomial functions of order one, up to the order of ten (see Eq. 5.2) and supplementary the γ^0-model for benchmarking. The Akaike's information criterion (AIC) or more precisely the AIC differences (ΔAIC) provide a relative quality measure for a set of candidate models to represent the underlying data samples, accounting for the goodness of fit and the model complexity. Taking for granted that errors of the complete set of candidate models are normally distributed, the AIC

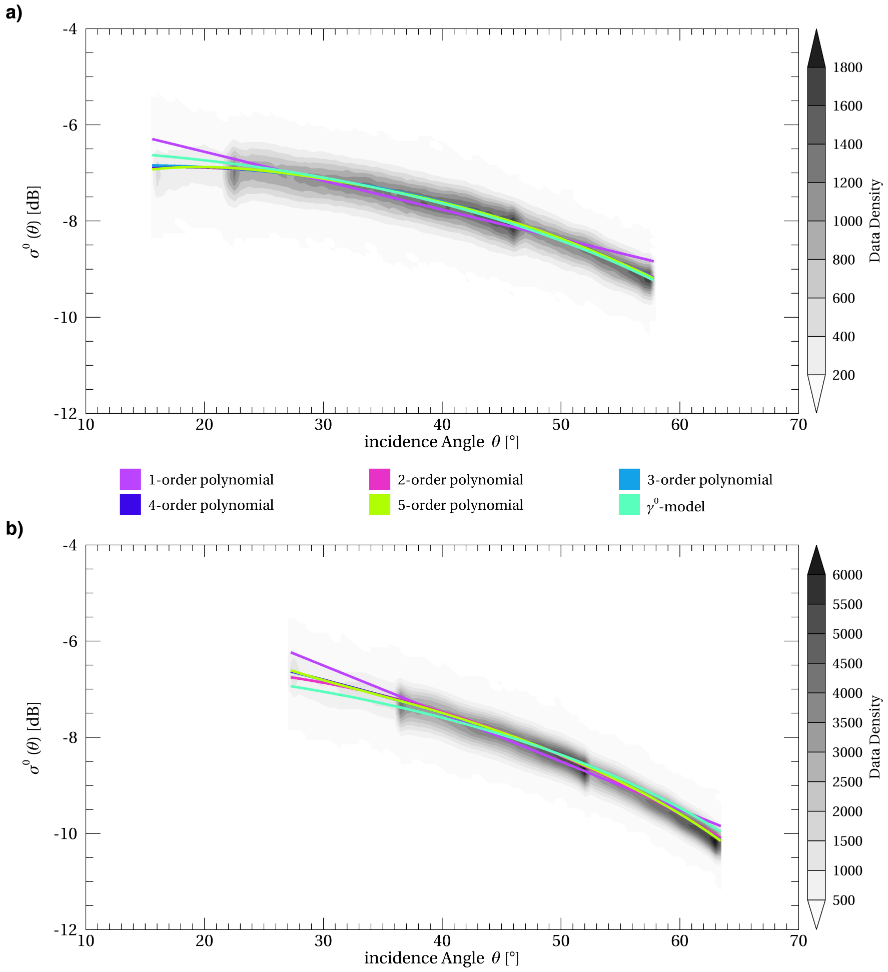

Figure 5.2: Data density plots with a set of estimated backscatter incidence angle models for Amazon Rainforest. a) ERS-2 AMI-WS data recorded in July 1998 and b) MetOp-A ASCAT data observed in July 2008

can be computed from least square regression statistics [*Burnham and Anderson*, 2002] given by:

$$AIC = 2K + n \log \sigma^2 \,. \tag{5.3}$$

In equation 5.3 the variable K denotes the number of independent parameters in a model referred to as model complexity, n designates the data sample size and σ^2 indicates the estimated mean squared error (see Eq. 5.5) of the data with respect to the model. An individual AIC value by itself is not interpretable, but differences (see Eq. 5.4) between AIC values of candidate models offers a relative measure of how much information is lost when a given model is used. AIC differences (ΔAIC) are routinely computed with reference to the minimum AIC value found for a candidate set of models.

$$\Delta AIC = AIC - AIC_{min} \tag{5.4}$$

Complementary to the ΔAIC measure, a random sub-sampling cross-validation of the candidate models was carried out to estimate the performance of each model in practice. The objective of the random sub-sampling cross-validation is to randomly partition a given dataset into a training- and validation-dataset. Candidate models are fitted to the trainings-dataset and subsequently the predicted model accuracy is assessed on the validation dataset by employing a measure of fit like the mean squared error (MSE), see equation 5.5. The validation dataset is regarded as independent dataset and accordingly the MSE of the validation dataset give an estimate of the generalised error of the model applied to any independent data. Commonly the MSE is utilised to express the quality of a model to fit the underlying data, defined as the mean of the squared residuals $\left(\epsilon_i^2\right)$ estimated between the model values (Y_i) and data $\left(y_i\right)$.

$$MSE = \frac{1}{n}\sum_{i=1}^{n}\epsilon_i^2 = \frac{1}{n}\sum_{i=1}^{n}\left(y_i - Y_i\right)^2 \tag{5.5}$$

A further meaningful measure to quantify models to represent a certain dataset is referred to as coefficient of determination $\left(R^2\right)$. The coefficient of determination $\left(R^2\right)$ can be interpreted as the proportion of variation of the data that is described or accounted for by the model [*Wilks*, 2011]. The coefficient is computed from

$$R^2 = 1 - \frac{SSE}{SST} = 1 - \frac{\sum_{i=1}^{n}\left(y_i - Y_i\right)^2}{\sum_{i=1}^{n}\left(y_i - \overline{y_i}\right)^2}\,, \tag{5.6}$$

relating the residual sum of squares (SSE), which is proportional to the mean squared error (see Eq. 5.5), and the so called total sum of squares (SST), which is proportional to the sample variance. If the model perfectly fits the data, the residual sum of squares (SSE) gets equal to null, resulting in $R^2 = 1$. The outlined model selection methods were employed for each selected calibration target of AMI-WS and ASCAT separately. Furthermore, the set of candidate models were evaluated for each month of the year in consideration of temporal discrepancies in the model selection. An example of computed model selection results is depicted in figure 5.3 with respect to the ASCAT calibration target Congo Rainforest. AIC differences (ΔAIC) of the investigated candidate models, polynomial function up to the order of ten, were normalised with respect to the maximum found ΔAIC value. Figure 5.3-a indicates that candidate models with polynomial orders greater than three tend to over-fitting and do not significantly improve the quality of the model to fit the underlying data. Moreover, the inter-annual monthly estimated AIC differences of the candidate models state the temporal invariance the models with an overall best fit model found for polynomial order of three. Model selection results of the γ^0-model (dashed line) are added to figure 5.3 to have a performance benchmark of the polynomial models. The benchmark was chosen with respect to the month of the minimum determined mean squared error of the γ^0-model. Cross-validation analysis of the candidate models (see Fig. 5.3-b) endorse the results found for the Akaike's information criterion (AIC), but the estimated cross-validation MSE

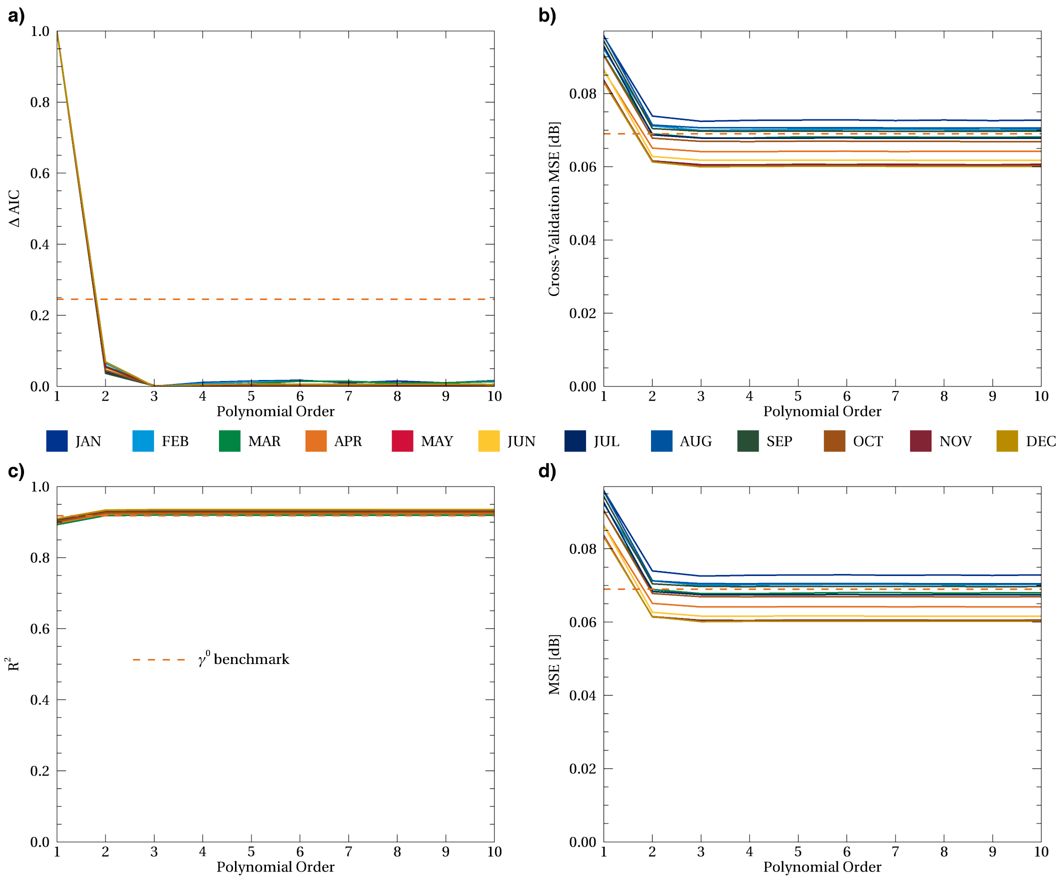

Figure 5.3: Results of the backscatter incidence angle model selection methods with respect to the Congo Rainforest calibration target based on ASCAT data. Model selection methods were utilised for each month of the year separately, illustrated by different line-colors. a) Δ AIC b) mean squared error (MSE) of cross-validation c) coefficient of determination R^2 d) total mean square error

indicates monthly variations of the sample variance. Data acquired in May, October or November seems to exhibit less variability, average MSE of approximately 0.06 dB, than data recorded in January, February or August with an average MSE of 0.075 dB. Furthermore, the cross-validation MSE and complementary the total model mean squared error (see Fig. 5.3-d) expose that polynomial models of orders greater than two do not considerably decrease the mean squared error. A similar statement can be drawn from the analysis of the coefficient of determination R^2, pointing out that more than 90% of the variability in the data is captured by polynomial models of order greater than one. Additionally, the coefficient of determination remain constant by increasing the polynomial order, concluding that no additional information about the backscatter versus incidence angle dependency will be attained. In general, calculated model selection variables of the candidate polynomials, with an order greater than one, achieve better scores than the independent γ^0-model used for benchmarking as can be spotted in figure 5.3. As a consequence, the analysed candidate models will predict the backscatter incidence angle dependency more accurately than the γ^0-model. At an overall perspective of this model selection analysis for AMI-WS and ASCAT calibration targets, the results discussed on the example of Congo Rainforest are equivalent for all calibration targets with exceptions concerning sparsely vegetated targets (Somalia and Western-Australia) and the Southeastern USA Plains calibration targets of ASCAT. The Somalia calibration target clearly indicates that a linear model (1-order polynomial) represents the "best-fit" backscatter incidence angle model. Polynomials of higher order obviously over-fits the backscatter versus incidence angle behaviour and decreases the prediction accuracy. Investigations concentrating on AIC differences of the Western-Australia target suggest a 3-order polynomial to accurately predict the backscatter dependency on incidence angle, but the outcome of the cross-validation, R^2 and the total MSE analysis show that polynomial functions of order one to five are appropriate models too. Nevertheless, sparsely vegetated calibration targets of ASCAT exhibit a significantly higher mean squared error, 0.3 dB - 0.6 dB, at some months of the year than that observed for Rainforest targets. On the other hand, calibration targets located in the Souteastern USA Plains expose fairly constant values for all model selection methods across all investigate candidate models. Summing up, an appropriate model to characterise the backscatter incidence angle dependency is found with a 2-order polynomial with reference to the estimated model selection parameters, Δ AIC, the cross-validation MSE, R^2 and the overall mean square error of the model. The 2-order polynomial function satisfies the required model selection criteria and serves as a good compromise between densely and sparsely vegetation covered calibration targets for AMI-WS and ASCAT.

5.3.3 Spatial and Temporal Backscatter Variations

With reference to the selection criteria of land-targets for the calibration of space-borne scatterometers, a long-term stable and spatial homogeneous backscatter response of the targets is indispensable over an extended area. As a consequence, temporal and spatial variations of the backscatter were taken into account in the threshold based calibration target selection scheme (see chapter 4.4). The objective of the this chapter is to confirm the required temporal backscatter stability and to verify the spatial homogeneous backscatter response of the calibration targets. Analysis of spatial and temporal backscatter variations were carried out under consideration of the discovered findings discussed in chapter 5.3.1 and 5.3.2. Accordingly, it is presumed that each calibration target acts like a perfect isotropic scatterer with respect to the azimuth angle ϕ and that the backscatter dependency with incidence angle can be accurately modelled by a 2-order polynomial centred at 40° incidence angle (see Eq. 5.7). Backscatter incidence angle model coefficients (B_0, B_1 and B_2) were estimated for each month of the year (t_M), representing the inter-annual monthly mean backscatter versus incidence angle behaviour of each calibration target L_T.

$$\sigma^0\left(L_T, t_M, \theta\right) = B_0\left(L_T, t_M, 40^\circ\right) + \sum_{p=1}^{n_{poly}=2} B_p\left(L_T, t_M, 40^\circ\right) * \left(\theta - 40^\circ\right)^p \tag{5.7}$$

Due to the assumption of a perfect isotropic scatterer with respect to the azimuth angle ϕ_j, backscatter observations from different antenna beams are considered equally for the model parameter estimation. Furthermore, the derived model coefficients were applied to each observation recorded in the corresponding month, to normalise the backscatter $\sigma^0(L_T, t_i, \theta)$ within a calibration target L_T to a reference incidence angle of 40 degrees.

$$\sigma^0\left(L_T, t_i, 40°\right) = \sigma^0\left(L_T, t_i, \theta\right) - B_1\left(L_T, MOY(t_i), 40°\right) * \left(\theta - 40°\right) - B_2\left(L_T, MOY(t_i), 40°\right) * \left(\theta - 40°\right)^2 \tag{5.8}$$

As a result, backscatter observations $\sigma^0(L_T, t_i, 40°)$ of a specific calibration target can be compared in space and time, regardless to the measurement geometry of the observations.

5.3.3.1 Spatial Backscatter Variability

In order to examine spatial variations of the NRCS within a calibration target, deviations between the mean backscatter of a specific GPI and the mean backscatter response of the entire target were investigated. The mean backscatter response of a specific GPI, $\overline{\sigma^0}(L, 40°)$, within a calibration target is calculated as the average backscatter value at 40 degrees incidence angle over time (see Eq. 5.9).

$$\overline{\sigma^0}\left(L, 40°\right) = \frac{1}{n}\sum_{t=1}^{n}\sigma^0\left(L, t_i, 40°\right) \tag{5.9}$$

In equation 5.9, the variable n denotes the number of measurements recorded for a GPI at location L over time, incorporating Fore-/ Mid-/ Aft-Beam observations equivalently. Furthermore, the mean backscatter exhibited by a calibration target, $\overline{\sigma^0}(L_T, 40°)$, is computed as the mean value of the averaged backscatter response $\overline{\sigma^0}(L, 40°)$ of each GPI within the calibration target (see Eq. 5.10).

$$\overline{\sigma^0}\left(L_T, 40°\right) = \frac{1}{n_{GPI}}\sum_{L=1}^{n_{GPI}}\overline{\sigma^0}\left(L, 40°\right) \tag{5.10}$$

In order to examine spatial variations of the backscatter signature of the calibration targets, the estimated mean backscatter of the calibration target is compared to the individual mean values estimated for each GPI (see Eq. 5.11).

$$\Delta\sigma^0(L) = \overline{\sigma^0}\left(L, 40°\right) - \overline{\sigma^0}\left(L_T, 40°\right) \tag{5.11}$$

Results of this analysis are illustrated in figure 5.4, depicting spatial variations within Amazon and Congo Rainforest for AMI-WS and ASCAT. Observed spatial variations, $\Delta\sigma^0(L)$, of both targets reveal magnitudes ranging from -0.2 to 0.2 dB. Especially in the central region of the Amazon Rainforest calibration target, negative magnitudes of $\Delta\sigma^0(L)$ are found, indicative for lower backscatter values with respect to the targets average may caused by less biomass or different vegetation types within this region. For a more detailed research about spatial backscatter variations within

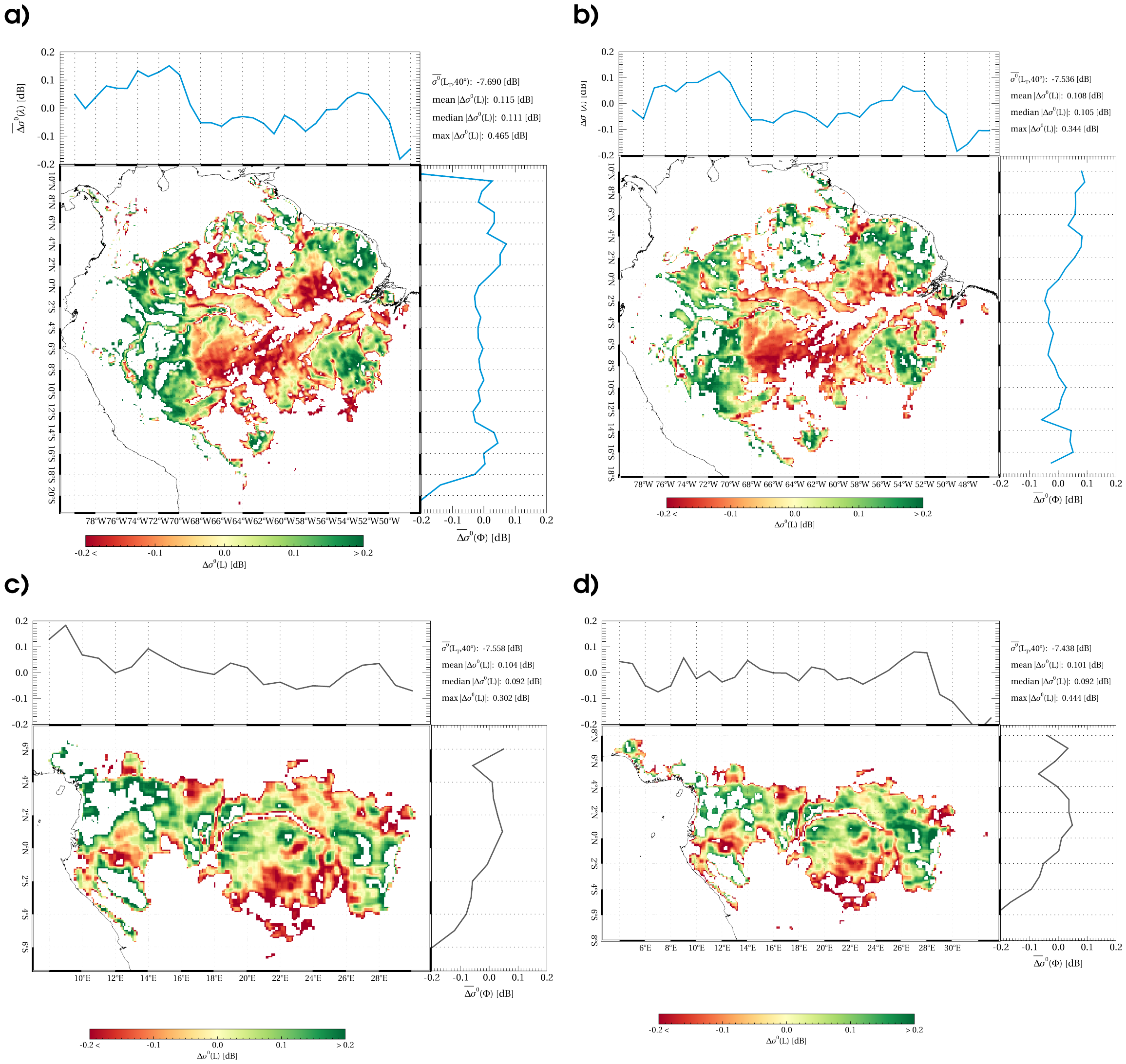

Figure 5.4: Results of the spatial variability analysis of Amazon Rainforest and Congo Rainforest for AMI-WS and ASCAT.

a) AMI-WS Amazon Rainforest b) ASCAT Amazon Rainforest
c) AMI-WS Congo Rainforest d) ASCAT Congo Rainforest

the calibration targets, mean values of $\Delta\sigma^0(L)$ were calculated in north-south and east-west geographic direction, representing the directional backscatter behaviour of the calibration targets. The north-south directional behaviour of the backscatter, $\overline{\Delta\sigma^0}(L(\Phi))$, is evaluated as the mean value of $\Delta\sigma^0(L)$ at a specific latitude Φ.

$$\overline{\Delta\sigma^0}(L(\Phi)) = \frac{1}{n_\lambda}\sum_{k=1}^{n_\lambda}\overline{\Delta\sigma^0}(L(\lambda_k,\Phi)) \tag{5.12}$$

	$\overline{\sigma^0}(L_T, 40°)$ [dB]		$\lvert\Delta\sigma^0(L)\rvert$ mean [dB]		median [dB]		max [dB]	
	AMI-WS	ASCAT	AMI-WS	ASCAT	AMI-WS	ASCAT	AMI-WS	ASCAT
Amazon Rainforest	-7.690	-7.536	0.115	0.108	0.111	0.105	0.465	0.344
Congo Rainforest	-7.558	-7.438	0.104	0.101	0.092	0.092	0.302	0.444
Indonesia Rainforest I	-7.280	-7.041	0.106	0.110	0.098	0.103	0.316	0.423
Upper Guinean Forest	-7.558	-7.522	0.111	0.109	0.107	0.106	0.310	0.355
Indonesia Rainforest II	-7.569	-7.348	0.106	0.110	0.098	0.104	0.293	0.338
Malaysian Rainforest	-7.465	-7.295	0.104	0.121	0.095	0.121	0.347	0.366
Caatinga - Brazil	-	-8.877	-	0.121	-	0.106	-	0.430
Southeastern USA Plains I	-	-9.580	-	0.117	-	0.109	-	0.335
Somalia	-	-10.201	-	0.231	-	0.205	-	0.819
Laos Rainforest	-	-7.563	-	0.104	-	0.095	-	0.309
Gran Chaco	-	-8.913	-	0.110	-	0.105	-	0.349
Southeastern USA Plains II	-	-9.805	-	0.107	-	0.096	-	0.383
Cental America Rainforest	-	-8.274	-	0.091	-	0.075	-	0.371
Western-Australia	-	-13.714	-	0.157	-	0.129	-	0.617
New Guinea Rainforest	-7.334	-	0.121	-	0.116	-	0.370	-

Table 5.2: Statistics of the spatial variability $\Delta\sigma^0(L)$ of the selected calibration targets for AMI-WS and ASCAT.

A GPI location L is determined by its longitude λ and latitude Φ coordinates. With respect to equation 5.12, $\overline{\Delta\sigma^0}(L(\Phi))$ is computed as the mean value of $\Delta\sigma^0(L)$ over the number of GPIs at a specific latitude Φ, denoted by n_λ, which is a function of the longitude λ coordinate. The directional backscatter behaviour in east-west direction is derived analogously, as the mean value of $\Delta\sigma^0(L)$ at a specific longitude λ as a function of the latitude coordinate Φ given by:

$$\overline{\Delta\sigma^0}(L(\lambda)) = \frac{1}{n_\Phi}\sum_{k=1}^{n_\Phi}\overline{\Delta\sigma^0}(L(\lambda,\Phi_k)) \ . \tag{5.13}$$

Both estimates of the backscatter directionality, $\overline{\Delta\sigma^0}(L(\Phi))$ and $\overline{\Delta\sigma^0}(L(\lambda))$, are depicted in figure 5.4 for Amazon and Congo Rainforest. In general, the observed directional variations of the NRCS, estimated for Amazon and Congo Rainforest, are consistent for both scatterometer missions. As can be distinguished for Amazon Rainforest, $\overline{\Delta\sigma^0}(L(\Phi))$ is almost stable across the examined latitudes. But with respect to AMI-WS, inhomogeneities to the mean backscatter $\overline{\sigma^0}(L_T, 40°)$ were found in the North and South of the target, mainly caused by a reduced amount of GPIs in these regions. The Congo rainforest, on the other hand, exhibit lower backscatter values in the South of the target, compared to the targets mean value, displayed by negative magnitudes of $\overline{\Delta\sigma^0}(L(\Phi))$ ranging from -0.1 dB to less than -0.2 dB for latitudes below 4° South.

Spatial backscatter variations in east-west direction of the Amazon Rainforest calibration target indicate a general backscatter trend with decreasing values of $\overline{\Delta\sigma^0}(L(\lambda))$ from West to the East, recognisable for both European scatterometers. This trend is superimposed by positive values of $\Delta\sigma^0(L)$ in the far East and West of the calibration target. An equivalent trend is observed for Congo Rainforest in terms of AMI-WS (see figure 5.4c). Longitudinal mean backscatter variations $\overline{\Delta\sigma^0}(L(\lambda))$ of the Congo Rainforest observed for ASCAT, reveal almost constant values ranging from -0.1 to 0.1 dB, neglecting the far-west region with an estimated mean backscatter deviation below -0.2 dB.

Further statistics of the investigated spatial variability parameter $\Delta\sigma^0(L)$ are given in table 5.2 for each calibration target of AMI-WS and ASCAT individually. The provided statistics encompass the mean, median and maximum value of the absolute value of $\Delta\sigma^0(L)$ complemented by the mean backscatter of the entire calibration target $\overline{\sigma^0}(L_T, 40°)$. With reference to the selected AMI-WS calibration targets, Congo Rainforest was found to be the most spatial homogeneous target in consideration of the provided statistics. On the other hand, the Central America Rainforest was distinguished as the most spatial homogeneous ASCAT calibration target, although the covered area of this target is rather small in comparison to extensive area targets like Amazon or Congo Rainforest. The mean absolute spatial variability of AMI-WS calibration targets is ranging from 0.104 dB for Congo Rainforest to 0.121 dB for the New Guinea Rainforest. In general, the average spatial variability, either the mean or the median values, of all considered AMI-WS and ASCAT calibration targets is approximately 0.1 dB. But with the exception of the sparsely vegetated calibration sites selected for ASCAT calibration, which reveal median values of the spatial variability of 0.205 dB for Somalia and 0.129 dB for Western-Australia.

5.3.3.2 Temporal Backscatter Variability

Besides the spatial homogeneity of the calibration targets, a temporal stable backscatter response is vital for relative radiometric calibration of space-borne scatterometers. The temporal variability parameter $v(L, 40°)$ was introduced in chapter 4.4.2 as an observation configuration independent measure of the temporal backscatter variability, estimated individually for all GPIs on the Discrete Global Grid (DGG). However, the parameter $v(L, 40°)$ is inappropriate to quantify the total temporal backscatter variability of the extended area calibration targets. As a consequence, two temporal variability measures were examined, one accounting for residual spatial variations within the extended area targets and one quantifying the total temporal backscatter variability. An estimate of the backscatter temporal variability, unaffected by residual spatial variations within the target, is employed closely following the derivation of the temporal variability parameter $v(L, 40°)$ introduced in chapter 4.4.2. The variance $v_t^2(L, 40°)$ of a single GPI within the calibration target can be calculate by utilising the following equation given by:

$$v_t^2(L, 40°) = \frac{1}{n}\sum_{i=1}^{n}\left(\sigma^0(L, t_i, 40°) - \overline{\sigma^0}(L, 40°)\right)^2 . \tag{5.14}$$

	$v_t(L_T, 40°)$ [dB]		$v_{spt}(L_T, 40°)$ [dB]		$\max\left(v_{spt}(L_T, 40°, t_M)\right)$ [dB]	
	AMI-WS	ASCAT	AMI-WS	ASCAT	AMI-WS	ASCAT
Amazon Rainforest	0.302	0.226	0.334	0.262	0.342	0.282
Congo Rainforest	0.305	0.232	0.333	0.265	0.358	0.283
Indonesia Rainforest I	0.328	0.220	0.356	0.257	0.425	0.274
Upper Guinean Forest	0.357	0.315	0.394	0.351	0.510	0.440
Indonesia Rainforest II	0.365	0.266	0.387	0.298	0.410	0.335
Malaysian Rainforest	0.371	0.274	0.398	0.314	0.448	0.352
Caatinga - Brazil	-	0.468	-	0.504	-	0.639
Southeastern USA Plains I	-	0.461	-	0.489	-	0.613
Somalia	-	0.450	-	0.535	-	0.669
Laos Rainforest	-	0.392	-	0.427	-	0.503
Gran Chaco	-	0.409	-	0.436	-	0.498
Southeastern USA Plains II	-	0.467	-	0.493	-	0.596
Cental America Rainforest	-	0.363	-	0.389	-	0.484
Western-Australia	-	0.535	-	0.574	-	0.757
New Guinea Rainforest	0.315	-	0.346	-	0.376	-

Table 5.3: Estimates of the temporal variability discovered for the selected extended area land-targets suitable for calibration.

It is worth mentioning that azimuthal isotropic backscatter behaviour is presumed, considering observations from different antenna beams (azimuth configurations ϕ_j) equivalently in the calculation of $v_t^2(L, 40°)$. Furthermore, the variance $v_t^2(L, 40°)$ is calculated over time, indicated by the parameter n denoting the number of backscatter observations at GPI location L. The unbiased parameter $v_t(L_T, 40°)$ is derived by utilising the pooled standard deviation, representing the temporal variability of a calibration target L_T, unaffected by spatial variations but incorporating residual azimuthal effects. Hence, the parameter $v_t(L_T, 40°)$ give an estimate of the expected temporal variability of the extend area calibration targets, supposed to be perfectly homogeneous over space.

$$v_t\left(L_T, 40°\right) = \sqrt{\frac{\sum_{L=1}^{n_{GPI}} n\, v_t^2(L, 40°)}{\sum_{L=1}^{n_{GPI}} n}} \tag{5.15}$$

As stated in chapter 5.3.3.2, the selected calibration targets exhibit spatial variations revealed in deviations between the mean backscatter of individual GPIs and the total mean backscatter of the target. However, with respect to the proposed calibration methodology, each extended area calibration target is supposed to act like a spatial homogeneous calibration reference. As consequence, any spatial backscatter variations within a calibration site will contribute additional deviations to the total temporal variability. A measure of the total temporal variability is found with the parameter $v_{spt}(L_T, 40°)$, comprising the net temporal variability inclusively residual spatial and azimuthal variations of the calibration target, given by the following equation 5.16.

$$v_{spt}\left(L_T, 40°\right) = \sqrt{\frac{1}{n}\sum_{i=1}^{n}\left(\sigma^0\left(L, t_i, 40°\right) - \overline{\sigma^0}\left(L_T, 40°\right)\right)^2} \tag{5.16}$$

Values of the temporal variability parameters $v_t(L_T, 40°)$ and $v_{spt}(L_T, 40°)$, estimated for all extended area land-targets selected for AMI-WS and ASCAT calibration, are summarised in table 5.3. By exploring the difference between $v_t(L_T, 40°)$ and $v_{spt}(L_T, 40°)$, it can be shown that most of the backscatter coefficient variability of the calibration targets is caused by temporal variations rather than by spatial variations. Estimates of the total temporal variability $v_{spt}(L_T, 40°)$ state that values discovered for ASCAT are in general smaller than those found for AMI-WS with respect to coincident calibration targets. Overall, coexisting calibration targets reveal a total temporal variability $v_{spt}(L_T, 40°)$ less than the defined temporal stability threshold, specified in the target selection scheme (see Tab. 4.2). Although, additional targets selected for ASCAT calibration expose a total temporal variability greater than 0.4 dB, with the exception of the Central America Rainforest and Laos Rainforest with regard to the spatially unbiased temporal variability parameter $v_t(L_T, 40°)$. Minimum values of the temporal variabilities $v_t(L_T, 40°)$ and $v_{spt}(L_T, 40°)$ are found for Amazon and Congo Rainforest for both European scatterometer, complemented by Indonesia Rainforest I with respect to ASCAT and the New Guinea Rainforest for AMI-WS respectively.

The previous performed analysis characterise the average temporal backscatter variability of the calibration targets. Additional examinations are conducted, concentrating on possible variations in the temporal variability parameter $v_{spt}(L_T, 40°)$ for each month of the year. Thus, the total temporal variability of a calibration target was calculated by extending equation 5.16 by the function argument t_m, resulting in:

$$v_{spt}\left(L_T, t_M, 40°\right) = \sqrt{\frac{1}{n_M}\sum_{i=1}^{n_M}\left(\sigma_i^0\left(L, MOY\left(t_i\right), 40°\right) - \overline{\sigma^0}\left(L_T, 40°\right)\right)^2}, \tag{5.17}$$

where n_M denotes the number of observations record in month t_M. Figure 5.5 illustrates the monthly temporal variability $v_{spt}(L_T, t_M, 40°)$ determined for each calibration target of AMI-WS and ASCAT separately. The temporal variability $v_{spt}(L_T, t_M, 40°)$ persist constant across the different months of the year for almost each AMI-WS calibration target. Anyhow, from January to April increases of the temporal variability are apparent for Malaysian Rainforest, Upper Guinean Forest and Indonesia Rainforest I. Applicable calibration targets extracted for ASCAT calibration, with an average temporal variability greater than 0.4 dB, display a seasonal cycle of the predicted temporal variability parameter $v_{spt}(L_T, t_M, 40°)$. Especially selected sparsely vegetated calibration sites, Somalia and Western-Australia, exhibit differences in the temporal variability of approximately 0.1 dB across different months. With respect to the complete number of calibration

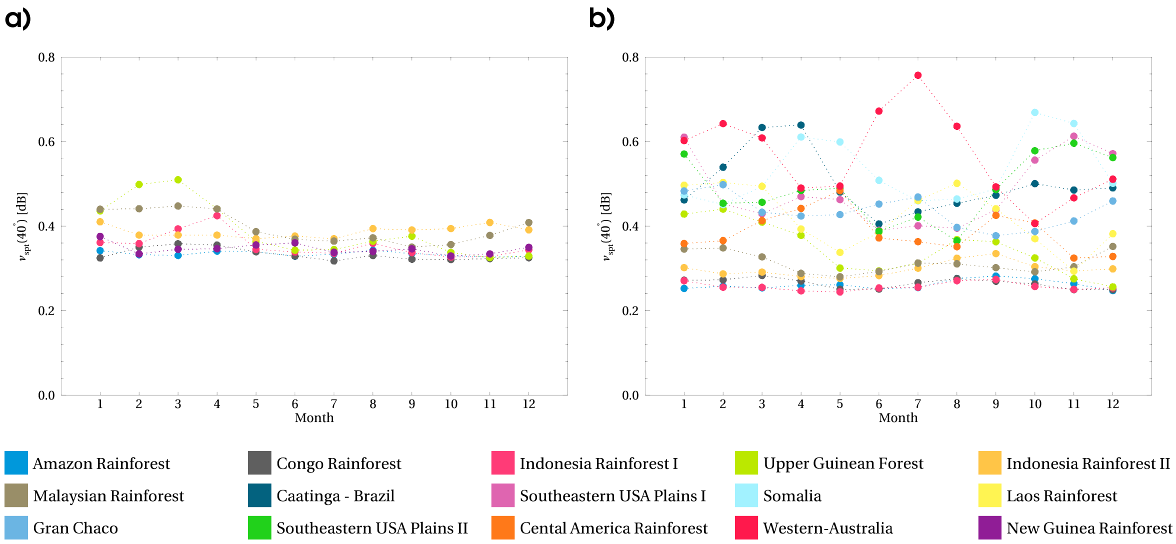

Figure 5.5: Monthly temporal backscatter variability exhibited by the selected extended area calibration targets of a) AMI-WS and b) ASCAT.

targets, minimum values of the monthly temporal variability are in general found for months ranging from June to September. Maximum values of $\nu_{spt}(L_T, t_M, 40°)$ observed with this analysis are listed in table 5.3, highlighting the worst case scenario expected for each calibration target.

So far, all investigated statistics, concentrating on the temporal backscatter variability of the selected calibration targets, were computed with reference to a temporal invariant mean backscatter $\overline{\sigma^0}(L_T, 40°)$, neglecting potential land cover dynamics like vegetation development which control the magnitude of the backscatter coefficient. Since most of the selected calibration targets are covered by dense vegetation, it is supposed that the computed temporal variabilities, tabulated in table 5.3, incorporate backscatter variations driven by vegetation phenology. Daily averages of the incidence angle normalised backscatter response of several calibration targets $\sigma^0(L_T, t_i, 40°)$ are depicted in figure 5.6, highlighting a strong backscatter seasonality due to vegetation dynamics of the given calibration targets. Consequently, efforts have been undertaken to predict and remove the observed deterministic seasonal component from the incidence angle normalised backscatter time series for each calibration target. The commonly used additive time series decomposition, see equation 5.19, was employ to decompose the time series into the deterministic trend component σ^0_{Trend}, the deterministic seasonal component σ^0_{Season} and the stochastic irregular component σ^0_{Irr} [*Cowpertwait and Metcalfe*, 2009].

$$\sigma^0\left(L_T, t_i, 40°\right) = \sigma^0_{Trend}\left(L_T, t_i, 40°\right) + \sigma^0_{Season}\left(L_T, t_i, 40°\right) + \sigma^0_{Irr}\left(L_T, t_i, 40°\right) \tag{5.18}$$

In terms of the proposed calibration methodology, the interest is in the trend component of the calibration target time series supposed to reflect calibration anomalies in the investigated scat-

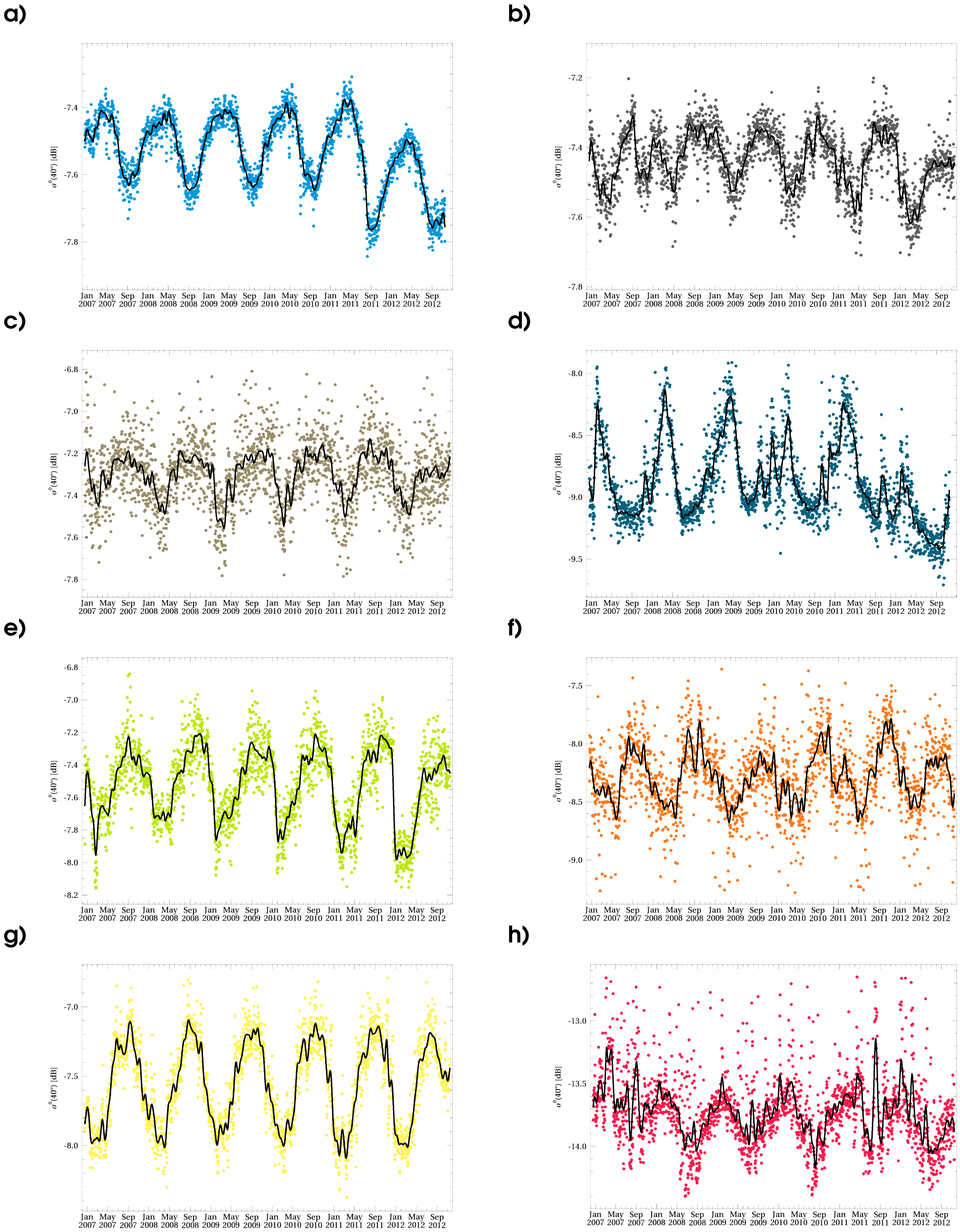

Figure 5.6: Temporal evolution of the backscatter coefficient σ^0 (40°) found for extended area calibration targets of ASCAT. Additionally a 31-day moving average window was applied to the data illustrated as solid black line.

a) Amazon Rainforest	b) Congo Rainforest	c) Malaysian Rainforest
d) Caatinga Brazil	e) Upper Guinean Forest	f) Cental America Rainforest
g) Laos Rainforest	h) Western-Australia	

terometer system. The deterministic seasonality is examined by a so-called stable seasonal filter by calculating the average of all backscatter coefficients for each day of the year. Results of the additive time series decomposition are illustrated in figure 5.7 for Amazon Rainforest (AMI-WS) and Malaysian Rainforest (ASCAT). The seasonal component, plotted in figure 5.7, was added to the trend component of the decomposed time series to fit the data range. Subtracting the seasonal component σ^0_{Season} from the raw backscatter time series will result in the deterministic trend component σ^0_{Trend} superimposed by the irregular component σ^0_{Irr}, leading to the seasonal adjusted time series given by:

$$\sigma^0_{adj}\left(L_T, t_i, 40°\right) = \sigma^0\left(L_T, t_i, 40°\right) - \sigma^0_{Season}\left(L_T, t_i, 40°\right) = \sigma^0_{Trend}\left(L_T, t_i, 40°\right) + \sigma^0_{Irr}\left(L_T, t_i, 40°\right) . \tag{5.19}$$

The irregular component consists of remaining non-predictable short-term variations and instrument noise of the $\sigma^0\,(L_T, t_i, 40°)$ time series. In other words, the irregular component constitutes the precision to determine the deterministic trend component. Finally an additional measure of the temporal variability, denoted as v_{adj}, of the calibration targets is determined by calculating the root mean square difference between the seasonal adjusted time series σ^0_{adj} and the temporal invariant mean backscatter $\overline{\sigma^0}\,(L_T, 40°)$.

$$v_{adj}\left(L_T, 40°\right) = \sqrt{\frac{1}{n}\sum_{i=1}^{n}\left(\sigma^0_{adj}\,(L_T, t_i, 40°) - \overline{\sigma^0}\,(L_T, 40°)\right)^2} \tag{5.20}$$

Results of this analysis are provided in table 5.4 for each extended area land-target applicable for radiometric calibration. By comparing these results to the temporal variability parameter $v_{spt}\,(L_T, 40°)$ given table 5.3, it is obvious that most of the observed temporal variability is caused by contributions of the deterministic seasonal backscatter cycle. Seasonal contributions observed for the investigated calibration targets of AMI-WS and ASCAT are approximately 0.2 dB on average with maximum values found in the order of 0.3 dB for Somalia and Laos Rainforest. Residual variations of the calibration targets determined by the parameter v_{adj} reveal backscatter variations less then 0.342 dB for the selected calibration targets with minimum values found for Amazon Rainforest and Congo Rainforest.

5.4 AMI-WS and ASCAT Intra-Calibration

The theoretical baseline of the developed sensor intra-calibration methodology is outlined in chapter 4.5, with the objective of monitor and correct for residual calibration anomalies, reflected in the recorded normalised radar cross section (NRCS) of a scatterometer. In terms of fan-beam scatterometers, calibration anomalies are considered to be found for individual antenna beams or the entire instrument as a result of sensor component alterations over time. Furthermore, systematic errors are taken into account, displayed in biases between observations of different an-

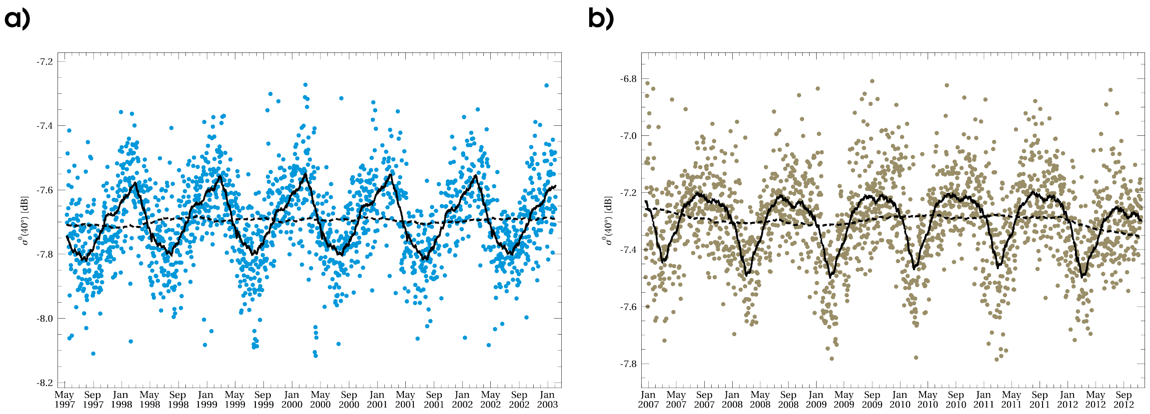

Figure 5.7: Trend [dashed line] and seasonal [solid line] component estimated for a) Amazon Rainforest [AMI-WS] and b) Malaysian Rainforest [ASCAT] incidence angle normalised backscatter coefficient time series.

tenna beams. The ascertainment of such radiometric deficiencies will be examined throughout sensor intra-calibration, based on carefully selected natural calibration targets over land, featured by unique backscatter attributes. As can be envisioned, the developed sensor intra-calibration methodology is not capable to quantify the absolute relationship between the raw instrument recordings and the physical quantity of interest. But the proposed method is applicable to quantify variations of the relationship relative to a defined calibration reference, determined by the unique backscatter response explored by a set of natural calibration targets.

Within the previous section 5.3 of this work, backscatter characteristics of suitable extended area land-targets were analysed intensively to prove and confirm their capability for calibration of C-band scatterometers. Various statistics are presented for both European scatterometer missions, highlighting different target backscatter attributes with respect to azimuthal anisotropy, backscatter incidence angle behaviour as well as spatial and temporal backscatter variations. According to the computed statistics, extended are land-targets are classified into calibration targets, used to infer calibration parameters, and verification targets to verify results of the applied calibration corrections. Targets characterised by minimum values across the provided statistics are designated as calibration targets, resulting in three calibration targets for both C-band scatterometers. Calibration targets used to infer calibration coefficients are Amazon Rainforest, Congo Rainforest, New Guinea Rainforest (AMI-WS) and Indonesia Rainforest I (ASCAT). Remaining AMI-WS targets are assigned as calibration verification targets, supplemented by Upper Guinean Forest, Indonesia Rainforest II, Malaysian Rainforest and Laos Rainforest in terms of verifying ASCAT calibration results. Residual ASCAT targets selected with the developed threshold based decision scheme like Caatinga-Brazil, Southeastern USA Plains, Somalia, Gran Chaco, Central America Rainforest and Western-Australia are neglected in the following calibration process, because of revealing significantly higher statistics in comparison to the considered targets for calibration and verification.

	$\nu_{adj}(L_T, 40°)$ [dB] AMI-WS	$\nu_{adj}(L_T, 40°)$ [dB] ASCAT
Amazon Rainforest	0.120	0.060
Congo Rainforest	0.140	0.072
Indonesia Rainforest I	0.221	0.105
Upper Guinean Forest	0.194	0.144
Indonesia Rainforest II	0.190	0.129
Malaysian Rainforest	0.232	0.139
Caatinga - Brazil	-	0.254
Southeastern USA Plains I	-	0.311
Somalia	-	0.211
Laos Rainforest	-	0.154
Gran Chaco	-	0.338
Southeastern USA Plains II	-	0.342
Cental America Rainforest	-	0.286
Western-Australia	-	0.329
New Guinea Rainforest	0.151	-

Table 5.4: Temporal variability estimated from the stochastic irregular component derived through time series decomposition for the selected extended area land-targets suitable for calibration.

5.4.1 Determination of the Calibration Reference

Sensor intra-calibration is performed with respect to a defined calibration reference $\overline{\sigma^0}(L_T, \theta)$ established for each calibration target. The backscatter response of calibration targets is postulated to be perfectly isotropic in azimuth, stable over time and spatial homogeneous. As a result, the true backscatter response $\widetilde{\sigma^0}$ of a calibration target L_T is supposed to be a function of the incidence angel θ exclusively, as already discussed in chapter 4.5. Furthermore, it is assumed that the scatterometer under investigation is perfectly calibrated, $\widetilde{C_{IAS}}(t_i, \theta, \phi) = 0$, for the time being. With these assumptions a measurement model of the observed normalised radar cross section $\sigma^0(L_T, t_i, \theta, \phi)$ can be explicitly derived for each calibration target given by:

$$\sigma^0(L_T, t_i, \theta, \phi) = \widetilde{\sigma^0}(L_T, \theta) + \epsilon\,, \tag{5.21}$$

where individual observations are assumed to deviate from the true normalised radar cross section $\widetilde{\sigma^0}(L_T, \theta)$ by an additive instrument noise term ϵ. With reference to equation 5.21, an estimate of the true backscatter coefficient $\widetilde{\sigma^0}(L_T, \theta)$ can be determined for each calibration target as a function of the incidence angle by averaging a sufficient number of observations. As a

		AMI-WS			ASCAT		
		B_0	B_1	B_2	B_0	B_1	B_2
	overpass dir.	[dB]	[dB/deg]	[dB/deg^2]	[dB]	[dB/deg]	[dB/deg^2]
Amazon Rainforest	asc	-7.728	-0.062	-0.0012	-7.578	-0.074	-0.0015
	desc	-7.641	-0.063	-0.0013	-7.458	-0.075	-0.0017
Congo Rainforest	asc	-7.661	-0.059	-0.0013	-7.507	-0.071	-0.0016
	desc	-7.479	-0.064	-0.0015	-7.295	-0.076	-0.0018
Indonesia Rainforest I	asc	-	-	-	-7.049	-0.073	-0.0017
	desc	-	-	-	-6.960	-0.073	-0.0019
New Guinea Rainforest	asc	-7.365	-0.063	-0.0013	-	-	-
	desc	-7.271	-0.060	-0.0010	-	-	-

Table 5.5: Polynomial coefficients characterising the backscatter calibration reference for selected calibration targets.

consequence, the predicted backscatter coefficient $\overline{\sigma^0}(L_T,\theta)$ constitutes the backscatter calibration reference of each target to infer potential instrument related variations. Referring to chapter 5.3.2, the backscatter versus incidence angle dependency of the calibration targets was found to be adequately modelled by a 2-order-polynomial function centred at 40 degrees incidence angle as stated in the following equation.

$$\overline{\sigma^0}(L_T,\theta) = \frac{1}{n}\sum_{i=0}^{n}\sigma^0\left(L_T,t_i,\theta,\phi_j\right) = B_0\left(L_T,40°\right) + \sum_{p=1}^{p_{order}=2} B_p\left(L_T,40°\right) * \left(\theta - 40°\right)^p \tag{5.22}$$

AMI-WS data of a the entire year 1998 are considered for the determination of the calibration reference $\overline{\sigma^0}(L_T,\theta)$ and backscatter observations recorded in 2007 are regarded for ASCAT respectively. Polynomial coefficients of the backscatter calibration reference are determined by an ordinary least square estimation with respect to the extracted data. Additionally, the extracted data used to determine the calibration reference was corrected for the observed backscatter seasonality as identified in chapter 5.3.3.2. Moreover, considering a full year of data has the advantage to account for residual backscatter variations not captured by the applied seasonality in the computation of $\overline{\sigma^0}(L_T,\theta)$. Backscatter observations were discriminated in terms of the satellite overpass direction; ascending and descending overpass; to account for known systematic differences in the recorded backscatter coefficient as equally observed by *Friesen et al.* [2012]. Estimated backscatter calibration references for New Guinea Rainforest, based on AMI-WS data, and Amazon Rainforest for ASCAT calibration are depicted in figure 5.8, separately for ascending and descending overpass. Polynomial coefficients of the backscatter calibration reference assessed for the selected calibration targets are listed in table 5.5 for sake of completeness. Differences in the backscatter calibration reference between ascending and descending satellite overpasses are distinguishable especially in the coefficient B_0 of the polynomial function. Observed differences are

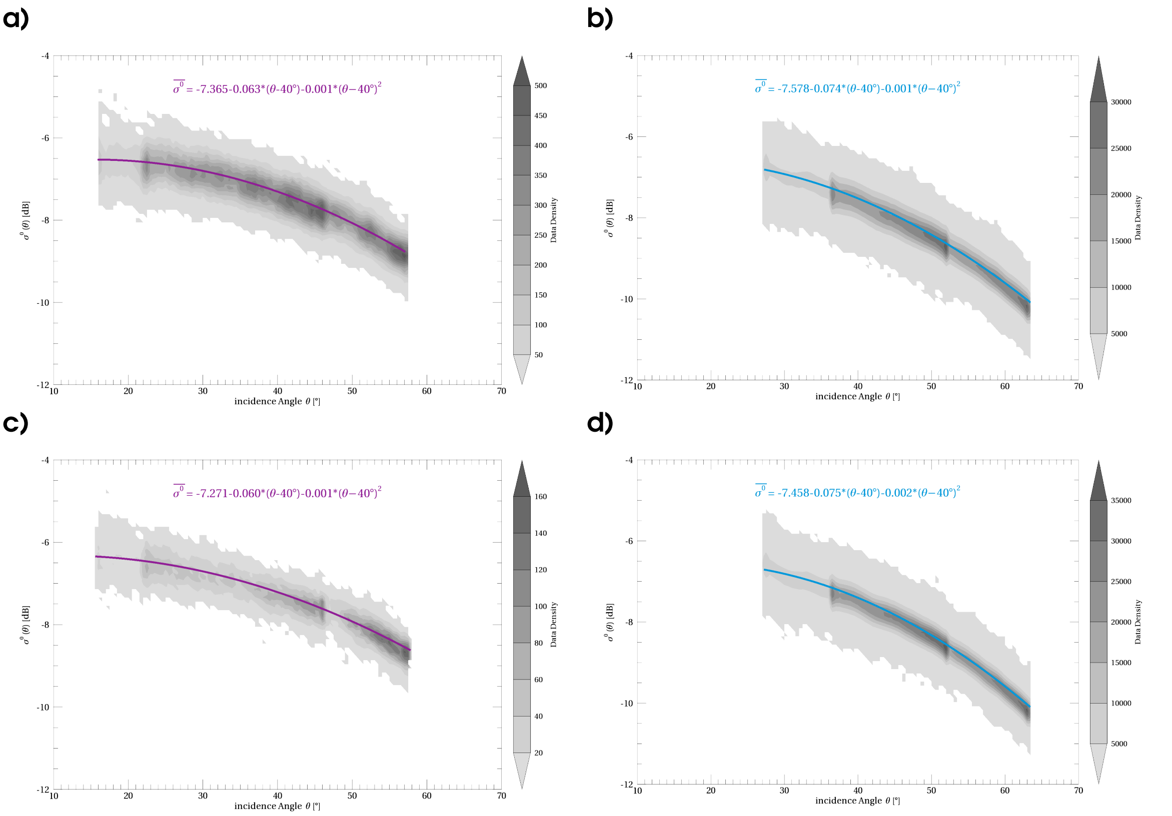

Figure 5.8: Estimated backscatter calibration references [solid line] of New Guinea Rainforest [AMI-WS a) ascending c) descending overpass] and Amazon Rainforest [ASCAT b) ascending d) descending overpass] with underlying data density plot depicting the amount of data per incidence angle used to predict the reference.

in the order of approximately 0.1 to 0.2 dB, and dissimilarities explored for the coefficients B_1 and B_2 are less significant. So far, the source of these overpass differences is unexplained, but possible causes are either related to the sensor itself, due to variations in the sun illumination, or related to processes on the land surface with respect to different observation times. Thus, backscatter observations recorded at different satellite overpasses are treated individually in the proceeding calibration approach to precisely determine calibration parameters for each scatterometer system.

5.4.2 Estimation of AMI-WS and ASCAT Intra-Calibration Coefficients

The derived backscatter calibration reference $\overline{\sigma^0}(L_T,\theta)$ constitutes the "true" time invariant backscatter response of each calibration target. Hence, deviations of the recorded backscatter coefficient $\sigma^0\left(L_T,t_i,\theta,\phi_j\right)$ to the calibration reference $\overline{\sigma^0}(L_T,\theta)$ are held to give estimates of calibration anomalies incorporated in the calibration coefficient $\widetilde{C_{IAS}}\left(t_i,\theta,\phi_j\right)$. In the case of the European scatterometers AMI-WS and ASCAT, calibration anomalies can affect particular antenna beams or the entire scatterometer system. Hence, inter-calibration coefficients are determined for each scatterometer antenna beam separately, covering the entire data period of AMI-WS and ASCAT (see table 4.1). Estimates of the sensor intra-calibration coefficient $\widetilde{C_{IAS}}\left(t_i,\theta,\phi_j\right)$ are computed by utilising equation 4.12, as stated in chapter 4.5, which is recapitulated within this section for convenience.

$$C_{IAS}\left(L_T,t_i,\theta,\phi_j\right)=\widetilde{C_{IAS}}\left(L_T,t_i,\theta,\phi_j\right)+\epsilon=\sigma^0\left(L_T,t_i,\theta,\phi_j\right)-\overline{\sigma^0}\left(L_T,\theta\right) \tag{5.23}$$

The presented intra-calibration methodology foresees the use of numerous calibration targets for a robust determination of the scatterometer related calibration coefficient $\widetilde{C_{IAS}}\left(t_i,\theta,\phi\right)$. Due to differences in the spatial extent of the individual calibration targets, the number of observations per time period vary from target to target. To assure a robust and well sampled estimation of the calibration coefficient as a function of the incidence angle θ, observations recorded during an entire month are gathered to deduce calibration parameters for all antenna beams independently, discriminating between ascending and descending orbit overpasses. As a result, calibration parameters are determined for each month of the considered scatterometer dataset to identify calibration related variations over time defined by:

$$\overline{C_{IAS}}\left(L_T,t_i,\theta,\phi_j\right)=\frac{1}{n}\sum_{i=1}^{n}C_{IAS}\left(L_T,t_i,\theta,\phi_j\right)=C_0\left(L_T,t_i,40^\circ,\phi_j\right)+C_1\left(L_T,t_i,40^\circ,\phi_j\right)*\left(\theta-40^\circ\right)\ . \tag{5.24}$$

The calibration coefficient $\overline{C_{IAS}}\left(L_T,t_i,\theta,\phi_j\right)$ serve as an estimate of the desired calibration coefficient $\widetilde{C_{IAS}}\left(t_i,\theta,\phi_j\right)$, determined for each calibration target L_T by employing equation 5.24 to the observed calibration anomalies $C_{IAS}\left(L_T,t_i,\theta,\phi_j\right)$ in a specific month t_i. Figure 5.9 illustrates calibration anomalies in a data density plot assessed for AMI-WS and ASCAT data in July 1999 and July 2010 respectively. In order to infer continuous calibration information across the complete range of incidence angles θ, a 1-order-polynomial function is fitted to the observed variations, representing the calibration anomaly $\overline{C_{IAS}}\left(L_T,t_i,\theta,\phi_j\right)$ investigated for a single calibration target. In the case of ASCAT, monitored calibration variations indicate oscillating alterations with respect to the incidence angle which are not distinguishable in the observed AMI-WS calibration anomalies. Currently, no reasonable explanation was found for the reason of these oscillations observed for ASCAT. The 1-order-polynomial function used to model the calibration anomaly $\overline{C_{IAS}}\left(L_T,t_i,\theta,\phi_j\right)$ is adequate to remove insufficiencies with respect to biases and 1-order deviations revealed in the monthly calibration coefficients. However, the used calibration targets are natural targets on the Earth's surface which may encounter possible variability over time in the overall backscatter response. Causes for possible variabilities are either human induced, like deforestation, or due to climate changes affecting the predominate land cover resulting in potential backscatter variations. The objective of intra-calibration is to discover potential instrument related backscatter variations rather than variations related to the calibration target itself. Therefore, the proposed sensor intra-calibration method make use of various calibration targets for a

a)

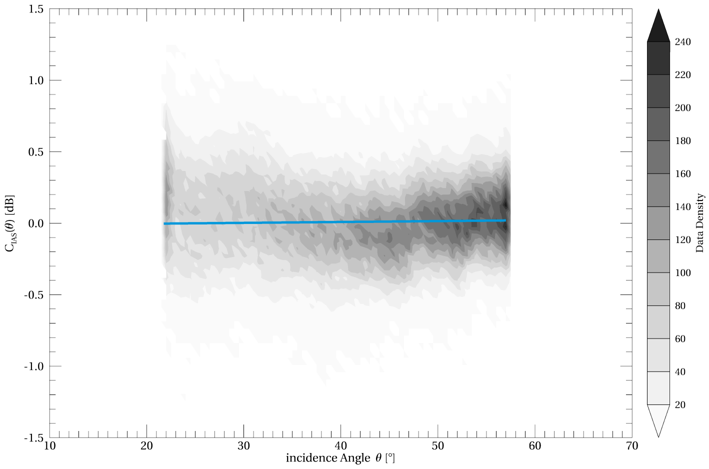

b)

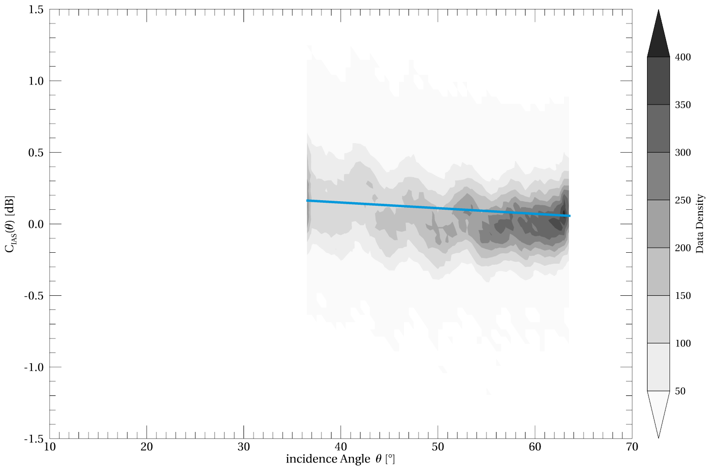

Figure 5.9: Calibration anomalies $\overline{C_{IAS}}\left(L_T, t_i, \theta, \phi_j\right)$ in the right swath fore-beam antenna observed for a) AMI-WS in July 1999 and b) ASCAT in July 2010 by utilising Amazon Rainforest.

robust prediction of potential temporal scatterometer calibration anomalies. Considering various targets for calibration simultaneously will reduce the risk to falsely interpret target related variations as potential instrument drifts. Consequently, the final calibration coefficient $\overline{C_{IAS}}\left(t_i, \theta, \phi_j\right)$ is derived as the weighted average of the individually determined coefficients $\overline{C_{IAS}}\left(L_T, t_i, \theta, \phi_j\right)$ of each calibration target L_T as stated in the following equation.

$$\overline{C_{IAS}}\left(t_i, \theta, \phi_j\right) = \frac{\sum_{T=1}^{n_{TAR}} w\left(L_T, t_i, \phi_j\right) \overline{C_{IAS}}\left(L_T, t_i, \theta, \phi_j\right)}{\sum_{T=1}^{n_{TAR}} w\left(L_T, t_i, \phi_j\right)} \tag{5.25}$$

The average is computed over the number of calibration targets denoted by n_{TAR}, given that the calibration coefficient $\overline{C_{IAS}}\left(t_i, \theta, \phi_j\right)$ is independent of the regarded calibration target L_T. The introduction of the weighted mean, instead of the arithmetic mean, for the calculation of calibration coefficient $\overline{C_{IAS}}\left(t_i,\theta,\phi_j\right)$ is reasonable in terms of considering the quality of each calibration target for contributing significant calibration information. With respect to this, the weights $w\left(L_T,t_i,\phi_j\right)$ comprise the goodness of fit of the calibration reference $\overline{\sigma^0}\left(L_T,\theta\right)$ and of the derived calibration coefficient $\overline{C_{IAS}}\left(L_T,t_i,\theta,\phi_j\right)$, represented by the mean squared error (MSE). The goodness of fit of the calibration reference is denoted as MSE_{Ref} and the mean squared error of the calculated calibration coefficient is termed as $MSE_{C_{IAS}}$. Weights $w\left(L_T,t_i,\phi_j\right)$ of the different calibration targets are inferred over time t_i for each antenna beam at azimuth angle ϕ_j.

$$w\left(L_T,t_i,\phi_j\right)=\frac{1}{MSE_{Ref}\left(L_T,\phi_j\right)}+\frac{1}{MSE_{C_{IAS}}\left(L_T,t_i,\phi_j\right)} \tag{5.26}$$

As a result, calibration coefficients $\overline{C_{IAS}}\left(t_i,\theta,\phi_j\right)$ are retrieved for each individual antenna beam over time t_i by incorporating estimates of ascending and descending overpasses equivalently as depicted in figure 5.9. The indiscriminate incorporation of calibration coefficients estimated for ascending and descending overpasses is meaningful, because the observed variations are a characteristic of a specific antenna beam and not related to different overpass times. Due to the usage of a 1-order-polynomial function for the estimation of calibration anomalies, intra-sensor calibration coefficients can be derived for arbitrary incidence angles to correct for observed calibration deviations. In figure 5.10 and 5.11, the intra-calibration coefficient at 40 degrees incidence angle $\overline{C_{IAS}}\left(t_i,40°,\phi_j\right)$ is plotted as function of time, illustrating antenna drifts discovered with the proposed methodology for AMI-WS and ASCAT. Additionally, intra-calibration coefficients determined for the individual calibration targets $\overline{C_{IAS}}\left(L_T,t_i,40°,\phi_j\right)$ are shown separately for ascending and descending overpass. A perfectly intra-calibrated sensor will be identified by a temporal constant coefficient $\overline{C_{IAS}}\left(t_i,40°,\phi_j\right)$ equal to 0, denoting that the observed backscatter response of a specific antenna beam is equal to the calibration reference over time. Positive deviations to the calibration reference indicate an attenuation of the antenna response while negative values of the intra-calibration coefficient represent amplifications in comparison to the reference.

Relatively constant intra-calibration coefficients are found for AMI-WS Fore- and Mid-beam antennas revealing a temporal invariant bias of the antenna beams, with magnitudes of 0.009 dB and 0.09 dB on average to the defined calibration references (see figure 5.10a and 5.10b). In addition, the benefit of employing the weighted average for the calculation of the intra-calibration coefficient $\overline{C_{IAS}}\left(t_i,\theta,\phi_j\right)$ is obvious, especially for coefficients determined from May 1997 to January 1998. In this period the New Guinea Rainforest target hypothesised inconsistent calibration anomalies with respect to the other used targets. However, throughout the averaging process such inconsistencies are taken care of by means of the introduced weights $w\left(L_T,t_i,\phi_j\right)$. In case of the Aft-beam antenna of AMI-WS, see figure 5.10a, almost constant intra-calibration coefficients can be distinguished until May 2001 followed by a rapid decrease of the coefficients with a peak value of -0.2 dB detected in January 2002 indicating backscatter amplifications. After January 2002 estimated intra-calibration coefficients converge towards to the defined calibration reference. The date of this calibration anomaly correspond to the so-called Zero Gyro Mode (ZGM) in which ERS-2 was piloted after January 2001. Although the investigated AMI-WS data were reprocessed within the ASPS processing facility, accounting for the failure of the Attitude and Orbit Control System (AOCS) in January 2001 of ERS-2, it is likely that the detected calibration anomalies of the Aft-beam antenna are residual artefacts related to this mission event.

Calibration variations encountered for ASCAT, see figure 5.11, reveal almost constant biases to the calibration reference from January 2007 to September 2009 for all antenna beams. A good analogy is distinguishable between the Mid-beam antenna of the right swath and the calibration reference for this time period, evidently in small deviations of intra-calibration coefficient. Anomalies in the calibration coefficient are perceived after September 2009 in the Aft-beam antenna of the left swath, highlighting magnitudes up to -0.1 dB (see. figure 5.11c). A possible explanation of this abnormal antenna beam behaviour was explored in the ASCAT product guide [*EUMETSAT*, 2013, table 3.2], summarising the ASCAT Level-1 on-ground processing software version history. Before September 2009 the on-ground processing software was based on static look-up-tables comprising normalisation factors used to convert the raw instrument recording into the normalised radar cross section σ^0. But in September 2009 the processing chain was updated to the so-called dynamic Normalisation Table Baseline (NTB) generation, capable to compute normalisation factors on the fly for the actual MetOp orbit. It is likely that the detected calibration anomaly in the left swath Aft-beam antenna is related to this on-ground processor update. Concentrating on the period after January 2011 an increase of the antenna gain is distinguishable for all antenna beams until February 2012. The reason of this calibration anomaly in the data is supposed to be caused by the implementation of the 2010 transponder calibration in the on-ground processor software [*EUMETSAT*, 2013]. As a consequence, data recorded after February 2012 are aligned to a different calibration level with an approximated backscatter decrease of 0.08 dB on average to data recorded before February 2012.

Finally, sensor intra-calibration is performed in order to achieve a consistent calibration level continuously for each European scatterometer mission. Global scatterometer observation $\sigma^0\left(L, t_i, \theta, \phi_j\right)$ are correct with the corresponding intra-calibration coefficient $\overline{C_{IAS}}\left(t_i, \theta, \phi_j\right)$, as discussed in chapter 4.5, relative to the determined calibration reference of the scatterometer. As a result, the detected calibration anomalies, like individual antenna beam drifts or variations, are supposed to be removed as well as the observed inter-beam biases.

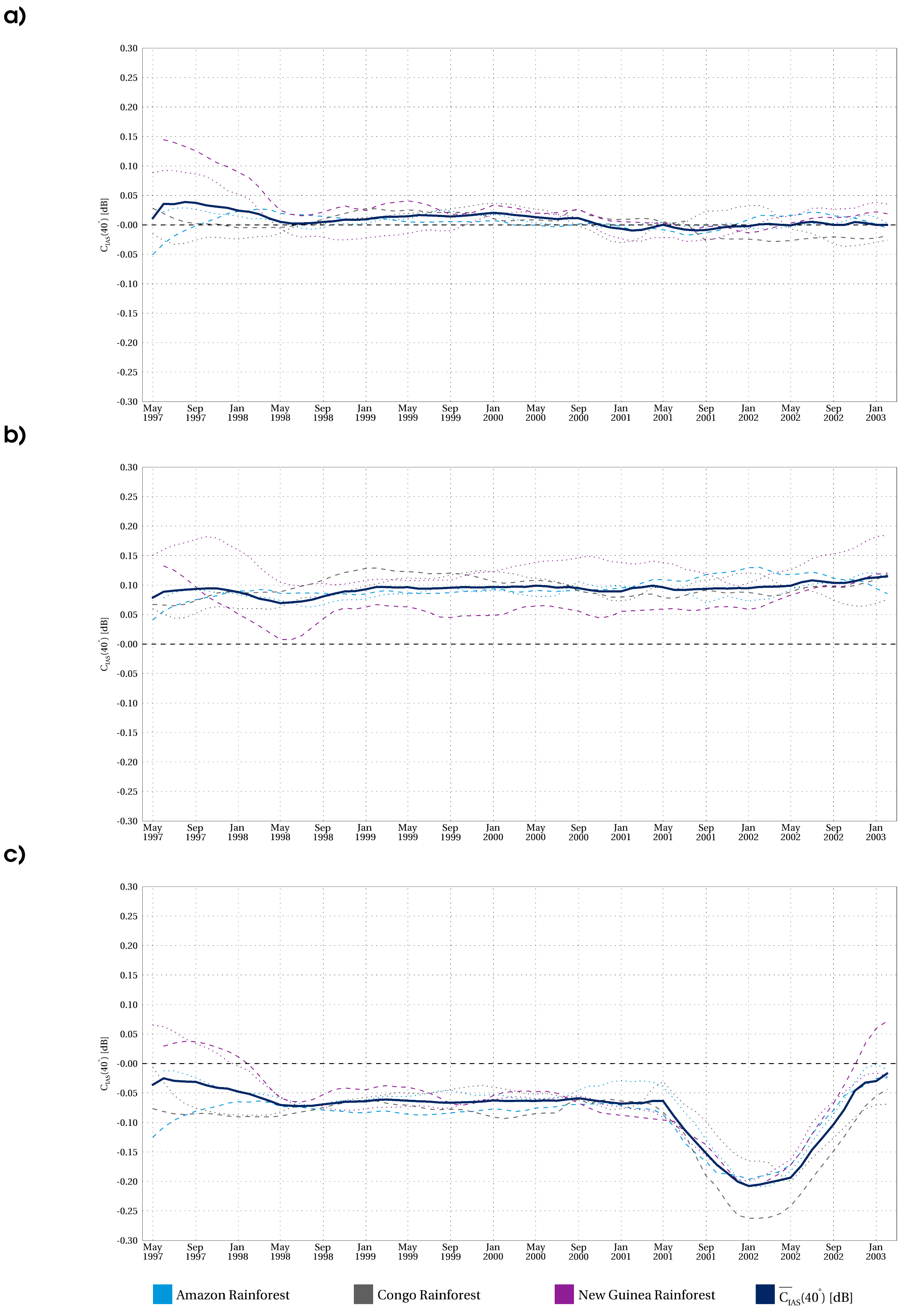

Figure 5.10: Temporal evolution of the intra-calibration coefficient $\overline{C_{IAS}}(40°)$ [solid dark blue line] determined for AMI-WS a) Fore-beam b) Mid-beam c) Aft-beam antenna. Estimates of the coefficient per calibration targets are depicted separately for ascending [dotted line] and descending overpass [dashed line].

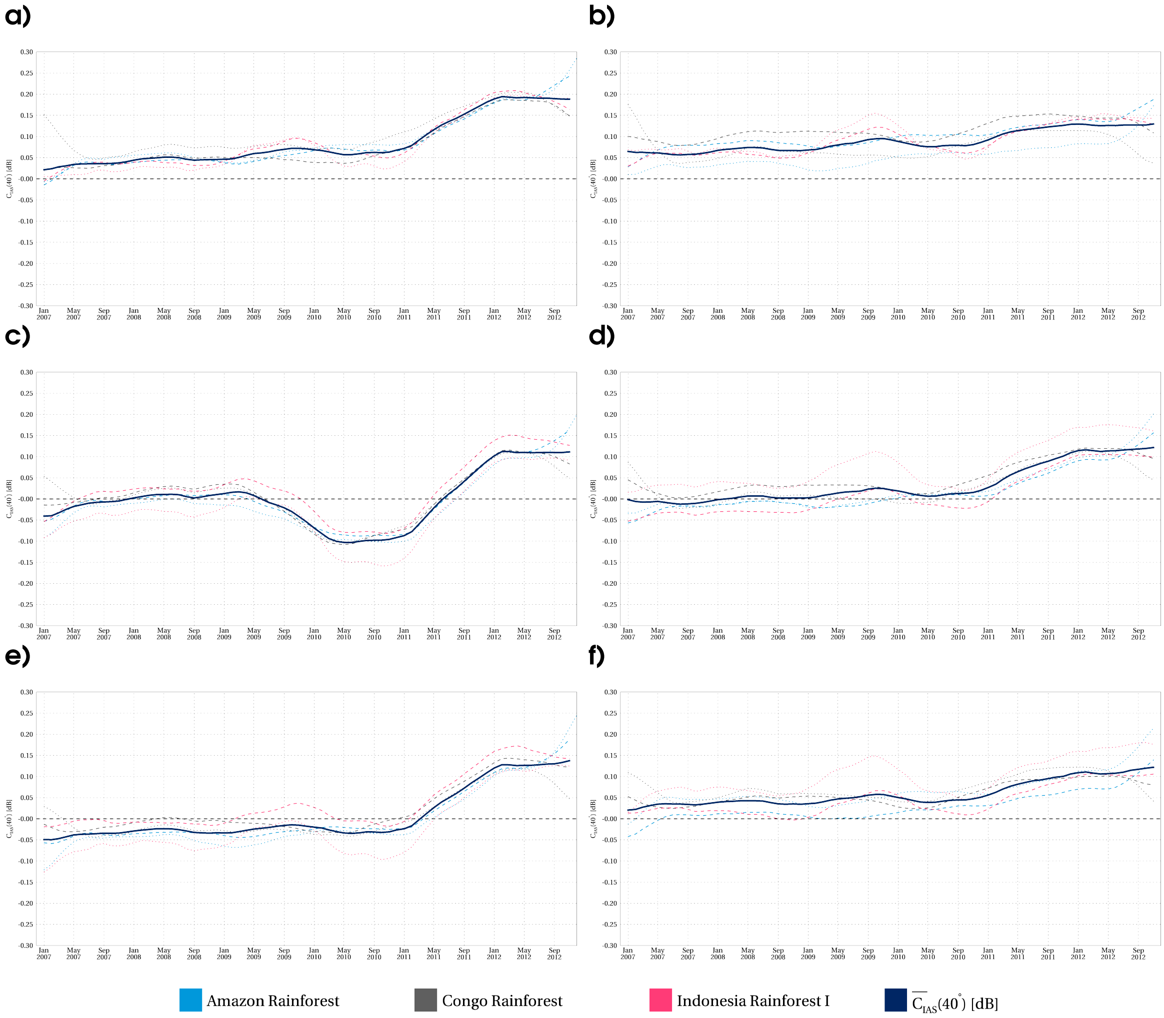

Figure 5.11: Temporal evolution of the intra-calibration coefficient $\overline{C_{IAS}}(40°)$ [solid dark blue line] determined for ASCAT a) Left b) Right Fore-beam c) Left d) Right Mid-beam e) Left f) Right Aft-beam antenna. Estimates of the coefficient per calibration targets are depicted separately for ascending [dotted line] and descending overpass [dashed line].

5.4.3 Verification of AMI-WS and ASCAT Intra-Calibration

Sensor intra-calibration coefficients $\overline{C_{IAS}}\left(t_i,\theta,\phi_j\right)$ are determined by means of three selected calibration targets. With regard to this analysis, global backscatter coefficients $\sigma^0\left(L,t_i,\theta,\phi_j\right)$ are adjusted to compensate for the observed calibration anomalies degrading the accuracy of the normalised radar cross section. Thus, the intra-calibrated scatterometer datasets have to be verified in order to confirm the successful elimination of the observed calibration anomalies. Verification of the data is performed on a set of independent calibration targets, by additionally applying the developed intra-calibration methodology, separately for AMI-WS and ASCAT. A successful intra-calibration of the individual scatterometer datasets is found if the newly computed intra-calibration coefficients of the independent calibration targets reveal hardly any deviations to the calibration reference. Results of this verification are illustrated in figure 5.12 for AMI-WS data verification and in figure 5.13 with respect to ASCAT. It should be noted that, verification targets are assumed to be characterised by identical backscatter characteristics as the employed calibration targets. Statistics of the verification targets, given in chapter 5.3, depict the applicability of the targets for calibration purposes, but also remark losses in the determination accuracy of intra-calibration coefficients, due to remaining unpredictable target variations. Therefore, estimated intra-calibration coefficients before (dashed lines) and after (solid lines) applying the sensor intra-calibration are illustrated in figures 5.12 and 5.13 for each verification target. Intra-calibration coefficients determined before the calibration was applied are hereafter referred to as initial intra-calibration coefficients and coefficients determined after calibration are referred to as verification coefficients.

Selected verification targets to prove intra-calibration results of AMI-WS are Indonesia Rainforest (I + II), Upper Guinean Forest and Malaysian Rainforest. Verification targets do indicate the successful elimination of the observed calibration anomalies. Especially for the Aft-beam antenna of AMI-WS (see figure 5.12c), an improved calibration result is apparently over the entire period, but particularly for measurement between May 2001 and January 2002. On the other hand, the verification of the Fore-beam antenna, see figure 5.12a, point out that the initial determined calibration anomalies found for the verification targets differ from those computed by the employed calibration targets (see figure 5.10a). As a consequence, verification coefficients indicate slightly increased calibration anomalies for the intra-calibrated normalised radar cross section of the verification targets. One reason for the found discrepancies might be the higher temporal backscatter variability exhibited by the verification targets in comparison to the utilised calibration targets (see table 5.4). Furthermore, a higher variance is obvious in the individual determined intra-calibration coefficients of the verification targets compared to the explored variance of the calibration targets. An equivalent conclusion can be drawn with respect to the verification result observed for the Mid-beam antenna of AMI-WS. In table 5.6 a measure to quantitatively verify the discovered results of the introduced intra-calibration is tabulated, to underpin the drawn statements and highlight the success of the method, despite of the found discrepancies in the verifica-

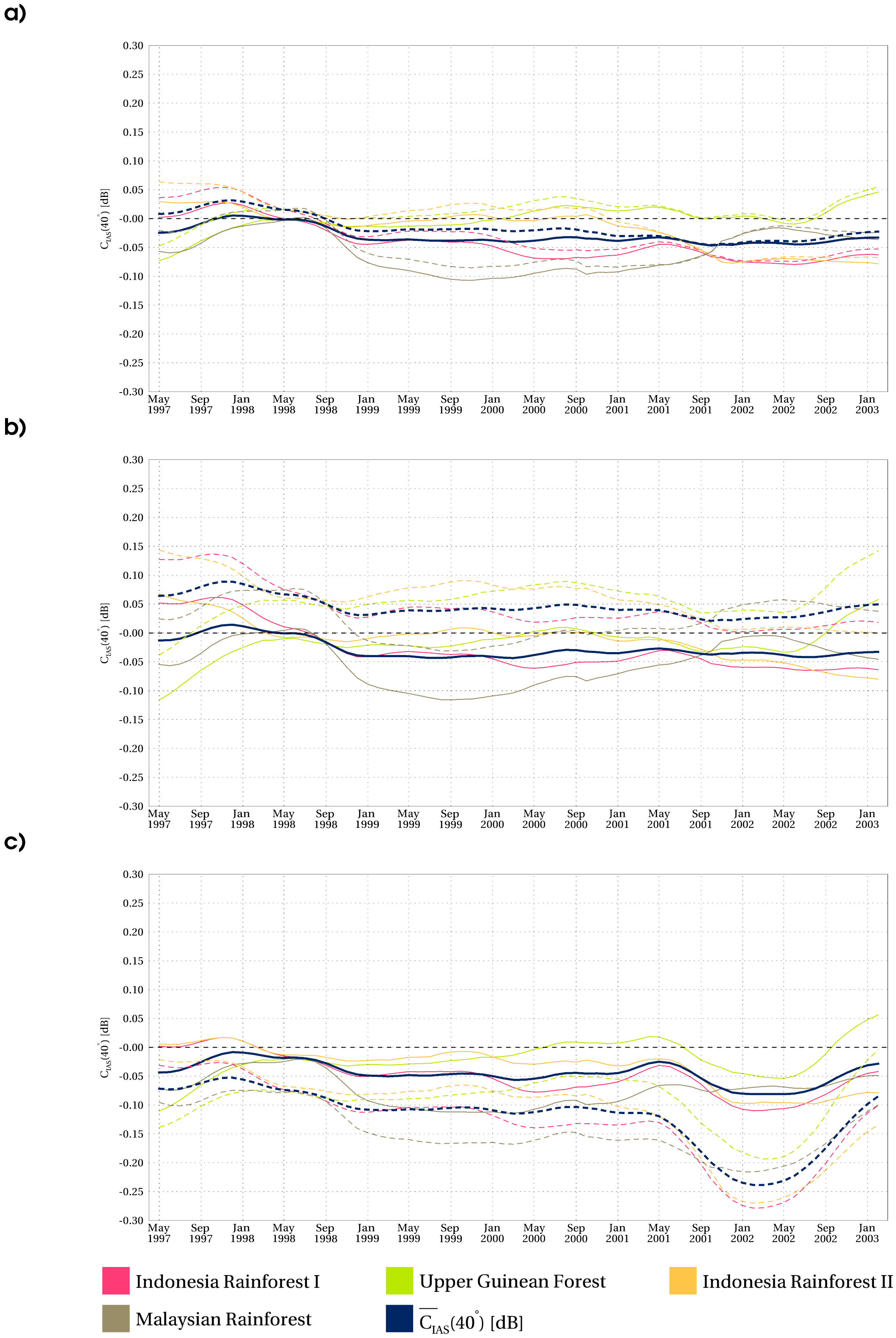

Figure 5.12: Results of sensor intra-calibration verification of AMI-WS performed on independent calibration targets. Initial intra-calibration coefficients are illustrated as dash lines and verification coefficients are illustrated as solid lines. a) Fore-beam b) Mid-beam c) Aft-beam antenna.

	RMS$\left(\overline{C_{IAS}}(t_i,\theta,\phi)\right)$ [dB]			
	AMI-WS		ASCAT	
Antenna Beam	un-calibrated	calibrated	un-calibrated	calibrated
Right Fore Beam	0.027	0.034	0.063	0.014
Left Fore Beam	-	-	0.076	0.014
Right Mid Beam	0.049	0.032	0.047	0.019
Left Mid Beam	-	-	0.058	0.017
Right Aft Beam	0.131	0.048	0.042	0.016
Left Aft Beam	-	-	0.041	0.013

Table 5.6: Root mean square of intra-calibration coefficients determined for the verification of AMI-WS and ASCAT sensor intra-calibration.

tion of the Fore- and Mid-beam antenna of AMI-WS. A useful measure to investigate the results of the intra-calibration process is gained by the root mean square of the initial and the verification intra-calibration coefficients. Values of this measure are provided in table 5.6, show that calibration anomalies observed for AMI-WS are successfully minimised by comparing the root mean square of the initial and the verified calibration results.

Verification targets selected for ASCAT are Upper Guinean Forest, Indonesia Rainforest II, Malaysian and Laos Rainforest. Initial intra-calibration coefficients of the verification targets, illustrated in figure 5.13, agreeing well with the calibration anomalies found by the employed calibration targets (see figure 5.11). Furthermore, intra-calibration coefficients calculated for verification highlight the success of the intra-calibration process in terms of ASCAT. The calibration anomaly observed for all ASCAT antennas after January 2011 is successfully minimised and additionally all antenna beams are closely aligned to the defined calibration reference. Moreover, the calibration anomaly in the period from September 2009 to January 2011, examined for the left swath Mid-beam antenna (see 5.13c), could also be eliminated with the developed intra-calibration method showing excellence accordance to the verification calibration reference. In addition, a consistent temporal behaviour of the verification coefficients of all ASCAT antennas should be highlighted, which is quantitatively confirmed by the provided root mean square values given in table 5.6. Root mean square values of residual calibration anomalies after intra-calibration of the dataset are in the range of 0.013 to 0.019 dB, while values are ranging from 0.041 - 0.076 dB before sensor intra-calibration was applied.

5.5 Inter-Calibration of ERS-2 AMI-WS and MetOp-A ASCAT

Inter-calibration of AMI-WS and ASCAT onboard of ERS-2 and MetOp-A respectively, is performed by means of already intra-calibrated scatterometer datasets, utilising coexisting calibration tar-

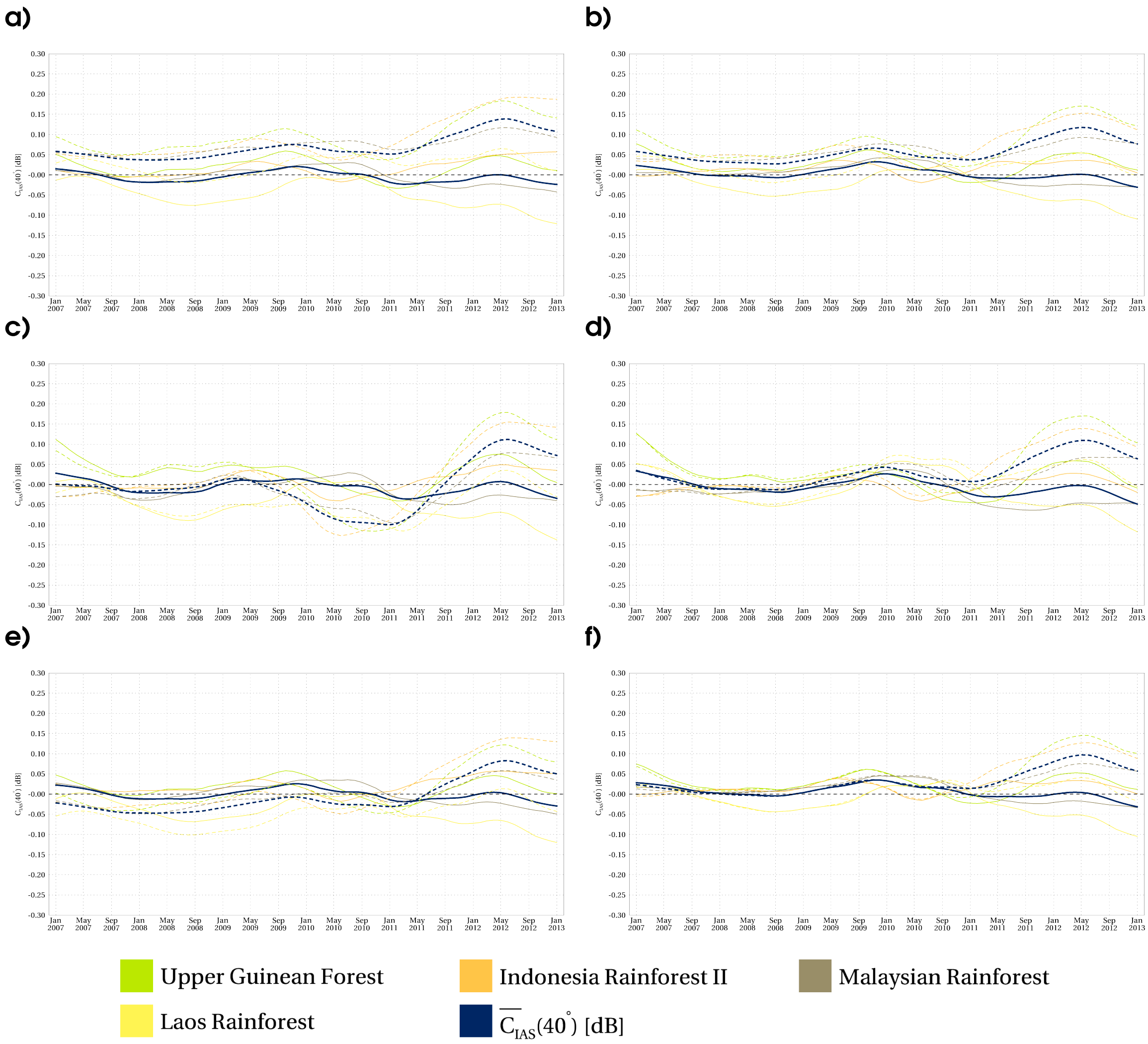

Figure 5.13: Results of sensor intra-calibration verification of ASCAT performed on independent calibration targets. Initial intra-calibration coefficients are illustrated as dash lines and verification coefficients are illustrated as solid lines. a) Left b) Right Fore-beam c) Left d) Right Mid-beam e) Left f) Right Aft-beam antenna.

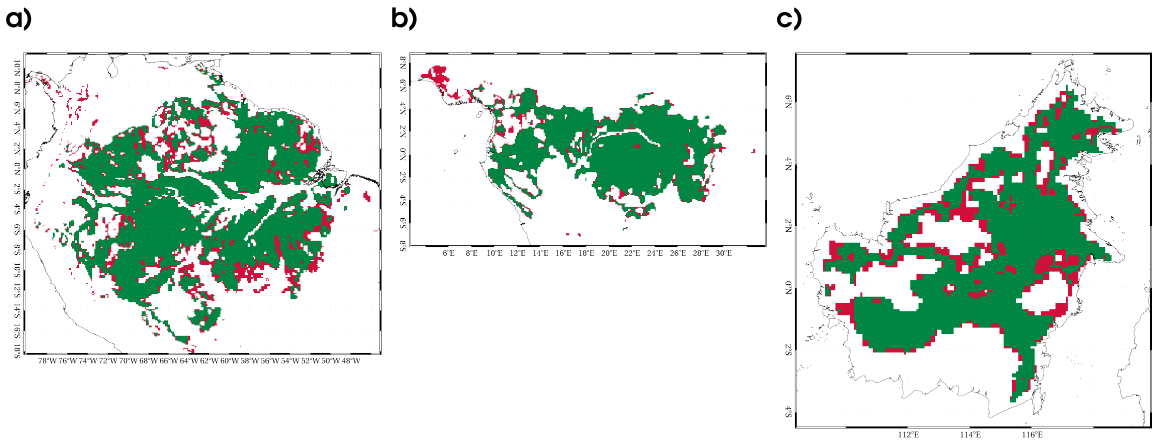

Figure 5.14: Differences in the spatial extend [red areas] of coexisting AMI-WS and ASCAT calibration targets. a) Amazon Rainforest b) Congo Rainforest c) Indonesia Rainforest I

gets. Hence, the developed inter-calibration methodology is referred to as a stepwise calibration approach. The consecutively execution of scatterometer calibration has the advantage that temporal emerging calibration anomalies of AMI-WS or ASCAT can be neglected for sensor inter-calibration. After the individually applied sensor intra-calibration, AMI-WS and ASCAT are considered to be calibrated to consistent - but differing - calibration levels determined for each instrument. Accordingly, a time invariant inter-calibration coefficient $\widetilde{C_{IES}}(\theta, \phi_j)$ is postulated, reflecting possible biases between the calibration levels of the two scatterometer missions. It is worthwhile to mention that sensor inter-calibration of AMI-WS and ASCAT is practicable, although the datasets of the considered scatterometer mission do not overlap in time. The feasibility is manifested in the long-term backscatter stability, already proven in chapter 5.3.3.2, of the coincident extended area land-targets utilised for radiometric calibration. Differences in the normalised radar cross section observed for AMI-WS and ASCAT are considered to express biases in the actual calibration levels of these scatterometer missions. Similar to sensor intra-calibration, extended area land-targets are classified into calibration targets, used to infer potential biases between the two scatterometer missions, and verification targets to confirm the applied inter-calibration methodology. Natural targets selected for inter-calibration purposes are Amazon Rainforest, Congo Rainforest and Indonesia Rainforest I. Consequently, Upper Guinean Rainforest, Indonesia Rainforest II and Malaysian Rainforest serve as verification targets respectively. It should be noted, that the selected calibration and verification targets of AMI-WS and ASCAT reveal differences in the spatial extent over time, possibly caused by deforestation, as can be seen in figure 5.14. However, the found spatial variations of the calibration targets are neglected for inter-calibration, incorporating the entire dataset of the individually derived calibration targets of AMI-WS and ASCAT.

			$\overline{C_{IES}}(\theta)$	
Antenna Beam	C_0 [dB]	C_1 [dB/deg]	min(θ) [dB]	max(θ) [dB]
Right Fore Beam	0.158	-0.012	0.384	-0.068
Right Mid Beam	0.194	-0.006	0.332	0.156
Right Aft Beam	0.155	-0.012	0.390	-0.08

Table 5.7: Inter-calibration coefficients determined for AMI-WS with respect to ASCAT represented by 1-order-polynomial coefficients.

5.5.1 Estimation of Inter-Calibration Coefficients for AMI-WS and ASCAT

ASCAT onboard of MetOp-A is the most recent operational scatterometer mission of the investigated datasets, while AMI-WS onboard of ERS-2 is already decommissioned. Therefore, the intention is to inter-calibrate AMI-WS onboard of ERS-2 with respect to ASCAT. Following the theoretical baseline of the developed inter-calibration methodology, see chapter 4.6, calibration references of the coincident calibration targets of ASCAT serve as the defined master calibration level denoted by $\overline{\sigma^0_{ASCAT}}(L_T,\theta)$. The employed calibration references are determined separately for each satellite overpass and are a function of the incidence angle θ exclusively. Furthermore, ASCAT calibration references incorporate measurements of left and right swath antenna beams, while AMI-WS is equipped with a single swath configuration of three antenna beams. Due to the assumption of an azimuthal isotropic backscatter behaviour of the utilised calibration targets, a one-to-one comparison of corresponding antenna beams is not essential. Therefore, sensor inter-calibration coefficients $C_{IES}(L_T,t_i,\theta,\phi_j)$ disclosing sensor related biases between AMI-WS and ASCAT are investigated by using equation 5.27 for each individual antenna beam of AMI-WS separately.

$$C_{IES}(L_T,t_i,\theta,\phi_j) = \widetilde{C_{IES}}(L_T,\theta,\phi_j) + \epsilon = \overline{\sigma^0_{ASCAT}}(L_T,\theta) - \sigma^0_{AMI}(L_T,t_i,\theta,\phi_j)\ . \tag{5.27}$$

Backscatter observations of AMI-WS, $\sigma^0_{AMI}(L_T,t_i,\theta,\phi_j)$, are corrected for the perceived seasonality exhibited by the calibration targets. Estimates of the inter-calibration coefficient C_{IES} are derived for each observation recorded by AMI-WS at the corresponding coincident calibration target, neglecting the actual measurement time t_i. Equivalently to the predication of sensor intra-calibration coefficients, the computed estimates $C_{IES}(L_T,\theta,\phi_j)$ are averaged over the number of calibration targets n_{TAR}, separately for the individual antenna beams of AMI-WS, represented by the function argument ϕ_j.

$$\overline{C_{IES}}(\theta,\phi_j) = \frac{1}{n_{TAR}n}\sum_{T=1}^{n_{TAR}}\sum_{i=1}^{n} C_{IES}(L_T,t_i,\theta,\phi_j) = C_0(40^\circ) + C_1(40^\circ) * (\theta - 40^\circ) \tag{5.28}$$

During the computation of the estimates C_{IES} of the inter-calibration coefficient for the individual targets, a linear relationship of the coefficient with the incidence angle θ was discovered. Accordingly, the inter-calibration coefficient $\overline{C_{IES}}(\theta, \phi_j)$ of each antenna beam is intended to be modelled as a 1-order polynomial function with respect to the incidence angle θ. Polynomial coefficients C_0 and C_1 are determined by an ordinary least square fit, incorporating the computed estimates C_{IES} of all utilised calibration targets. As a result, the derived linear model parameters, listed in table 5.7, represent the inter-calibration coefficient $\overline{C_{IES}}(\theta, \phi_j)$ as continuous function of the incidence angle θ for each AMI-WS antenna beam. The predicted inter-calibration coefficients $\overline{C_{IES}}(\theta, \phi_j)$ are illustrated in figure 5.15 for the individual antenna beams, accompanied by a data density plot of the investigated estimates, depicting the explored linear relation of C_{IES} with incidence angle θ. It should be noted that positive values of the inter-calibration coefficient $\overline{C_{IES}}$ indicate a lower AMI-WS backscatter coefficient at the incidence angle θ in comparison to the ASCAT normalised radar cross section and for negative values of $\overline{C_{IES}}$ vice versa. Inter-calibration coefficients found for the Fore- and Aft-beam antenna of AMI-WS reveal almost identical biases to the calibration reference of ASCAT, as can be seen in the determined model coefficients given in table 5.7. The inter-calibration coefficient at 40 degrees incidence angle $\overline{C_{IES}}(40°)$ of the Mid-beam antenna indicate a marginal higher bias, in the order of 0.038 dB, with respect to the coefficients of the Fore- and Aft-beam antennas. Furthermore, inter-calibration coefficients of the Mid-beam antenna solely displays positive coefficients across the analysed incidence angle range, highlighting lower backscatter values observed by AMI-WS. Values of the Mid-beam inter-calibration coefficient are ranging from 0.332 dB to 0.156 dB. But in terms of the Fore- and Aft-beam coefficients, negative values are apparent for incidence angles greater than 52 degrees, indicating lower backscatter values for ASCAT. Sensor inter-calibration coefficients of the Fore- and Aft-beam antenna are in the range of 0.39 dB to -0.08 dB as listed in table 5.7. With reference to the determined inter-calibration coefficient $\overline{C_{IES}}(\theta, \phi_j)$, backscatter observations of AMI-WS are rectified to account for the discovered antenna beam biases given by equation 4.18, resulting in a long-term consistent European scatterometer data archive. Nonetheless, the effective adjustment of the observed backscatter discrepancies between AMI-WS and ASCAT antenna beams need to be verified by means of the independent verification targets.

5.5.2 Verification of Sensor Inter-Calibration

Already intra-calibrated AMI-WS backscatter observations were corrected for the observed antenna biases by utilising the determined inter-calibration coefficients $\overline{C_{IES}}(\theta, \phi_j)$ and equation 4.18. The objective of the verification process is to confirm the effective adjustment of AMI-WS backscatter measurements with respect to the defined calibration level of ASCAT. Therefore, the sensor inter-calibration method was repeated for inter-calibrated AMI-WS data by using the selected verification targets Indonesia Rainforest (I + II), Upper Guinean Forest and Malaysian Rainforest. In the case of a perfect rectification of the observed antenna beam biases, inter-calibration

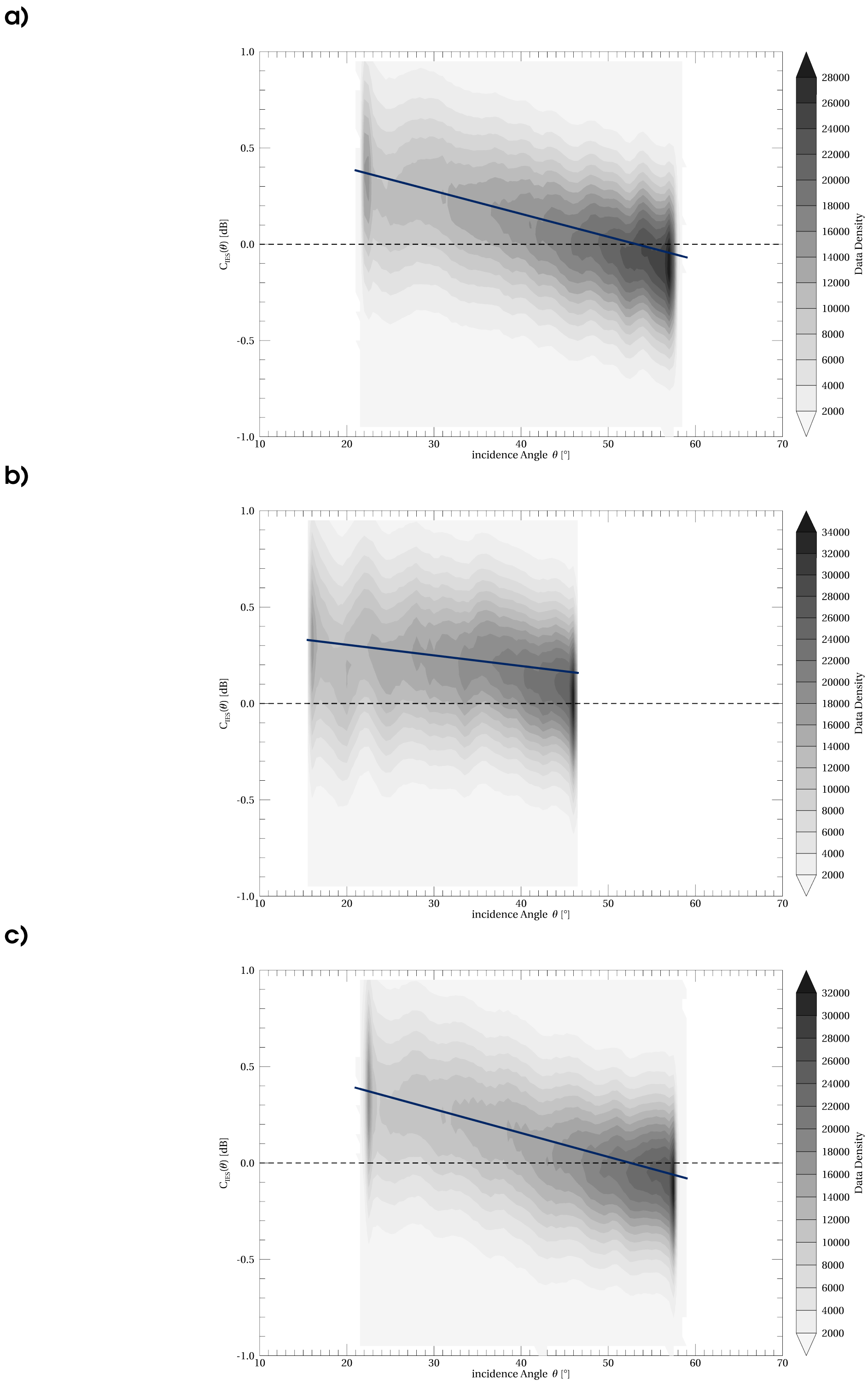

Figure 5.15: Inter-calibration coefficients [solid dark blue line] estimated for AMI-WS with respect to ASCAT by utilising coincident calibration targets. Underlying data density plot depict the amount of data used to determine the coefficients. a) Fore-beam b) Mid-beam c) Aft-beam

		$\overline{C_{IES}}(\theta)$ [dB]		
Antenna Beam	C_0 [dB]	C_1 [dB/deg]	min(θ) [dB]	max(θ) [dB]
Right Fore Beam	-0.011	-0.002	-0.040	0.019
Right Mid Beam	-0.024	-0.003	-0.042	0.040
Right Aft Beam	-0.019	-0.002	-0.048	0.011

Table 5.8: Verification results of the sensor inter-calibration applied to AMI-WS represented by 1-order-polynomial coefficients.

coefficients derived for verification, represented by the 1-order-polynomial parameter C_0 and C_1, become equal null. Figure 5.16 illustrates the predicted inter-calibration coefficients of each AMI-WS antenna beam, estimated during the verification process. As can be seen, the explored antenna beam biases between AMI-WS and ASCAT are eliminated successfully by making use of the introduced sensor inter-calibration approach. Residual antenna beam biases revealed by the verification targets are ranging from 0.04 dB to -0.048 dB, see table 5.8, with respect to the minimum and maximum incidence angles of the antenna beams. Moreover, the determined antenna beam biases at 40 degrees incidence angle, represented by the model parameter C_0, could be aligned to the defined calibration reference with deviations of less than 0.025 dB. In addition, the backscatter versus incidence angle dependency of AMI-WS could be matched to those of ASCAT, highlighted by insignificantly small values of the model parameter C_1. In summary, the introduced stepwise inter-calibration methodology is capable to successfully expose and correct for possible antenna beam biases, paving the way towards a long-term consistent European scatterometer data archive incorporating AMI-WS and ASCAT backscatter observations.

a)

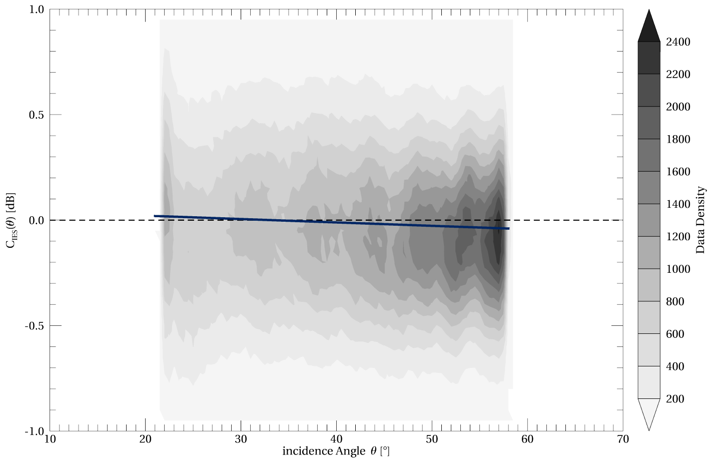

b)

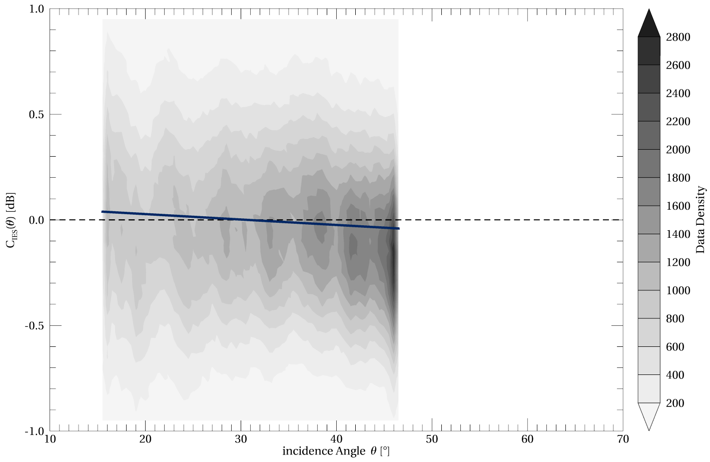

c)

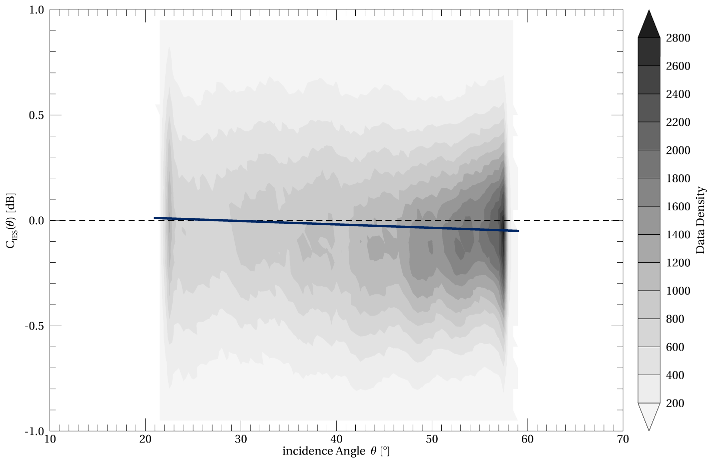

Figure 5.16: Verification of inter-calibration coefficients [solid dark blue line] estimated for AMI-WS with respect to ASCAT by utilising coincident verification targets. Underlying data density plot reflect the amount of data used to determine the coefficients. a) Fore-beam b) Mid-beam c) Aft-beam

Chapter 6

Conclusion and Outlook

In the present work a novel relative calibration methodology for C-band fan-beam scatterometers was introduced. Relative calibration of scatterometers is performed since the early stages of space-borne scatterometry. Nevertheless, the proposed calibration methodology is innovative with respect to the incorporation of a set of calibration targets for the determination and verification of calibration parameters. The major benefit of using a number of diverse calibration targets is to discriminate between residual variations exhibited by single calibration targets and pure calibration anomalies of the investigated scatterometer in space. In general, backscatter characteristics of the utilised natural calibration targets have to be examined thoroughly, especially with respect to the long-term backscatter stability of the extended area land-targets, which is fundamental for the accomplishment of relative calibration. In the preparation phase of this study the importance of in-depth analysis of backscatter characteristics of the exploit calibration targets was noticed. These analysis pointed out that initially selected ASCAT calibration targets Caatinga-Brazil, Southeastern USA Plains, Somalia, Gran Chaco, Central America Rainforest and Western-Australia, do not fully comply with the required criteria to determine calibration parameters accurately. Relaxing the required criteria for the selection of applicable extend area calibration targets, with regard to the requirement of azimuthal isotropic backscatter, would be advisable to incorporate these moderate to sparsely vegetated targets. In addition, discarding the requirement of azimuthal isotropic backscatter may benefit in making use of further potential calibration targets, already investigated in several studies [*Kunz and Long*, 2005; *Moon and Long*, 2013], such as the Greenland and Antarctic ice sheets and the Sahara desert.

The defined calibration references used for sensor intra- and inter-calibration are determined by taking advantage of recorded backscatter measurements covering a complete year of data. Moreover, the calibration reference was found by assuming a perfectly calibrated instrument for the time being. The considered data period for the determination of the calibration reference have to be chosen carefully, because neglected calibration anomalies in the period will affect the overall calibration level. As a consequence, artificial biases will be induced in the monitored calibration anomalies over time and in the temporal invariant inter-calibration coefficients. Calibration anomalies, inferred throughout intra- and inter-calibration, are modelled as continuous functions of the incidence angle within this study. The examined 1-order polynomial functions are not capable to describe calibration deficiencies at specific incidence angles, but are applicable to correct for possible biases and first-order deviations of backscatter versus incidence angle behaviour. The developed calibration methodology is a simple and obvious approach to monitor and correct for residual calibration artefacts of scatterometer missions. Monitored calibration deficiencies are found to correspond to main mission events or on-ground processor updates, which have been successfully removed with the developed calibration methodology and have been verified by the use of independent verification targets. In addition, the introduced calibration methodology should be capable of incorporating calibration parameters of different calibration approaches like ocean calibration, sea ice calibration or calibration using co-located backscatter observation by simply extending the number of calibration targets for a robust detection and correction of calibration deficiencies. [*Anderson et al.*, 2012; *Crapolicchio et al.*, 2012; *Stoffelen*, 1999].

The ultimate aim of the developed calibration methodology is to derive a long-term consistent scatterometer data archive for global surface soil moisture (SSM) retrieval. The SSM retrieval model developed at Vienna University of Technology (TU-Wien) is designed as a change detection algorithm for C-band fan-beam scatterometer observations. A detailed description of the TU-Wien SSM retrieval algorithm is beyond the scope of this work, but details about the current implementation, the so-called WAter Retrieval Package (WARP), can be found in *Bartalis et al.* [2007]; *Naeimi et al.* [2009]; *Wagner et al.* [1999a,b,c]. Nevertheless, implications of the introduced scatterometer calibration methodology on the SSM retrieval algorithm will be discussed briefly and very general.

The TU-Wien surface soil moisture retrieval algorithm is based on a set of model parameters, determined by temporal analysis of long-term backscatter time series, characterising spatial variations in land cover, surface roughness and many other effects controlling the backscatter coefficient σ^0. Furthermore, model parameters are determined by making use of the multi-beam observation capability of fan-beam scatterometers. As a consequence, calibration anomalies discovered in one or more antenna beams will affect the model parameter determination by degrading the parameter accuracy. For example, a noise estimate of the backscatter coefficient σ^0 is calculated as the standard deviation of Fore-/ Aft-beam observation differences. Unaccounted calibration anomalies exposed in these antenna beams will therefore contribute artificial backscatter noise to this model parameter, which will be propagated to the final SSM noise estimate. As a result of sensor intra-calibration, a more accurate backscatter noise estimate, referred to as Estimated Standard Deviation (ESD), is derived by means of a successful elimination of residual calibration deficiencies. Additionally, the predication of the key parameters of the TU-Wien surface soil moisture retrieval model, referred to as Slope and Curvature, employ observations of the Fore-, Mid- and Aft-beam antenna simultaneously over time. Hence, the model parameters Slope and Curvature are sensitive to calibration anomalies of any antenna beam over time. Especially observed calibration deficiencies in the Mid-beam antenna are important for an accurate estimation of these SSM model parameters, because of the followed determination procedure. The model parameters Slope and Curvature are exploit to express the backscatter coefficient σ^0 as a function of the incidence angle θ, developed as a 2-order polynomial function centred at a reference incidence angle of 40 degrees. Moreover, the temporal evolution of the Slope model parameter is supposed to depict vegetation phenology, which needs to be considered in the SSM retrieval, to highlight the importance of an accurate parameter determination.

The advantage of the TU-Wien algorithm is a direct SSM retrieval from scatterometer measurements, utilising the pre-computed model parameters. As a result, possible calibration deficiencies of individual antenna beams have an impact on the model parameter estimation and furthermore are directly transferred to the retrieved SSM values. However, further studies need to be conducted to quantify all implications of the introduced calibration methodology on the SSM retrieval algorithm rigorously. A first impression of the implications of the introduced calibration methodology is given in figure 6.1, which illustrates daily global surface soil moisture anomalies computed from MetOp-A ASCAT retrievals. The graph displays SSM anomalies before (black) and after (blue) sensor intra-calibration was applied to the data. The implication of sensor intra-calibration is obvious, particularly for SSM anomalies after September 2011. SSM anomalies in this period highlight the importance of a well calibrated instrument in terms of climate change research. If sensor intra-calibration of ASCAT is neglected, one may come to the conclusion that the global climate changed dramatically after September 2011, revealed by a sudden break of the SSM anomalies to very dry soil moisture conditions. But the very dry soil moisture conditions turned out to be caused by varying sensor characteristics rather than a real climate change after September 2011, by focusing on the global anomalies derived from intra-calibrated scatterometer data (blue line). The cause of this sensor related deficiency was already discovered in the intra-calibration of ASCAT discussed in chapter 5.4.

Aforementioned implications on the SSM retrieval concentrated on possible calibration deficiencies of individual scatterometer missions monitored throughout sensor intra-calibration. But advantages of the proposed inter-calibration methodology were disregarded so far. Sensor inter-calibration accomplish a common calibration level between two or more scatterometers, so that backscatter observations of individual missions can be regarded equivalently. With respect to the derivation of model parameters used for SSM retrieval, long-term backscatter observations are envisaged for a precise determination of the different contributions affecting the backscatter coefficient σ^0. Hence, sensor inter-calibrated data of AMI-WS and ASCAT, for example, could be used to infer a single set of consistent model parameters for SSM retrieval by incorporating these scatterometer missions. The combined use of AMI-WS and ASCAT backscatter observations for

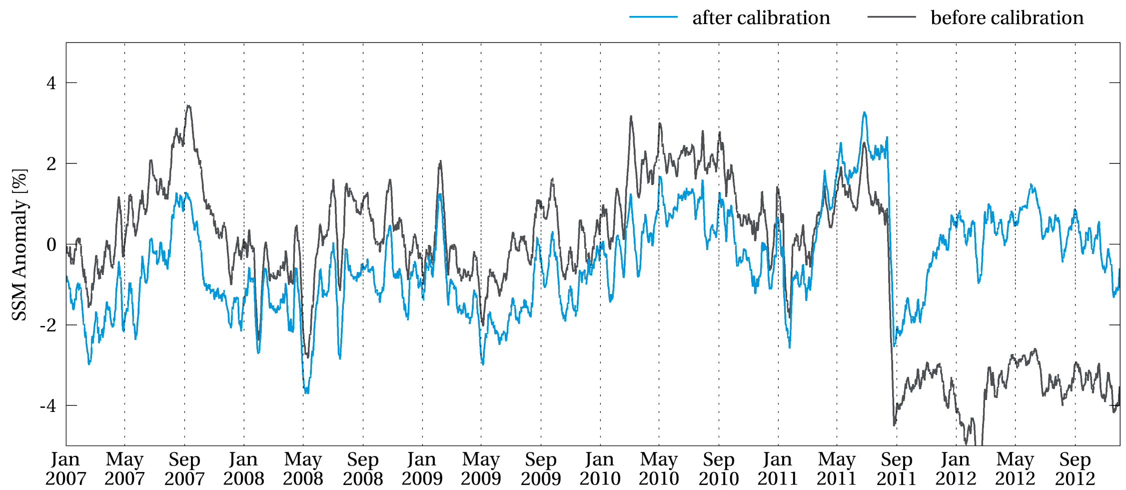

Figure 6.1: Global surface soil moisture anomalies before and after sensor intra-calibration of ASCAT.

SSM retrieval is aspired for generating a surface soil moisture Essential Climate Variable (ECV). Current efforts undertaken to merge SSM retrievals of these scatterometer mission are focusing on a statistical matching of the retrieved soil moisture values known as Cumulative Distribution Function (CDF) matching [*Liu et al.*, 2012, 2011]. Thus, the developed inter-calibration strategy is a great opportunity to merged these scatterometer datasets on a backscatter coefficient level, for a consistent computation of a surface soil moisture ECV by the use of a single set of model parameters and inter-calibrated scatterometer observations. Furthermore, ASCAT is foreseen as a multi-mission instrument onboard of a series of three MetOp satellites. Consequently, the developed inter-calibration method can be employed to discover and correct for sensor related differences of ASCAT onboard of the individual satellites, with the objective to retrieve a consistent calibrated multi-mission ASCAT surface soil moisture product. A combine use of MetOp-A and MetOp-B ASCAT backscatter observations for SSM retrieval is already planned to be performed with the TU-Wien algorithm.

The introduced calibration methodology was specifically developed with respect to C-band fan-beam scatterometers. Though, the calibration procedure may be capable of cross-calibrating scatterometer and Synthetic Aperture Radar (SAR) instruments too. A radiometric cross-calibration of these active microwave instruments is feasible because European scatterometer and SAR instruments operate at almost identical frequencies in the C-band. Additionally, the production of a high resolution SSM product derived from SAR observations will benefit from the radiometric cross-calibration of scatterometers and SARs [*Pathe et al.*, 2009].

Bibliography

Anderson, C., J. Figa, H. Bonekamp, J. J. W. Wilson, J. Verspeek, A. Stoffelen, and M. Portabella (2012), Validation of backscatter measurements from the advanced scatterometer on MetOp-A, *J. Atmos. Oceanic Technol.*, **29**(1), p. 77–88, doi:10.1175/JTECH-D-11-00020.1.

Attema, E. (1991), The Active Microwave Instrument on-board the ERS-1 satellite, *Proceedings of the IEEE*, **79**(6), p. 791 –799, doi:10.1109/5.90158.

Bartalis, Z. (2009a), Spaceborne scatterometers for change detection over land, Ph.D. thesis, Technische Universität Wien, Vienna.

Bartalis, Z. (2009b), ERS-ASCAT backscatter and soil moisture intercomparison - first results., *Working Note 6*, Institute of Photogrammetry and Remote Sensing, Vienna University of Technology, Vienna.

Bartalis, Z., K. Scipal, and W. Wagner (2006), Azimuthal anisotropy of scatterometer measurements over land, *IEEE Transactions on Geoscience and Remote Sensing*, **44**, p. 2083–2092, doi:10.1109/TGRS.2006.872084.

Bartalis, Z., W. Wagner, V. Naeimi, S. Hasenauer, K. Scipal, H. Bonekamp, J. Figa, and C. Anderson (2007), Initial soil moisture retrievals from the METOP-A advanced scatterometer (ASCAT), *Geophysical Research Letters*, **34**(20), doi:10.1029/2007GL031088.

Bennett, V., and S. James (2013), Guidelines for data producers - climate change initiative phase 1, *Technical Note CCI-PRGM-EOPS-TN-11-0003.*

Birrer, I. J., E. M. Bracalente, G. J. Dome, J. Sweet, and G. Berthold (1982), Sigma-0 Signature of the Amazon Rain Forest Obtained from the Seasat Scatterometer, *IEEE Transactions on Geoscience and Remote Sensing*, **20**(1), p. 11–17, doi:10.1109/TGRS.1982.4307513.

Burnham, K. P., and D. R. Anderson (2002), *Model selection and Multimodel Inference: A practical information-theoretic approach*, 2nd ed., Springer.

Chander, G., T. J. Hewison, N. Fox, X. Wu, X. Xiong, and W. J. Blackwell (2013), Overview of intercalibration of satellite instruments, *IEEE Transactions on Geoscience and Remote Sensing*, **51**(3), p. 1056–1080, doi:10.1109/TGRS.2012.2228654.

Cheng, Y. (1995), Mean shift, mode seeking, and clustering, *IEEE Transactions on Pattern Analysis and Machine Intelligence*, **17**(8), p. 790–799, doi:10.1109/34.400568.

Comaniciu, D., and P. Meer (2002), Mean shift: a robust approach toward feature space analysis, *IEEE Transactions on Pattern Analysis and Machine Intelligence*, **24**(5), p. 603–619, doi:10.1109/34.1000236.

Cowpertwait, P. S. P., and A. V. Metcalfe (2009), *Introductory time series with R*, Springer-Verlag, New York.

Crapolicchio, R. (2004), On the stability of amazon rainforest backscattering during the ERS-2 scatterometer mission lifetime, *Technical report*, ESA.

Crapolicchio, R., P. Lecomte, and X. Neyt (2005), The advanced scatterometer processing system for ERS data: Design, products and performances, in *European Space Agency, Special Publication*, p. 843–851.

Crapolicchio, R., G. De Chiara, A. Elyouncha, P. Lecomte, X. Neyt, A. Paciucci, and M. Talone (2012), ERS-2 scatterometer: Mission performances and current reprocessing achievements, *IEEE Transactions on Geoscience and Remote Sensing*, doi:10.1109/TGRS.2011.2179808.

De Chiara, G., R. Crapolicchio, and P. Lecomte (2007), ERS-1/2 scatterometer new products: mission reprocessing and data quality improvement, in *Second Space for Hydrology Workshop*.

Early, D., and D. Long (1997), Azimuthal modulation of c-band scatterometer σ^0 over southern ocean sea ice, *IEEE Transactions on Geoscience and Remote Sensing*, **35**(5), p. 1201–1209, doi:10.1109/36.628787.

Elyouncha, A., and X. Neyt (2012), A method for cross-comparison of scatterometer data using natural distributed targets: application to ERS-1 and ERS-2 data during the tandem mission, p. 85,320O–85,320O–9, doi:10.1117/12.975218.

Elyouncha, A., and X. Neyt (2013), C-band satellite scatterometer intercalibration, *IEEE Transactions on Geoscience and Remote Sensing*, **51**(3), p. 1478–1491, doi:10.1109/TGRS.2012.2217381.

ESA (2013), Earthnet Online - The ERS Missions, `https://earth.esa.int/support-docs/ers-missions/ers-missions.html`, accessed on 2013 November 9.

EUMETSAT (2013), ASCAT Product Guide, `http://oiswww.eumetsat.org/WEBOPS/eps-pg/ASCAT/ASCAT-PG-0TOC.htm`, accessed on 2013 October 26.

Figa-Saldaña, J., J. J. Wilson, E. Attema, R. Gelsthorpe, M. R. Drinkwater, and A. Stoffelen (2002), The advanced scatterometer (ASCAT) on the meteorological operational (MetOp) platform: A follow on for european wind scatterometers, *Canadian Journal of Remote Sensing*, **28**(3), p. 404–412, doi:10.5589/m02-035.

Friesen, J., S. C. Steele-Dunne, and N. van de Giesen (2012), Diurnal differences in global ERS scatterometer backscatter observations of the land surface, *IEEE Transactions on Geoscience and Remote Sensing*, **50**(7), p. 2595–2602, doi:10.1109/TGRS.2012.2193889.

Frison, P., and E. Mougin (1996), Use of ERS-1 wind scatterometer data over land surfaces, *Geoscience and Remote Sensing, IEEE Transactions on*, **34**(2), p. 550–560.

Fromberg, A. F., E. W. Pritchard, N. G. Wright, J. J. Wilson, and G. Kayal (2010), Deployment of the ASCAT calibration transponders, p. 3486–3489, IEEE, doi:10.1109/IGARSS.2010.5652493.

Fukunaga, K., and L. Hostetler (1975), The estimation of the gradient of a density function, with applications in pattern recognition, *IEEE Transactions on Information Theory*, **21**(1), p. 32–40, doi:10.1109/TIT.1975.1055330.

GCOS (2010), Implementation plan for the global observing system for climate in support of the UNFCCC, *Tech. Rep. GCOS-138 (GOOS-184, GTOS-76, WMO-TD/No. 1523)*, WMO.

Gelsthorpe, R., E. Schied, and J. Wilson (2000), ASCAT – metop's advanced scatterometer, *ESA Bulletin*, (102), p. 19–27.

GEO (2013), Group on Earth Observations, `http://www.earthobservations.org/index.shtml`, accessed on 2013 October 25.

Hastie, T., J. Friedman, and R. Tibshirani (2003), *The elements of statistical learning : data mining, inference, and prediction*, Springer, New York, NY [u.a.].

Hawkins, R., E. Attema, R. Crapolicchio, P. Lecomte, J. Closa, P. J. Meadows, and S. K. Srivastava (2000), Stability of amazon backscatter at c-band: Spaceborne results from ERS-1/2 and RADARSAT-1., in *SAR workshop : CEOS Committee on Earth Observation Satellites*, *ESA Special Publication*, vol. 450, edited by R. A. H. . L. Ouwehand, p. 99.

Hersbach, H., A. Stoffelen, and S. de Haan (2007), An improved c-band scatterometer ocean geophysical model function: CMOD5, **112**, doi:10.1029/2006JC003743.

Kennett, R., and F. Li (1989a), Seasat over-land scatterometer data. i. global overview of the ku-band backscatterer coefficients, *Geoscience and Remote Sensing, IEEE Transactions on*, **27**(5), p. 592–605.

Kennett, R., and F. Li (1989b), Seasat over-land scatterometer data. II. selection of extended area and land-target sites for the calibration of spaceborne scatterometers, *Geoscience and Remote Sensing, IEEE Transactions on*, **27**(6), p. 779–788.

Kidd, R. (2005), NWP discrete global grid systems, *ASCAT Soil Moisture Report Series*, (4).

Klaes, K. D., M. Cohen, Y. Buhler, P. Schlüssel, R. Munro, A. Engeln, E. Clérigh, H. Bonekamp, J. Ackermann, J. Schmetz, and J.-P. Luntama (2007), An introduction to the EUMETSAT polar system, *Bulletin of the American Meteorological Society*, **88**(7), p. 1085–1096, doi:10.1175/BAMS-88-7-1085.

Kramer, H. J. (2002), *Observation of the earth and its environment*, Springer, Berlin.

Kumar, R., S. A. Bhowmick, K. N. Babu, R. Nigam, and A. Sarkar (2011), Relative calibration using natural terrestrial targets: A preparation towards oceansat-2 scatterometer, *IEEE Transactions on Geoscience and Remote Sensing*, **49**, p. 2268–2273, doi:10.1109/TGRS.2010.2094196.

Kunz, L., and D. Long (2005), Calibrating SeaWinds and QuikSCAT scatterometers using natural land targets, *IEEE Geoscience and Remote Sensing Letters*, **2**, p. 182–186, doi:10.1109/LGRS.2004.842468.

Lecomte, P. (1998), ERS scatterometer instrument and the on-ground processing of its data, in *European Space Agency, (Special Publication) ESA SP*, p. 241–260, cited By (since 1996): 11.

Lecomte, P., and W. Wagner (1998), ERS wind scatterometer commissioning & in-flight calibration, *EUROPEAN SPACE AGENCY-PUBLICATIONS-ESA SP*, **424**, p. 261–270.

Liu, Y., W. Dorigo, R. Parinussa, R. de Jeu, W. Wagner, M. McCabe, J. Evans, and A. van Dijk (2012), Trend-preserving blending of passive and active microwave soil moisture retrievals, *Remote Sensing of Environment*, **123**, p. 280–297, doi:10.1016/j.rse.2012.03.014.

Liu, Y. Y., R. M. Parinussa, W. A. Dorigo, R. A. M. De Jeu, W. Wagner, A. I. J. M. van Dijk, M. F. McCabe, and J. P. Evans (2011), Developing an improved soil moisture dataset by blending passive and active microwave satellite-based retrievals, *Hydrology and Earth System Sciences*, **15**(2), p. 425–436, doi:10.5194/hess-15-425-2011.

Long, D., and M. Drinkwater (2000), Azimuth variation in microwave scatterometer and radiometer data over antarctica, *Geoscience and Remote Sensing, IEEE Transactions on*, **38**(4), p. 1857 –1870, doi:10.1109/36.851769.

Long, D. G., and G. B. Skouson (1996), Calibration of spaceborne scatterometers using tropical rain forests, *IEEE Transactions on Geoscience and Remote Sensing*, **34**(2), p. 413–424, doi:10.1109/36.485119.

Manise, N., X. Neyt, and M. Acheroy (2004), Calibration of the ERS-2 scatterometer in gyro-less mode, Salzburg, Austria.

Martin, S. (2004), *An introduction to ocean remote sensing*, Cambridge, Cambridge, UK ; New York.

Moon, K. R., and D. G. Long (2013), Considerations for ku-band scatterometer calibration using the dry-snow zone of the greenland ice sheet, *Geoscience and Remote Sensing Letters, IEEE*, **PP**(99), p. 1–6, doi:10.1109/LGRS.2013.2241012.

Naeimi, V., K. Scipal, Z. Bartalis, S. Hasenauer, and W. Wagner (2009), An improved soil moisture retrieval algorithm for ERS and METOP scatterometer observations, *IEEE Transactions on Geoscience and Remote Sensing*, **47**, p. 1999–2013, doi:10.1109/TGRS.2008.2011617.

Neyt, X., P. Pettiaux, and M. Acheroy (2002), Scatterometer ground processing review for gyro-less operations, in *Proceedings of SPIE - The International Society for Optical Engineering*, vol. 4880, p. 1–10, cited By (since 1996): 5.

Ohring, G., B. Wielicki, R. Spencer, B. Emery, and R. Datla (2005), Satellite instrument calibration for measuring global climate change: Report of a workshop, *Bulletin of the American Meteorological Society*, **86**(9), p. 1303–1313, doi:10.1175/BAMS-86-9-1303.

Pathe, C., W. Wagner, D. Sabel, M. Doubkova, and J. B. Basara (2009), Using ENVISAT ASAR global mode data for surface soil moisture retrieval over oklahoma, USA, **47**(2), p. 468–480, doi:10.1109/TGRS.2008.2004711.

Rostan, F. (2000), The calibration of the MetOp/Advanced scatterometer (ASCAT), in *Geoscience and Remote Sensing Symposium, 2000. Proceedings. IGARSS 2000. IEEE 2000 International*, vol. 5, p. 2206–2208, doi:10.1109/IGARSS.2000.858357.

Rostan, F., M. Kuntz, and S. Schutz (1999), The advanced scatterometer (ASCAT) ground processing prototype, in *Geoscience and Remote Sensing Symposium, 1999. IGARSS '99 Proceedings. IEEE 1999 International*, vol. 1, p. 224 –226 vol.1, doi:10.1109/IGARSS.1999.773454.

Spencer, M., C. Wu, and D. Long (2000), Improved resolution backscatter measurements with the SeaWinds pencil-beam scatterometer, *IEEE Transactions on Geoscience and Remote Sensing*, **38**(1), p. 89–104, doi:10.1109/36.823904.

Stoffelen, A. (1998), Scatterometry, Ph.D. thesis, University of Utrecht, Utrecht.

Stoffelen, A. (1999), A simple method for calibration of a scatterometer over the ocean, *Journal of Atmospheric and Oceanic Technology*, **16**(2), p. 275–282, doi:10.1175/1520-0426(1999)016<0275:ASMFCO>2.0.CO;2.

Ulaby, F. T., R. K. Moore, and A. K. Fung (1981), *Microwave remote sensing - Fundamentals and Radiometry*, vol. 1, Artech House, Norwood.

Ulaby, F. T., R. K. Moore, and A. K. Fung (1982), *Microwave Remote Sensing - Active and Passive*, vol. 2, Artech House, Norwood, MA.

Ulaby, F. T., R. K. Moore, and A. K. Fung (1986), *Microwave Remote Sensing - From Theory to Applications*, vol. 3, Artech House, Norwood, MA.

Vass, P., European Space Agency, Earthnet (Agency), and European Space Research Institute (1992), *ERS-1 system*, no. 1146 in ESA SP, ESA Publications Division, Noordwijk, Netherland.

Wagner, W., G. Lemoine, and H. Rott (1999a), A method for estimating soil moisture from ERS scatterometer and soil data, *Remote Sensing of Environment*, **70**(2), p. 191–207, doi:10.1016/S0034-4257(99)00036-X.

Wagner, W., G. Lemoine, M. Borgeaud, and H. Rott (1999b), A study of vegetation cover effects on ERS scatterometer data, *IEEE Transactions on Geoscience and Remote Sensing*, **37**(2), p. 938–948, doi:10.1109/36.752212.

Wagner, W., J. Noll, M. Borgeaud, and H. Rott (1999c), Monitoring soil moisture over the canadian prairies with the ERS scatterometer, *IEEE Transactions on Geoscience and Remote Sensing*, **37**(1), p. 206–216, doi:10.1109/36.739155.

Wilks, D. S. (2011), *Statistical methods in the atmospheric sciences*, Academic Press, Oxford; Waltham, MA.

Wilson, J. J. W., C. Anderson, M. A. Baker, H. Bonekamp, J. F. Saldaña, R. G. Dyer, J. A. Lerch, G. Kayal, R. V. Gelsthorpe, M. A. Brown, E. Schied, S. Schutz-Munz, F. Rostan, E. W. Pritchard, N. G. Wright, D. King, and U. Onel (2010), Radiometric calibration of the advanced wind scatterometer radar ASCAT carried onboard the METOP-A satellite, *IEEE Transactions on Geoscience and Remote Sensing*, **48**, p. 3236–3255, doi:10.1109/TGRS.2010.2045763.

Woodhouse, I. H. (2006), *Introduction to microwave remote sensing*, Taylor & Francis, Boca Raton.